FINITE ELEMENT ANALYSIS AND TESTS OF COMPOSITE BEAMS WITH FIBER BRAGG GRATING SENSORS UNDER TORSIONAL LOAD FOR STRUCTURAL HEALTH MONITORING APPLICATIONS

A THESIS SUBMITTED TO
THE GRADUATE SCHOOL OF NATURAL AND APPLIED SCIENCES
OF
MIDDLE EAST TECHNICAL UNIVERSITY

BY

CANSU KARATAŞ

IN PARTIAL FULFILLMENT OF THE REQUIREMENTS
FOR
THE DEGREE OF MASTER OF SCIENCE
IN
AEROSPACE ENGINEERING

SEPTEMBER 2017

Approval of the thesis:

FINITE ELEMENT ANALYSIS AND TESTS OF COMPOSITE BEAMS WITH FIBER BRAGG GRATING SENSORS UNDER TORSIONAL LOAD FOR STRUCTURAL HEALTH MONITORING APPLICATIONS

submitted by **CANSU KARATAŞ** in partial fulfillment of the requirements for the degree of **Master of Science in Aerospace Engineering Department, Middle East Technical University** by,

Prof. Dr. Gülbin Dural Ünver
Director, Graduate School of **Natural and Applied Sciences**

Prof. Dr. Ozan Tekinalp
Head of Department, **Aerospace Engineering**

Prof. Dr. Yavuz Yaman
Supervisor, **Aerospace Engineering Dept., METU**

Examining Committee Members

Prof. Dr. Serkan Özgen
Aerospace Engineering Dept., METU

Prof. Dr. Yavuz Yaman
Aerospace Engineering Dept., METU

Assoc. Prof. Dr. Melin Şahin
Aerospace Engineering Dept., METU

Assist. Prof. Dr. Gökhan Özgen
Mechanical Engineering Dept., METU

Assoc. Prof. Dr. Erdem Acar
Mechanical Engineering Dept., TOBB
University of Economics and Technology

Date: 07.09.2017

I hereby declare that all information in this document has been obtained and presented in accordance with academic rules and ethical conduct. I also declare that, as required by these rules and conduct, I have fully cited and referenced all material and results that are not original to this work.

Name, Last name: Cansu, Karataş

Signature:

ABSTRACT

FINITE ELEMENT ANALYSIS AND TESTS OF COMPOSITE BEAMS WITH FIBER BRAGG GRATING SENSORS UNDER TORSIONAL LOAD FOR STRUCTURAL HEALTH MONITORING APPLICATIONS

KARATAŞ, Cansu
M.Sc., Department of Aerospace Engineering
Supervisor: Prof. Dr. Yavuz Yaman

September 2017, 113 pages

In this thesis, feasibility of Fiber Bragg Grating sensors for Structural Health Monitoring applications of composite structures is studied. The method and essentials for the manufacturing process of composite beams with embedded Fiber Bragg Grating sensors are presented. Composite beams instrumented with surface bonded and embedded Fiber Bragg Grating sensors are tested under static torsional load. In addition, Finite Element Analyses of composite beams under torsional load is conducted using the commercial finite element code ABAQUS®. Subsequently, the results obtained from the tests and from the Finite Element Analyses are compared to observe the consistency between the torque and shear strain results. Furthermore, as a case study, static torsion test of a composite beam equipped with both a strain gage and a Fiber Bragg Grating sensor is performed for the purpose of identifying the agreement between the shear strain results.

Keywords: Fiber Bragg Grating Sensors, Structural Health Monitoring, Embedded Fiber Bragg Grating Sensors, Finite Element Analysis, Torsional Load, Static Torsion Test

ÖZ

YAPISAL SAĞLIK İZLEME UYGULAMALARI İÇİN FIBER BRAGG IZGARA ALGILAYICILAR İÇEREN KOMPOZİT KİRİŞLERİN BURULMA YÜKLERİ ALTINDAKİ SONLU ELEMANLAR ANALİZLERİ VE TESTLERİ

KARATAŞ, Cansu
Yüksek Lisans, Havacılık ve Uzay Mühendisliği Bölümü
Tez Yöneticisi: Prof. Dr. Yavuz Yaman

Eylül 2017, 113 sayfa

Bu tezde, kompozit yapıların Yapısal Sağlık İzleme uygulamaları için Fiber Bragg Izgara algılayıcıların uygulanabilirliği incelenmiştir. Gömülü Fiber Bragg Izgara algılayıcı içeren kompozit kirişlerin üretim süreci metodu ve gereklilikleri sunulmuştur. Yüzeye yapıştırılmış ve gömülü Fiber Bragg Izgara algılayıcılarla donatılmış kompozit kirişler statik burulma yükü altında test edilmiştir. Ek olarak, kompozit kirişlerin burulma yükleri altındaki Sonlu Elemanlar Analizleri, ticari sonlu elemanlar kodu ABAQUS® kullanılarak gerçekleştirilmiştir. Takiben, Sonlu Elemanlar Analizlerinden ve testlerden elde edilen burulma momenti ve kayma gerinimi sonuçları, aralarındaki tutarlılığı gözlemlemek amacıyla karşılaştırılmıştır. Ayrıca, bir örnek çalışma olarak, gerinim ölçer ve Fiber Bragg Izgara algılayıcılarla donatılmış bir kompozit kirişin statik burulma testi, gerinim sonuçları arasındaki uyumu belirlemek amacıyla gerçekleştirilmiştir.

Anahtar Kelimeler: Fiber Bragg Izgara Algılayıcılar, Yapısal Sağlık İzleme, Gömülü Fiber Bragg Izgara Algılayıcılar, Sonlu Elemanlar Analizi, Burulma Yükü, Statik Burulma Testi

Atam'a…

ACKNOWLEDGEMENTS

I would like to thank my supervisor Prof. Dr. Yavuz YAMAN for his guidance, valuable advice and support throughout the study.

I am deeply and sincerely grateful to Assoc. Prof. Dr. Melin Şahin for sharing his knowledge, patience, kindness and support.

I also would like to thank Hakan İşçi and Murat Ceyhan for supporting this thesis and giving me the chance to work for this intriguing research and development project as a part of the Rotary Wing Technology Center. This study is funded by Turkish Aerospace Industries as a part of the project DKTM/2014/04.

I am sincerely indebted to my smart and understanding colleague Boray Değerliyurt who takes part in the same project. I learned that the support of a colleague is very important for the success of the study.

I gained valuable technical experience while working for the Rotary Wing Technology Center. However, I also had the chance of making smart, lovely and precious friends. I am grateful to my dearest colleagues Ali Kıvanç Ersan, Ali Oğuz Yüksel, Gökçe Özgül, Mehmet Ali Yavuz, Ozan Alican, Senem Aktaş, and Sinem Uluocak for all the support, love and laughter.

I cannot express how grateful I am for having the love and support of my beloved parents who were always there for me when I needed. I am the luckiest daughter in the world.

Finally, I would like to express my gratitude towards my beloved fiancé Mustafa Demircan for his endless love, patience and support.

TABLE OF CONTENTS

CHAPTERS

APPENDICES

LIST OF TABLES

TABLES

LIST OF FIGURES

FIGURES

CHAPTER 1

INTRODUCTION

1.1 Motivation and Objective of the Thesis

Fiber reinforced polymer composite materials have been preferred for structural parts in aeronautical industry because of their exceptional properties such as ease to manufacture complex parts, high strength-to-weight ratio, corrosion resistance, and fatigue resistance properties. However, their complex failure modes and difficulty of maintenance have accelerated the research activities on advanced monitoring technologies.

Structural Health Monitoring (SHM) is an emerging technology to monitor the condition of the structure continuously, detect damages in advance and prevent failure before occurring. SHM technologies depend heavily on enhancements in sensing technology. Fiber Bragg Grating (FBG) strain sensors have become appealing for the SHM of composite structures because of their inherent properties including light weight, immunity to electromagnetic interference, capability of multiplexing, and most importantly, the ability to embedment into composites.

The objective of the thesis is to research and demonstrate the feasibility of FBG sensors for SHM of composite structures by performing static tests of composite beams instrumented with embedded and surface bonded FBG sensors and comparing the results of tests with Finite Element Analyses (FEA) to observe the agreement between them. Thesis study represents a part of a project supported by the Rotary Wing Technology Center, which is the research and development center in Turkish

Aerospace Industries, Inc. Considering the needs of the project, the beams are intended to be tested under torsional load since rotary wings such as helicopter blades are exposed continuously to torsional loads throughout their operation.

1.1 Assumptions and Limitations of the Thesis

The assumptions and limitations of the thesis are listed below.

- Only geometric nonlinearity is included in the FEA. Material nonlinearity could not be included due to the fact that material properties in plastic region are not available.
- According to literature, it is assumed that the sensors do not affect the mechanical properties of the host material. For that reason, FBG sensors are not modeled for Finite Element Model of the composite beams.
- All the tests are assumed to be performed under room temperature. In addition, variations of temperature during the tests are assumed to be small.
- The axial and transverse strains are assumed to be negligible with respect to the in-plane shear strain under torsional load.

1.2 Layout of the Thesis

In Chapter 2, literature review is conducted to generate background information about the SHM motivations and applications in civil, aerospace and mechanical engineering fields. In addition, working principles and advantages of using FBG sensors for SHM applications are explained.

In Chapter 3, Finite Element Model development and FEA results for composite beams under torsional load is presented.

Chapter 4 explains the tests of the composite beams under torsional load. Manufacturing composite beams with embedded FBG sensors and sensor system are also included.

In Chapter 5, torque and shear strain results obtained from the torsion tests using FBG sensors and the FEA are compared to observe the consistency of the results. In addition, a case study is conducted to observe the agreement between the results obtained from a strain gage and a FBG sensor.

Finally, conclusions reached from the thesis study and future work are pointed out in Chapter 6.

CHAPTER 2

LITERATURE REVIEW

2.1 Introduction

In this section, literature review study is performed to generate background information about Structural Health Monitoring (SHM) and Fiber Bragg Grating (FBG) sensors. In section 2.2, motivations behind the SHM studies and flowchart to conduct SHM are presented. Section 2.3 includes working principles of FBG and advantages obtained through use of FBG Sensors for SHM applications. In addition to these, the studies which include manufacturing of composite structures with embedded FBG sensors are also presented to guide throughout the manufacturing process. Finally, FBG sensor applications for SHM of composite structures are reviewed.

2.2 Structural Health Monitoring

Structural Health Monitoring is an emerging technology which involves continuously monitoring of the features which represent the state of the structure concerned. The aim of SHM is to improve safety, reliability and maintainability of civil, aerospace and mechanical engineering infrastructures by identifying the changes in features at the earliest stage.

Applications of SHM are widespread for infrastructures of civil, aeronautical and mechanical engineering.

Civil infrastructure are vast structures which are prone to corrosion, pressure and fatigue failure during the long-term use. The maintenance, inspection and rehabilitation of these structures require great effort due to the unsuitability to reach the structures. SHM offers a great convenience of intervening the system remotely by integrating a damage identification system into the structure during the construction. Bridges [1], [2], buildings [3], and tunnels [4], [5] are among the civil infrastructure on which SHM methods are applied.

Aerospace structures, civil and military aircrafts and helicopters, operate under harsh conditions. There are strict safety, reliability and maintainability regulations with the requirement of periodic maintenance schedules. However, maintenance operations demand great effort and cost. Also, each maintenance operation increases the downtime of the vehicles. SHM is convenient for monitoring the structures and performing maintenance only when needed. SHM has been practiced on rotor blades [6]–[9], wind turbine blades [10], [11] and wings of civil and military aircrafts [12]–[15].

Mechanical structures also operate under severe conditions, considering rotating machinery [16], bearings [17] and other connection parts [18]. SHM offers the advantage of the ability to prevent failure by detecting any deterioration in advance.

In general, developing a SHM system and integrating into the structures enhance safety and reliability of civil, aerospace and mechanical engineering structures considering the advancements below.

- Avoiding catastrophic failure by detecting damage in advance
- Monitoring the infrastructures while in use
- Shortening downtime by replacing schedule based maintenance with condition based maintenance

- Cutting down the life-cycle costs due to reduced number of maintenance cycles
- Reducing maintenance labor by only focusing on the damaged parts of the structures
- Eliminating the need of physical access to the inspection area
- Reducing the time for maintenance by inspecting multiple locations at the same time

Flowchart of a typical SHM procedure is presented in Figure 2.1 [19]. The steps will be explained by order in the following paragraphs.

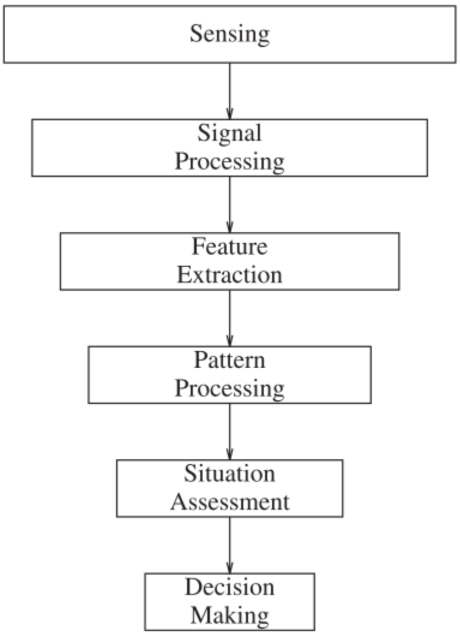

Figure 2.1: Structural Health Monitoring Flow Chart [19]

First of all, SHM requires a sensor system for monitoring the features sensitive to the damage, among which are natural frequency, strain, time data of acceleration, displacement mode shapes and strain mode shapes. Improvement of sensor technology in terms of size, weight, cost and efficiency allowed utilization of sensors as an integral part of the structures [20]. Use of different sensors such as accelerometers, conventional strain gages, piezoelectric sensors, and fiber optic sensors for SHM purposes is present in the literature.

Accelerometers are among the most used sensors for SHM applications because of their availability and cost. Accelerometers are generally used for Frequency Domain Methods [21], [22]. Drawback of the accelerometers is that accelerometers could change the mass of the structure if they are used in great numbers.

Conventional strain gages have been widely used for experimental studies since they are low-cost, small, and lightweight products of a mature technology. Strain gages are suitable for Strain Based Damage Identification Methods [9], [23] and Frequency Domain Methods [9], [22]. A disadvantage of strain gage use for SHM is that a lot of sensor is needed to cover a large area. The wires needed for the strain gages are another challenge for SHM.

The ability to use piezoelectric materials as both a sensor and an actuator makes them exceptional in the field. In addition, piezoelectric sensors are light, highly sensitive to strain and need little power [24]. They have been utilized for different damage detection methods such as Lamb Wave Methods [24], [25], Acoustic Emission Methods [26] and Electro-Mechanical Impedance Methods [27]. However, ambient vibration and temperature have negative effects on piezoelectric sensors.

Fiber optic sensors are being utilized more and more for SHM purposes because of their lightweight, electromagnetic interference immunity and large area coverage thanks to their multiplexing capability. However, the ability to be embedded into the composite structures is the most important property of fiber optic sensors. The damage detection studies with Strain Based Methods [10], [28]–[31] using fiber optic sensors are present in the literature. Types of fiber optic sensors are interferometric sensors, distributed sensors and Grating-based sensors [28]. In this study, one type of the fiber optic sensors is interested, which is Fiber Bragg Grating sensors. A detailed review on FBG sensors is presented in section 2.3.

Second step of SHM includes signal processing and feature extraction. Basically, the signal obtained from the sensor system is examined, filtered and treated by algorithms to obtain useful data. Then, features indicating damages are extracted from the useful data.

Later, damage identification methods are needed to interpret changes in the features. Damage is defined as a permanent change in the mechanical state of a structural material or a component which might alter the performance of the structure [32]. Damage identification is a process of diagnosing the health of the structure by analyzing the changes in the features that indicate the condition of the structure. Pattern processing and situation assessment are included in damage identification practice. According to Rytter [33], damage identification process has five levels as shown below.

1. Recognizing the existence of damage
2. Locating the damage
3. Distinguishing the type of the damage
4. Observing extent of the damage
5. Prognosis of the remaining life

There are different damage identification methods applied on composite structures such as Frequency Domain Methods [24], [34], Wave Propagation Methods [24], [35], Eddy Current Methods [36], and Strain Based Methods [10], [12], [15], [37], [38].

Finally, decision making process is performed to determine whether the structure could continue its function or it needs maintenance. Statistical methods are utilized during the decision making process.

2.3 Fiber Bragg Grating Sensors

Fiber optic sensors have found applications in monitoring the manufacturing process by measuring the strain and temperature, checking the conditions during the assembly process by contributing to nondestructive evaluation, structural health monitoring by helping the establishment of sensor network, and complementing performance monitoring systems [39].

FBG sensors are one type of fiber optic sensors based on the reflection of light with a particular wavelength called Bragg wavelength.

Working principles and inherent properties of FBG sensors that make them one of the ideal sensors for SHM will be discussed in detail throughout this section. In addition, the solutions for the problems encountered during the manufacturing of composite structures with embedded sensors will be explained. Finally, some of the SHM applications for composite structures in the literature will be presented.

2.3.1 Working Principles of Fiber Bragg Grating Sensors

Fiber optic cables are composed of three layers which are core, cladding and coating as seen in Figure 2.2 [40]. Light emitted from a light source is transmitted through the core which is generally made of glass. Outside the core, cladding ensures the quality of the transmission by reflecting the stray light back to the core. Core and cladding are surrounded by the coating layer which provides protection from the external conditions and physical damage [40]. Most importantly, stress and strain is transmitted from the structural element to the fiber through the coating. The coating thickness, chemical compatibility with the host material, rigidity and tolerance to the curing process might affect the response when FBG sensors are embedded into the composites [41].

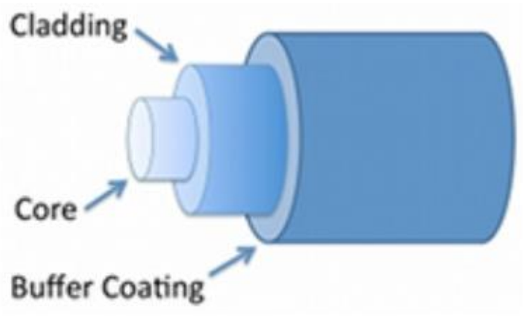

Figure 2.2: Layers of Fiber Optic Cables [40]

FBGs are produced by exposing a short length of fiber (1 mm to 10 mm) within the core to a periodic distribution of light intensity. Since fibers are photosensitive, i.e., sensitive to UV radiation, the refractive index of the related section is altered permanently [40]. When a broadband light beam is transmitted through the optical fiber, it reflects from the FBGs as a narrowband light beam called Bragg wavelength, as described in Figure 2.3 [42]. Thus, FBG is basically a filter which allows reflection of only a specific frequency of light.

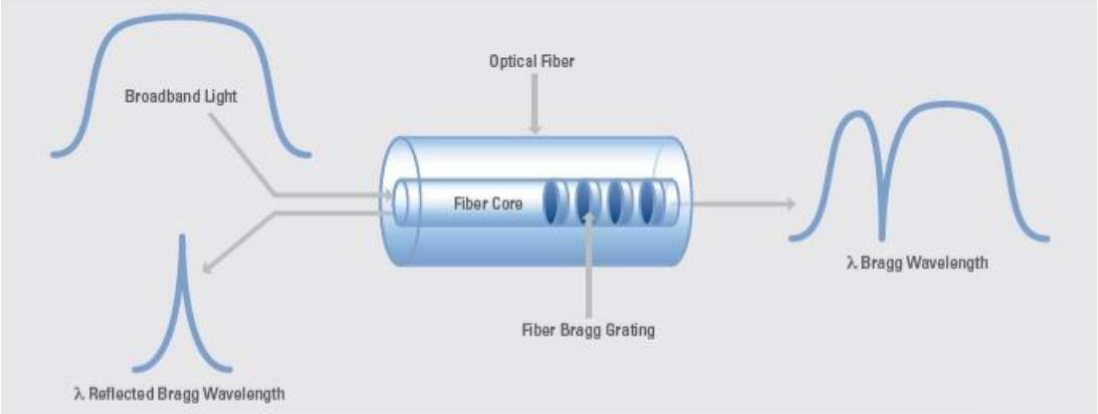

Figure 2.3: Bragg Wavelength Reflected from the Grating [42]

Equation 2.1 describes the dependence of Bragg wavelength on the refractive index of the core and the spacing between gratings as shown in Figure 2.4 [40].

$$\lambda_b = 2n\Lambda \tag{2.1}$$

where

λ_b: Bragg Wavelength

n: The refractive index of the core

Λ: Spacing between the gratings

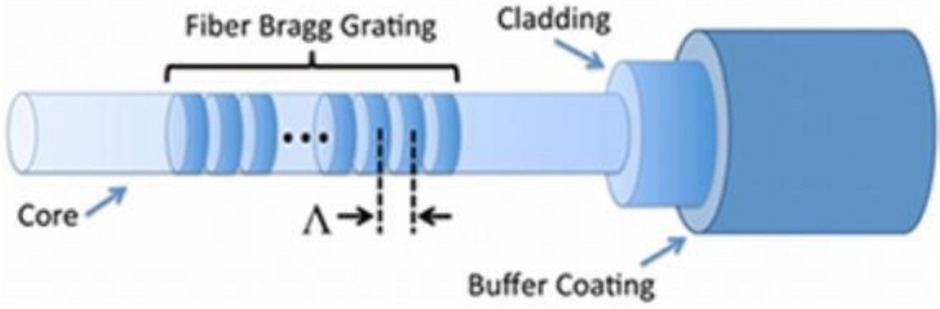

Figure 2.4: Fiber Bragg Grating in the Core of the Fiber Optic Cable [40]

The FBG with a specific Bragg Wavelength desired could be produced by adjusting the spacing between the gratings. One could record multiple FBG sensors with unique wavelengths on a single fiber, which is called multiplexing, and interrogate them at the same time.

Elongation or retraction of the FBG sensor in response to temperature and strain leads to the shift of the Bragg wavelength since the spacing between the gratings and refractive index of the core changes. The temperature and strain lead to a shift in Bragg wavelength in a linear manner as described in Equation 2.2 [40] .

$$\frac{\Delta\lambda}{\lambda_0} = (1 - p_e) * \varepsilon + (\alpha_\Lambda + \alpha_n) * \Delta T \qquad \boxed{2.2}$$

where

$\Delta\lambda$: Wavelength shift

λ_0: Initial wavelength

ρ_e: Strain-optic coefficient

ε: Strain

α_{Λ}: Thermal expansion coefficient

α_n: Thermo-optic coefficient

ΔT: Change in temperature

The parameters strain-optic coefficient (ρ_e) and thermal expansion coefficient (α_{Λ}) are material properties, whereas thermo-optic coefficient (α_n) is sensitive to the variations in the refractive index.

Finally, algorithms perform the transformation of the change in wavelength to strain measurements.

2.3.2 Advantages and Disadvantages of Using Fiber Bragg Grating Sensors for Structural Health Monitoring

FBG sensors have many inherent properties which makes them one of the ideal sensors for SHM applications.

First of all, they are small (generally with a diameter of 125 µm - 250 µm) and lightweight which generates the ability to be embedded in the composite structures. The mechanical properties of the structure do not get affected severely when fiber optic cables are placed between the layers of fiber reinforced plastic materials [43]. The embedment of the FBG sensors also provides a protection from the environmental conditions such as humidity and temperature.

Another property of optical fibers is again advantageous for embedment of them into the composite structures which is the ability to withstand high temperatures and pressures, two main parameters for the curing of the composite materials. The coating is generally made of polymers such as Acrylate or Polyimide. Acrylate coating allows a temperature range of -270°C and 85°C, whereas Polyimide coating allows the FBGs to work between a temperature range between -270°C and 300°C [44]. Polyimide coatings are preferred for embedment to the composite structures since cure temperature of composites is around 180°C. Also, rigidity and strength of the Polyimide are greater than those of the Acrylate [41].

In addition, fiber optic cables are produced from different classes of glass, which is known to be a dielectric material. This characteristic makes them immune to electromagnetic interference (EMI) which is a serious problem especially for aeronautical structures [43].

Also, on a single fiber more than one FBG sensors could be produced which is called multiplexing. Multiplexing is achieved by assigning each FBG sensors a unique wavelength on the available spectrum of the light source. Multiplexing capacity depends on the number of channels on the interrogator device for parallel multiplexing and the total wavelength range of the interrogator (in general, 40 – 80 nm) for in-line multiplexing, as shown in Figure 2.5 [29] .

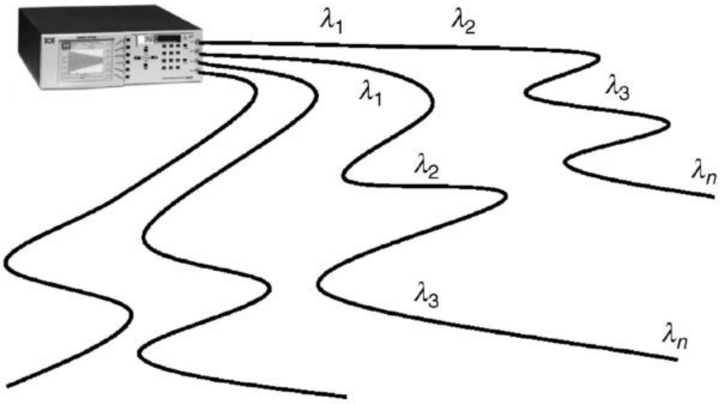

Figure 2.5: Multiplexing Capacity of FBG Sensors [29]

FBG sensors could be issued as reliable, safe and performance enhancing sensors for Structural Health Monitoring applications considering the advantages explained above. In addition, it is demonstrated that FBG sensors offer reproducible and reliable strain measurements [45]. In addition, FBG sensors do not need calibration through their life since they have a digitally encoded identity which does not change. Initially nulling the system, i.e. resetting the measurement, is sufficient for accurate measurements [46], [47]. However, the most important contribution of the FBG sensors to the SHM applications is that they are suitable for being embedded into the composite materials for monitoring the state and distribution of strains in the structures.

Disadvantages of FBG sensors could be the fragility and unpracticality to handle. FBG sensors require great care during manufacturing processes.

2.3.3 Manufacturing of Composite Structures with Embedded FBG Sensors

The ability to be embedded between the layers of the composite beams makes the FBG sensors one of the most suitable sensors for the SHM. However, care should be taken during the manufacturing of the composites with embedded FBG sensors. Stress concentrations are expected at the ingress/egress points, which might lead to the breakage of the fragile fiber optic cables during curing and handling [48].

Ramly et al. explained the process of manufacturing sandwich panels, which are a part of the vertical stabilizer, with embedded FBG sensors as seen in Figure 2.6. Note that they measured the signals of the FBG sensors before and after the embedding process to observe their functionality for further experiments [49].

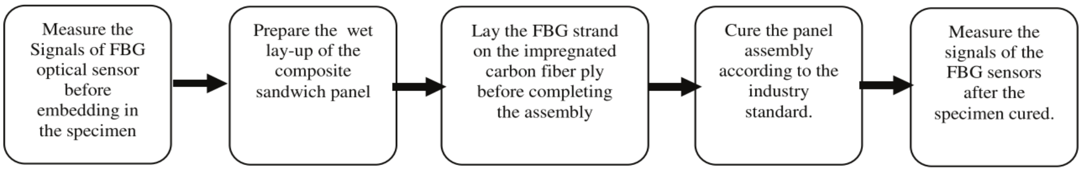

Figure 2.6: A Typical Process of Manufacturing Sandwich Panels with Embedded FBG Sensors [49]

One of the main problems encountered during the manufacturing of the composite structures with embedded FBG sensors was the stress concentration at the ingress/egress regions where the fiber optic cables are evacuated from the beam. Teflon and plastic tubes are placed around the fiber optic cables as precautions in the literature to solve that problem. Pedrazzani et al. used Teflon tubes at the ingress and egress points to ensure the safety of the fiber optic cables embedded into a large scale wind turbine blade as presented in Figure 2.7 [10].

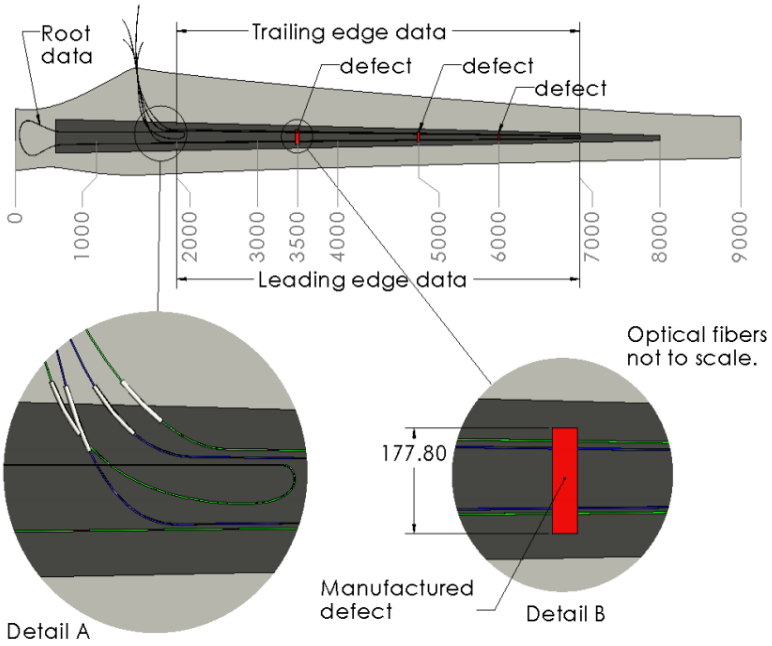

Figure 2.7: Teflon Tubes at the Ingress and Egress Points [10]

Kahandawa et al. also used Teflon tubes for the protection of the fiber optic cables at the egress region where stress concentration is expected based on the Finite Element Analysis. Figure 2.8 presents the egress region after the cure of the beam [50].

Figure 2.8: Teflon Tubes at the Egress Region [50]

Dawood et al. preferred use of plastic tubes at the egress points while producing a sandwich panel with resin infusion method. Also, they isolated the fiber optic cables from the resin by placing them in non-sticking film bag at the evacuation regions as shown in Figure 2.9 [51].

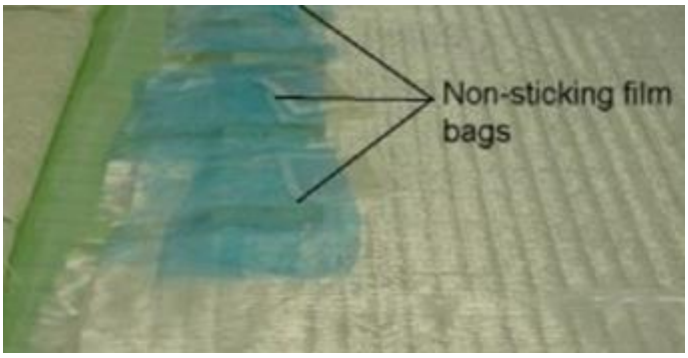

Figure 2.9: Isolated Fiber Optic Cables using Non-sticking Film Bag [51]

Optical loss due to the curvature of the fiber optic cable is another problem encountered during embedment of the fiber optical sensor [51]. Hayama et al. inspected the effect of curvature with a conclusion that the power loss becomes negligible after a 30 mm of radius curvature [52].

2.3.4 Embedded FBG Sensor Applications for Structural Health Monitoring of Composite Structures

SHM of composite structures is the main interest of this thesis, therefore the studies related to them will be reviewed in this subsection.

Composite helicopter blades, wind turbine blades and aircraft wings are vulnerable to the damages due to aerodynamics loads, cyclic loads, foreign objects and engine vibration. Also note that, complex geometry of wing and blades make them prone to the edge delamination, matrix cracking and fiber breaking.

Kahandawa et al. installed a FBG sensor between the layers of a helicopter blade base to observe the FBG spectra at the stress concentration regions for SHM applications [48]. One of the important studies is the study where Bullock et al. were able to embed FBG sensors through the thickness of a composite flexbeam representative specimen to monitor the ply delamination at the edges, the principal failure mode of beams [53]. Crack propagation was able to be detected under tension loading.

Kim et al. measured deflection of a composite wind turbine blade under static loading with embedded FBG sensors on the bonding line with shear web and spar cab as shown in Figure 2.12 [11].

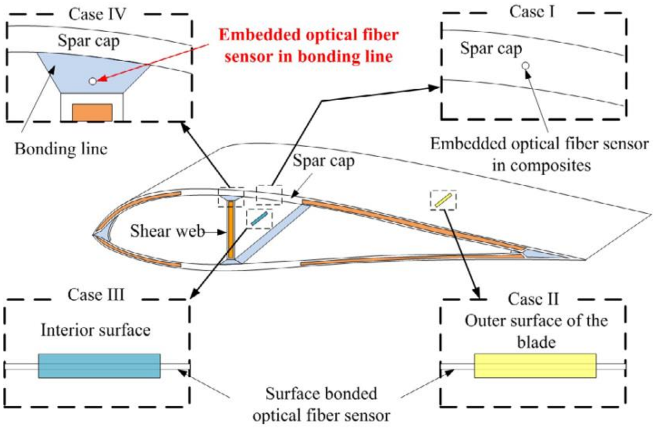

Figure 2.10: FBG Sensors Embedded in a Composite Wind Turbine Blade [11]

Costa et al. instrumented a scaled model of a T38 airplane wing shown in Figure 2.13 with FBG sensors for SHM and NDE applications [13].

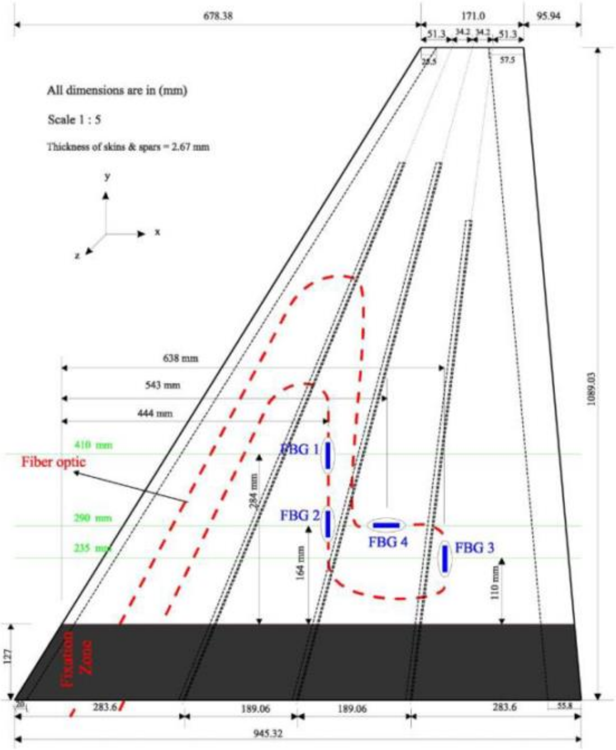

Figure 2.11: Embedded FBG Sensors in the Wings of a Scaled Model of T38 Airplane [13]

Skin and spars in aircraft wings are also suitable to be monitored with FBG sensors. Lee et al. conducted in-flight health monitoring of a subscale wing instrumented with two FBG sensors in the wing skin as shown in Figure 2.14 [15].

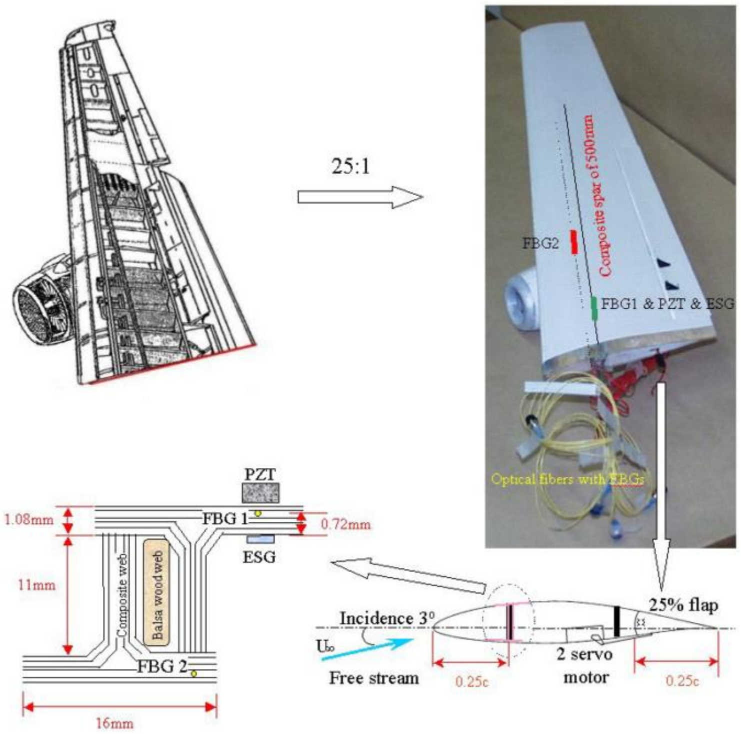

Figure 2.12: Subscale Wing Instrumented with FBG Sensors in the Wing Skin [15]

Composite beams are mostly preferred for developing and practicing new SHM and damage detection methods using FBG sensors. Response of the beams are observed under static and fatigue loadings to detect delamination, transverse crack and impact damage.

Takeda et al. placed FBG sensors within a CFRP beam to quantitatively observe the delamination length by relating the delamination length with the change in the spectrum [54]. Shin and Chiang conducted fatigue damage monitoring of a polymeric composite with a circular hole at the center using multiple FBG sensors [55]. Yashiro et al. even predicted multiple damage states (splits, transverse cracks and delamination) in composite beams utilizing embedded FBG sensors [56].

There are considerations about using embedded fiber optical sensors in composite structures, which are degradation of host material properties and increasing possibility of failure [57]. Diameter range of the fiber optic cables is 125 – 250 µm, which is larger compared to the diameter range of the S-glass reinforcement fibers (5 – 24 µm) [58]. However, it has shown that mechanical properties of the host structure do not get affected much if the fiber optic cable is placed parallel to the fibers of the composite layer. If fiber optic cable is placed in angular position compared to the fibers of the layer, resin pockets may form, which might lead to delamination. However, if fiber optic cable is needed to be used in an angular position, low fiber optic density is suggested such that the effect of fiber optic cable as a defect center is insignificant [57].

2.4 Conclusion

In this chapter, literature review study to generate background information on SHM and FBG sensors is conducted. SHM is an emerging and flourishing technology which improves safety, reliability and maintainability of civil, aerospace and mechanical engineering structures by continuously monitoring the damage sensitive features. SHM requires a sensor system to monitor the changes in the features. FBG sensors are being increasingly used for SHM of composite structures because of their superior characteristics such as light weight, electromagnetic immunity, multiplexing capacity and ability to be embedded between the composite layers. However, research and development activities are in progress for obtaining a mature SHM technology using FBG sensors such that it could be efficiently and practically applied on an operating structural part.

CHAPTER 3

FINITE ELEMENT ANALYSIS OF COMPOSITE BEAMS UNDER TORSIONAL LOAD

3.1 Introduction

In this chapter, development of Finite Element Model (FEM) for the analysis of composite beams under torsional load will be explained and results of Finite Element Analysis (FEA) will be demonstrated. FEM development part consists of description of the geometry, materials, boundary conditions, finite element properties and mesh convergence analysis. FEA part includes FEA results along with important points that are taken into account during the analysis.

3.2 Development of Finite Element Model

FEM of the composite beams are developed using the commercial FEA code ABAQUS®. ABAQUS® is comprised of different modules for the modeling and analysis [59]. ABAQUS® is one of the most user-friendly FEA software to develop a FEM considering the efficiency of the module system. In addition, the ability of ABAQUS® to easily adapt the whole model in accordance with the changes made after the first draft, however complex the model is, makes it a practical and convenient FEM development and FEA software.

Following subsections include demonstration of the geometry of the beams, materials assigned to the beam, boundary conditions applied, finite element properties and mesh convergence analysis.

3.2.1 Geometry of Composite Beams

The composite beams were obtained by scaling a part of a structural component which was expected to work under tension and torsion loads. The scaling was conducted in accordance with the related ASTM standards. Standards also recommend that tabs are bonded at the ends of the beams to protect the beams from the stress concentrations at the gripping region. Scaling and tab design studies were demonstrated in a study published by author [60] .

ABAQUS® is used to model two types of beams, which are the beams without tabs and the beams with tabs. The beams are modeled as 3-D, solid and deformable parts. In general, composites are suggested to be modeled as shells, however when normal stresses or interlaminate stresses near load application regions are important and their accuracy is desired, composites may be modeled as solids [61].

Figure 3.1 and Figure 3.2 show the 3-D geometry of the beams with the specified length, width and thickness measures. The beams with tabs have simple tabs bonded at the end of the beams with a thickness of 1.3 mm. Adhesive layer between the beam and the tabs has a thickness of 0.22 mm.

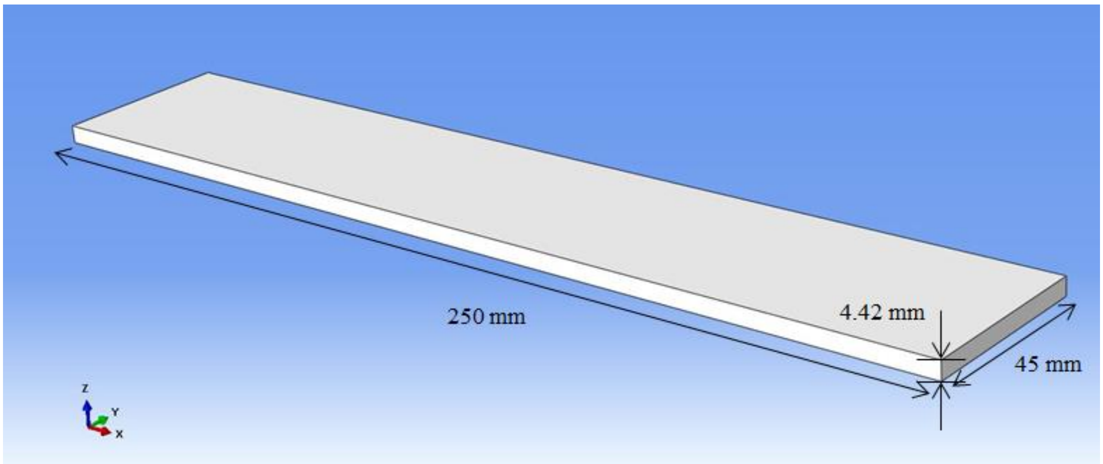

Figure 3.1: Geometry of the Beams without Tabs

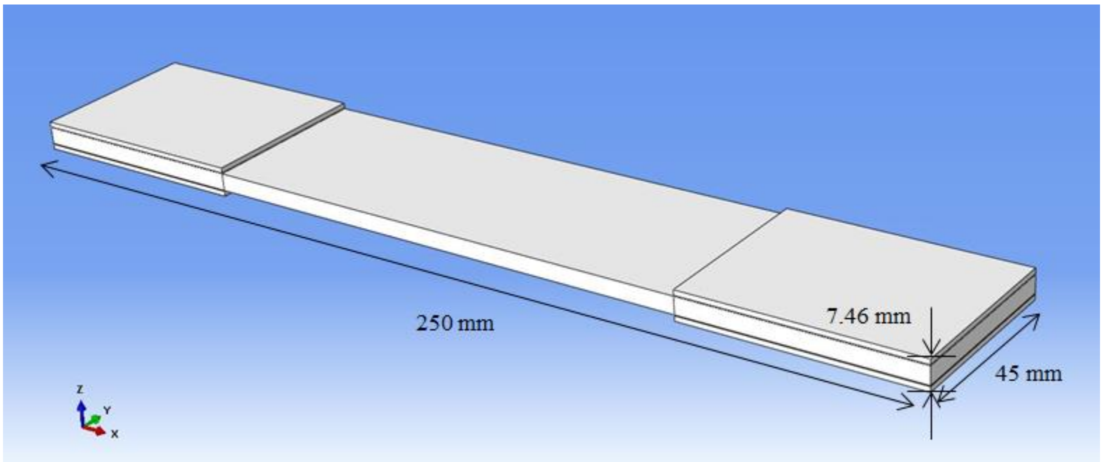

Figure 3.2: Geometry of the Beams with Tabs

3.2.2 Materials Specified to the Layers of Composite Beams

The beams are composite laminates which consist of glass/epoxy unidirectional composite layers, glass/epoxy woven composite layers and thermosetting epoxy adhesive strips with a stacking sequence of

$$[0_8/Film/(\mp 45)_{Woven}/(\mp 45)_{Woven}/Film/0_8].$$

Material of the tabs are the same as the glass/epoxy woven composite layers used in the beams. Also, thermosetting epoxy adhesive strips are used to bond the tabs to the beams.

The layers with the same material properties are modelled as one whole layer. Figure 3.3 and Figure 3.4 demonstrates the beams partitioned to apply different material properties to the divisions of the beams. Solid, homogeneous sections are created to assign the material properties to the divisions. Unidirectional composite layers, woven composite layers and adhesive strips are depicted as colors blue, green and magenta, respectively.

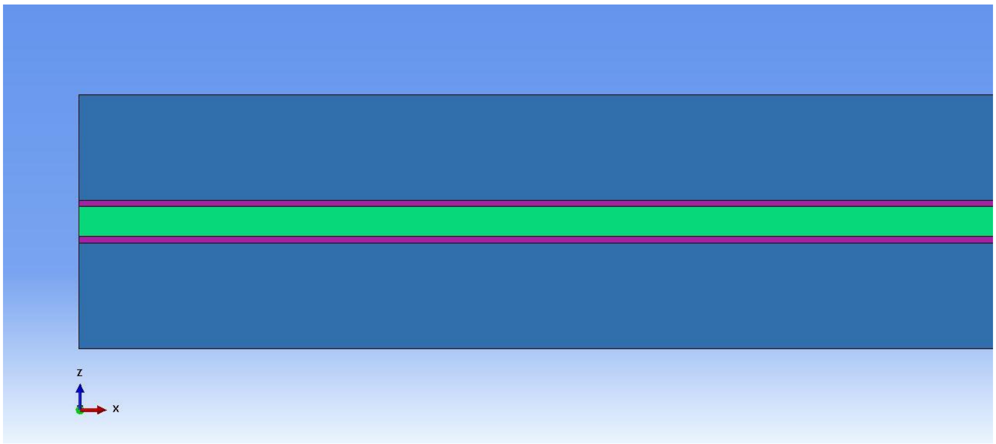

Figure 3.3: Material Assignment of the Beams without Tabs

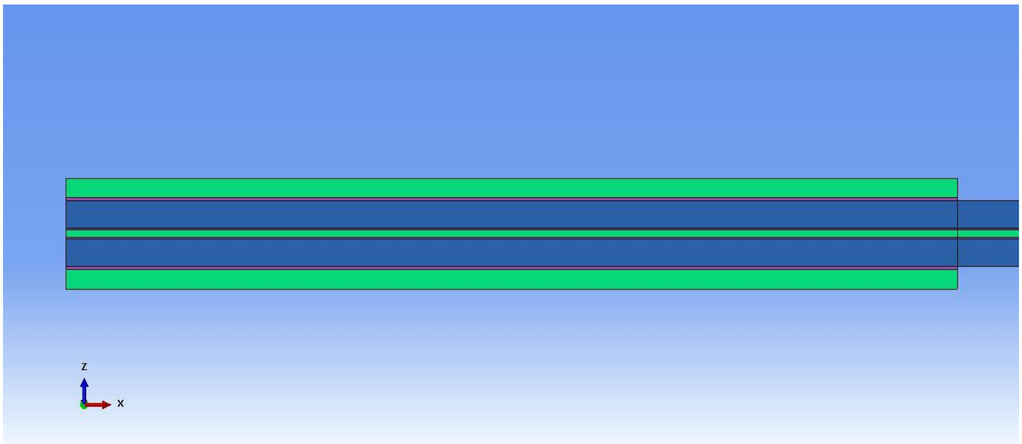

Figure 3.4: Material Assignment of the Beams with Tabs

Unidirectional and woven composite layers are modelled as orthotropic materials using *Engineering Constants* option which consists of Young's Moduli E_1, E_2, E_3; Poisson's Ratios $\vartheta_{12}, \vartheta_{13}, \vartheta_{23}$ and Shear Moduli $G_{12}, G_{13,} G_{23}$. Thermosetting epoxy adhesive strips are modelled as isotropic material using *Isotropic* option which only consists of Young's Modulus E and Poisson's Ratio ϑ. Linear elastic material properties of the materials were available and they were used as input for the FEM.

3.2.3 Boundary Conditions

The beams will be deformed under torsional load until a 20° of angle of twist is obtained. One end of the beams is given a fixed boundary condition and the other end of the beams is applied a torque, as seen in Figure 3.5.

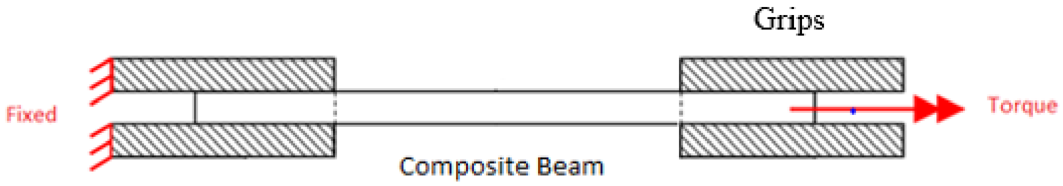

Figure 3.5: The Beams under Torsional Load

During the test, the grips of the machine will be in direct contact with the surfaces at the end of the beams. It is convenient to assume that the ends of the beams will move in accordance with the grips due to friction. FEM is desired to simulate the test conditions as close as possible. For that reason, surface nodes at the end of the beams which are in contact with the grips are tied to a reference node with rigid body constraint, which can be seen in Figure 3.6 and Figure 3.7. Rigid body constraint ensures that the motion of the surfaces in contact with the grips are governed by the motion of the reference nodes [61]. Then, boundary conditions are applied to the reference nodes (points) created. Although tabs are designed for a 60 mm length, only 50 mm of them will be in contact with the grips of the test machine.

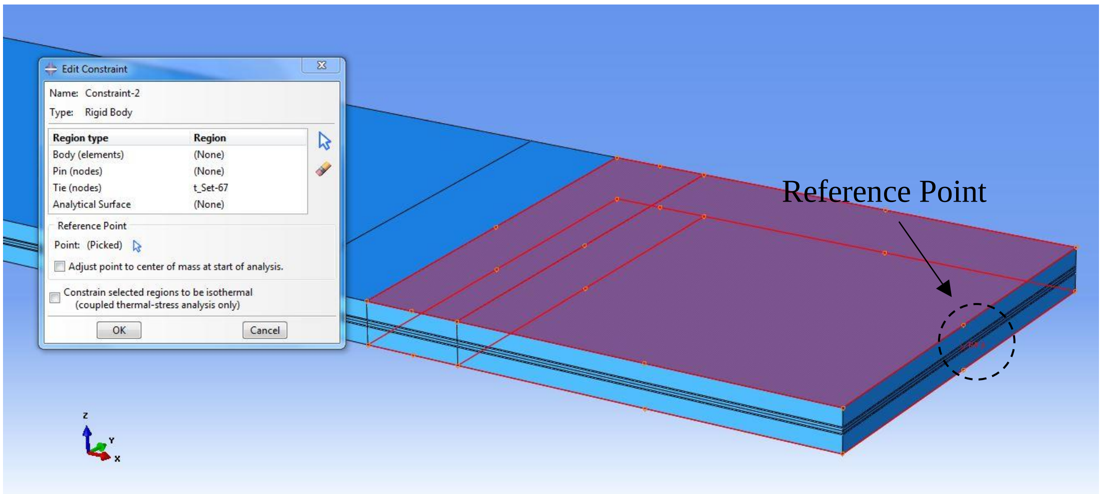

Edit Constraint

Name: Constraint-2

Type: Rigid Body

Region type	Region
Body (elements)	(None)
Pin (nodes)	(None)
Tie (nodes)	t_Set-67
Analytical Surface	(None)

Reference Point

Point: (Picked)

☐ Adjust point to center of mass at start of analysis.

☐ Constrain selected regions to be isothermal (coupled thermal-stress analysis only)

Figure 3.6: Rigid Body Constraint of the Surface Nodes to a Reference Node for the Beams without Tabs

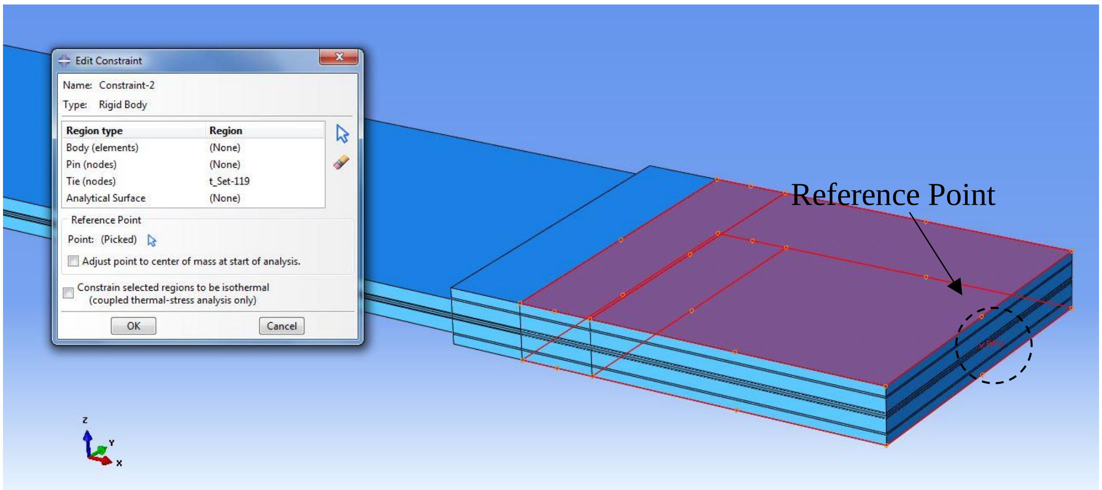

Edit Constraint

Name: Constraint-2

Type: Rigid Body

Region type	Region
Body (elements)	(None)
Pin (nodes)	(None)
Tie (nodes)	t_Set-119
Analytical Surface	(None)

Reference Point

Point: (Picked)

☐ Adjust point to center of mass at start of analysis.

☐ Constrain selected regions to be isothermal (coupled thermal-stress analysis only)

Figure 3.7: Rigid Body Constraint of the Surface Nodes to a Reference Node for the Beams with Tabs

The reference point at one end of the beams are constrained in all translational and rotational degrees of freedom to simulate the fixed boundary condition.

The reference point at the other end of the beams are constrained in all translational and rotational degrees of freedom around the axes, except the longitudinal axis (x axis). Translational degree of freedom is not constrained around the longitudinal axis, as in the test. Angle of twist is given around the longitudinal axis to simulate the torsional load applied to the beams.

3.2.4 Properties of Finite Elements and Mesh Convergence Analysis

Finite elements employed for the analysis are linear, hexahedral elements of type C3D8R and quadratic, hexahedral elements of type C3D20R. Nodes of both elements have three degrees of freedom. A typical coding of the finite elements in ABAQUS is explained in Figure 3.8, which helps to understand properties of the finite elements [61].

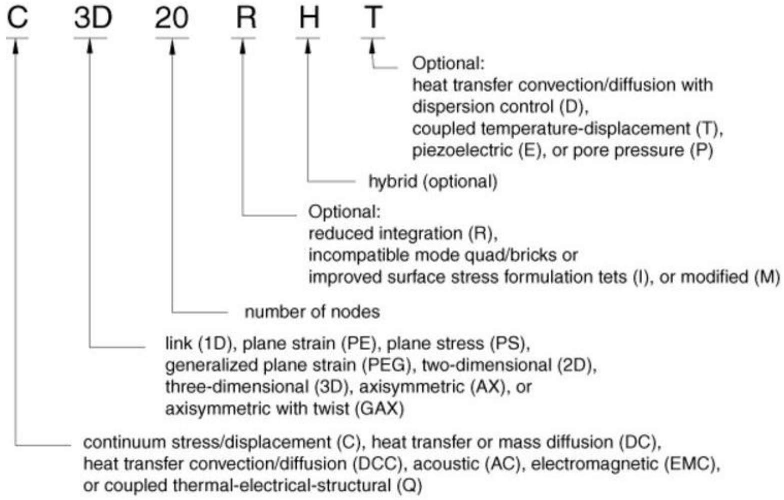

Figure 3.8: Coding Rules for the Finite Elements in ABAQUS [61]

C3D8R elements are 8-node, linear (first order), brick elements which uses reduced integration (1 integration point) with hourglass control [61]. The most accurate stress and strain values of C3D8R are obtained at integration points. For that reason, use of small elements is suggested to capture the stress concentrations at the boundaries [62].

C3D20R elements are 20-node, quadratic (second order), brick elements which uses reduced integration (8 integration points) with hourglass control [61].

Mesh convergence analysis should be conducted to ensure that the results of the analysis are not significantly affected from the mesh density. However, computational time should also be taken into account to avoid using impractical mesh structures. C3D8R elements are employed during mesh convergence analysis. Procedure follows as first applying a mesh size (seed) to whole model, then increasing the element number in thickness direction. The configurations for different meshes are presented in Table 3.1.

Table 3.1: Mesh Properties for Convergence Study

Beams without Tabs	**Configuration No.**	**Global Finite Element Size [mm]**	**Finite Element Number in Thickness Direction**	**Total Number of Elements**
	1	2.5	6	10800
	2	1	8	90000
	3	1	10	112500
	4	1	12	135000
	5	0.5	12	540000
Beams with Tabs	**Configuration No.**	**Global Finite Element Size**	**Finite Element Number in Thickness Direction**	**Total Number of Elements**
	1	2.5	6	14256
	2	1	8	111600
	3	1	10	144900
	4	1	12	178200
	5	0.5	12	712800

Reaction moments around longitudinal axis (torque) are obtained from the analysis results for the mesh properties given above, results of which are presented in Figure 3.9 and Figure 3.10. For both type of the beams, it is observed that torque results do not change much from mesh configuration 4 to mesh configuration 5. However, computational time increases vastly. Considering both the accuracy and computational time, the mesh configuration 4 (constructed from 135000 finite elements for the beams without tabs and 178000 finite elements for the beams with tabs) is chosen for both type of the beams.

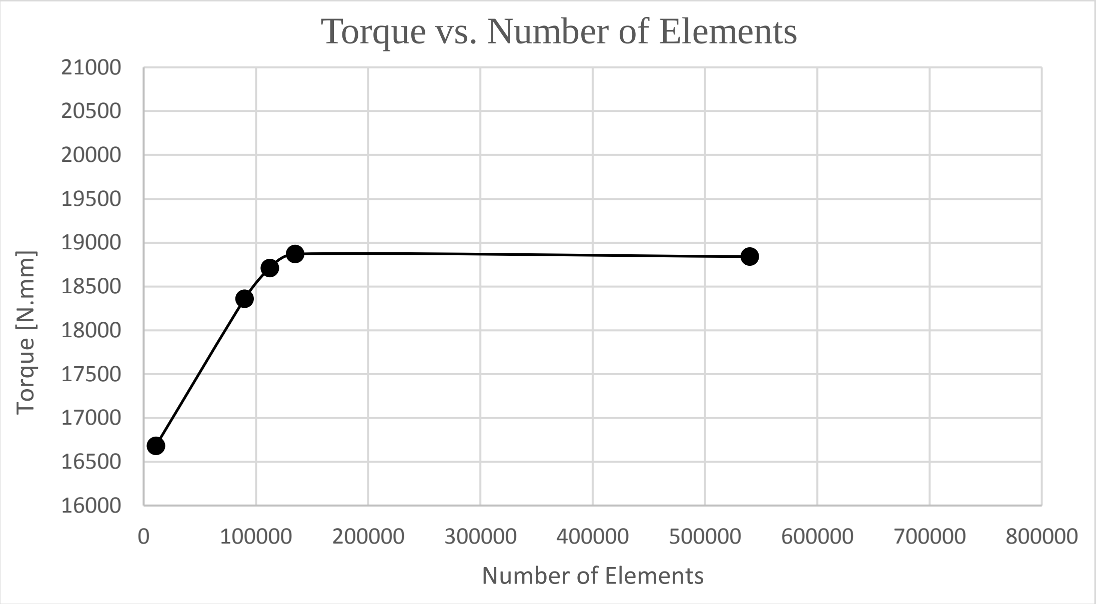

Figure 3.9: Mesh Convergence Results for the Beams without Tabs

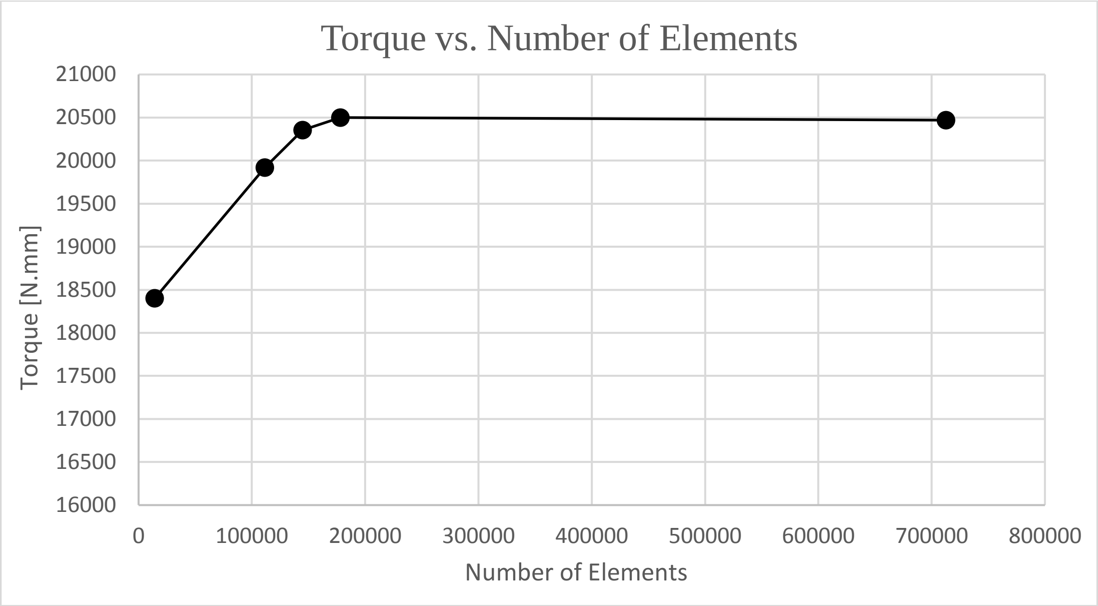

Figure 3.10: Mesh Convergence Results for the Beams with Tabs

Mesh structures that will be utilized for all the analysis is given in Figure 3.11 for the beams without tabs and in Figure 3.12 for the beams with tabs. Cross section views of the mesh structures are presented in Figure 3.13 and Figure 3.14. Unidirectional layers are modeled with eight elements, woven layers are modeled with two elements, adhesive film strips are modeled with two elements and woven layers in the tabs are modeled with three elements in thickness direction. Smallest finite element has dimensions of 1 mm x 1 mm x 0.11 mm, which models the adhesive film strips.

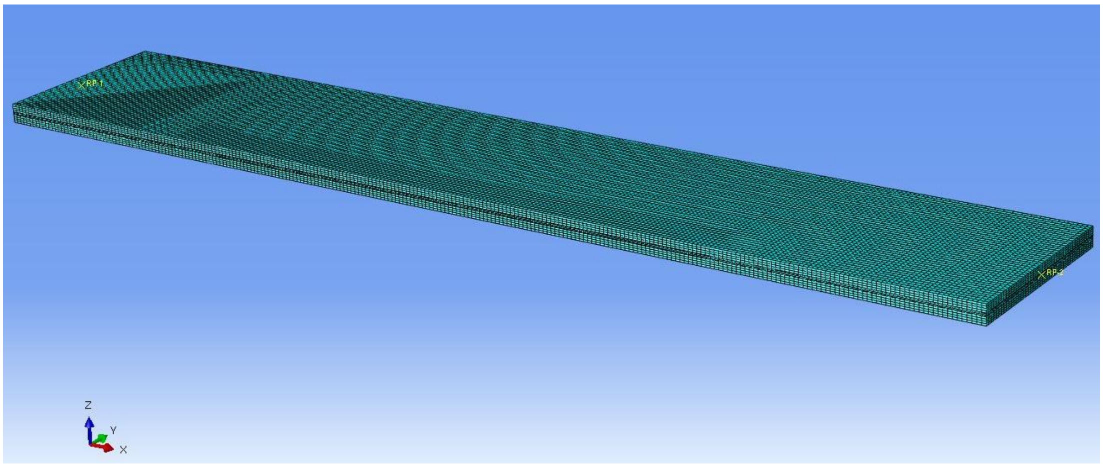

Figure 3.11: Mesh Structure for the Beams without Tabs

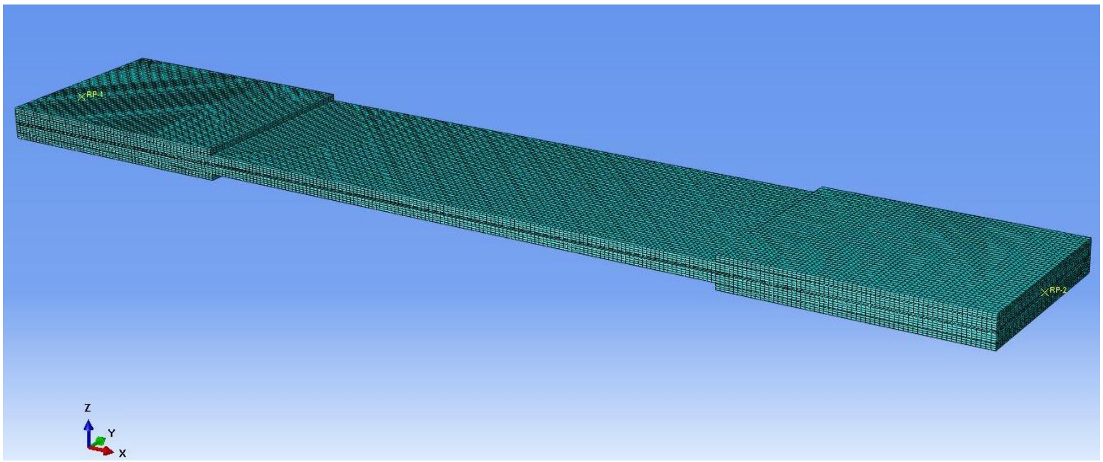

Figure 3.12: Mesh Structure for the Beams with Tabs

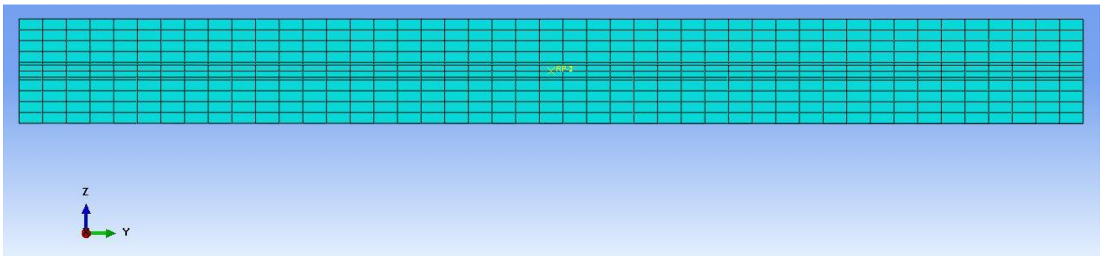

Figure 3.13: Cross Section View of the Mesh Structure for the Beams without Tabs

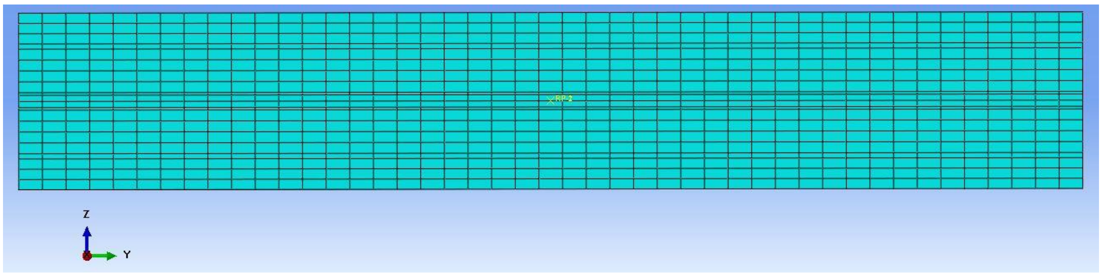

Figure 3.14: Cross Section View of the Mesh Structure for the Beams with Tabs

3.3 Description and Results of Finite Element Analysis

Following sections include finite element analysis description where the finite element analysis parameters are explained and finite element analysis results where results of analyses with different finite elements and analysis parameters are demonstrated.

3.3.1 Description of Finite Element Analysis

Static stress analysis was performed to simulate the torsion test of composite beams. Solution technique employed was full Newton and angle of twist was applied with 5° of increment.

Both material nonlinearity and geometrical nonlinearity should be included for the angle of twist desired for the tests (20°) since plasticity and large torsional rotations are expected to occur. In case of large displacements and rotations, finite elements distort from their original shapes and their nodal positions change as deformation increases. Nlgeom option allows to choose whether to formulate the elements using current nodal positions or original positions [61]. Geometrical nonlinearity could be included using *Nlgeom On* option. FEA are performed for both on and off options. The results for different configurations will be presented in following subsection 3.3.2.

Material nonlinearity; however, could not be modeled due to the fact that plastic region properties were not known.

3.3.2 Results of Finite Element Analysis

Finite Element Analysis results for the cases below will be presented in this section.

- FEA with linear geometry and C3D8R finite elements
- FEA with nonlinear geometry and C3D8R finite elements
- FEA with linear geometry and C3D20R finite elements
- FEA with nonlinear geometry and C3D20R finite elements

Reaction moments around longitudinal axis (torque) - angle of twist curves are given below in Figure 3.15 and Figure 3.16 for the beams. FEA results for C3D8R and C3D20R elements are nearly the same. However, there is an increasing difference between the results of FEA with linear and nonlinear geometry with increasing angle of twist.

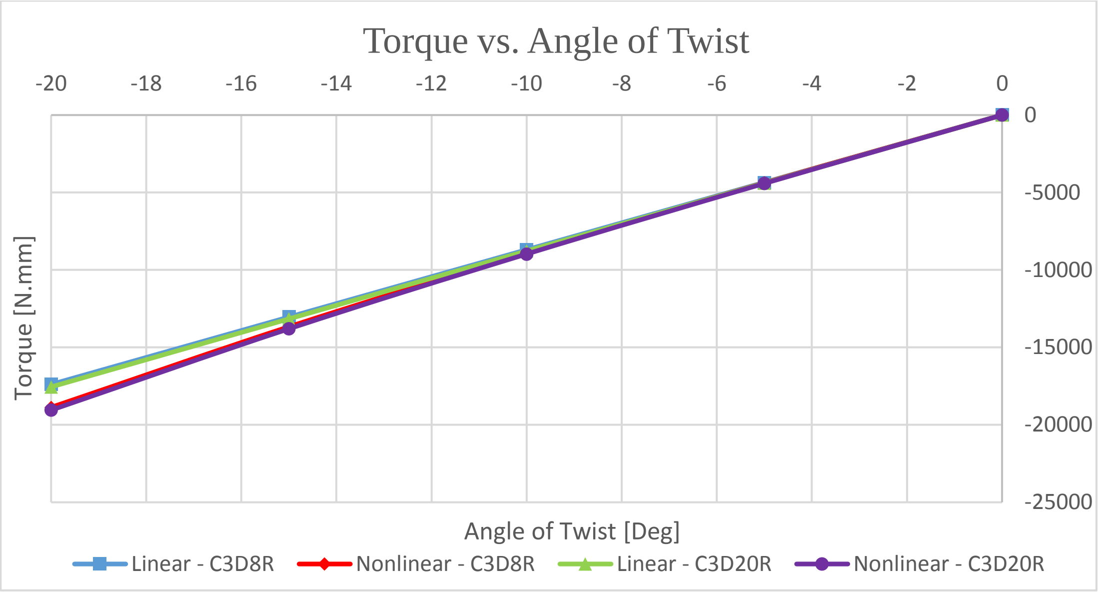

Figure 3.15: Torque - Angle of Twist Curves for the Beams without Tabs

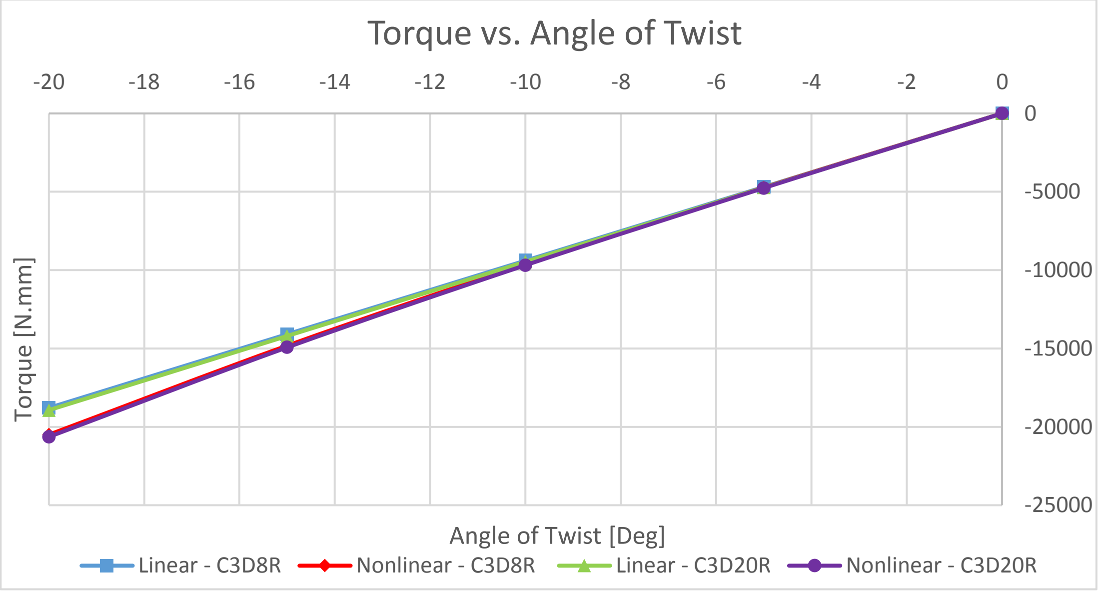

Figure 3.16: Torque - Angle of Twist Curves for the Beams with Tabs

In-plane shear strain (ε_{12}) distributions of the beams are presented in Figures 3.17 – 3.20 for the FEM with C3D8R type of elements including nonlinear geometry effects. In-plane shear strain (ε_{12}) is maximum at the middle of the long edge, as expected.

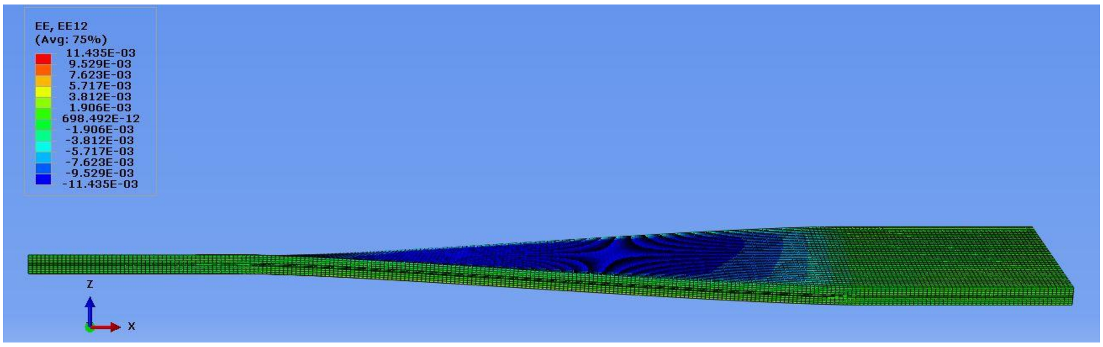

Figure 3.17: In-plane Shear Strain (ε_12) Distribution for the Beams without Tabs

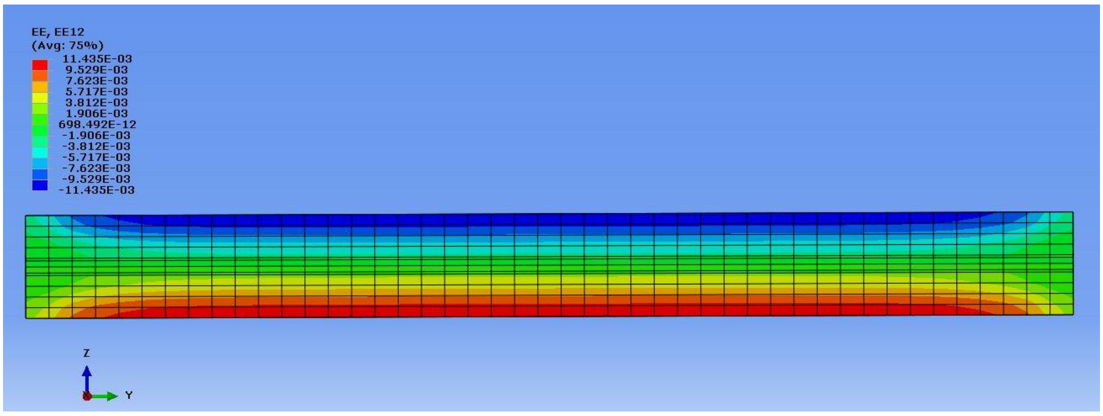

Figure 3.18: Cross Section View of In-plane Shear Strain (ε_12) Distribution at the Middle of the Beam for the Beams without Tabs

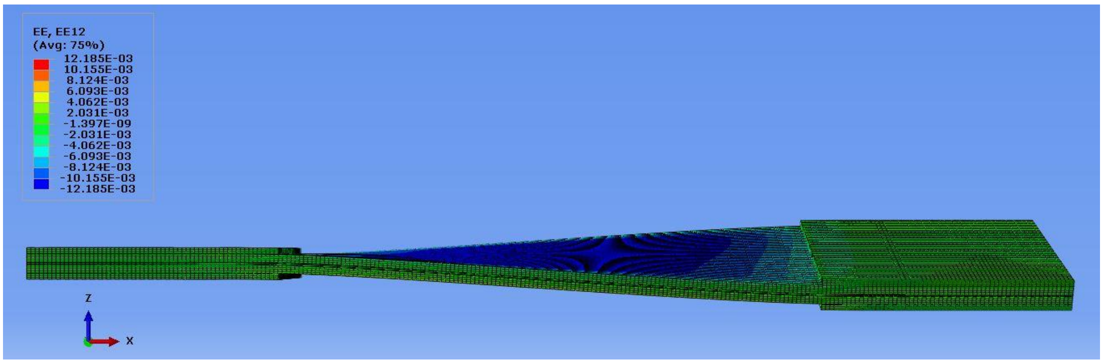

Figure 3.19: In-plane Shear Strain (ε_12) Distribution for the Beams with Tabs

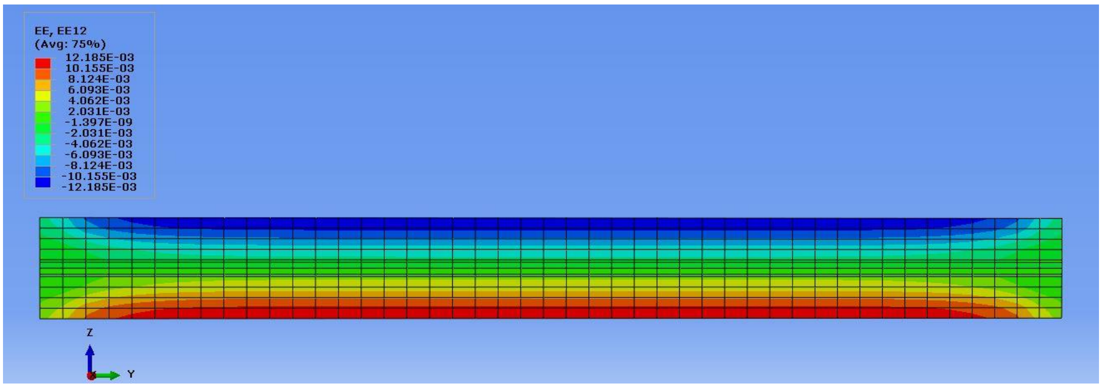

Figure 3.20: Cross Section View of In-plane Shear Strain (ε_12) Distribution at the Middle of the Beam for the Beams with Tabs

Maximum in-plane shear strain (ε_{12}) - angle of twist curves for the beams are presented in Figure 3.21 and Figure 3.22. Shear strain results are greater for the FEA with C3D20R element than C3D8R element. In addition, shear strain results do not get affected from inclusion of nonlinear geometry.

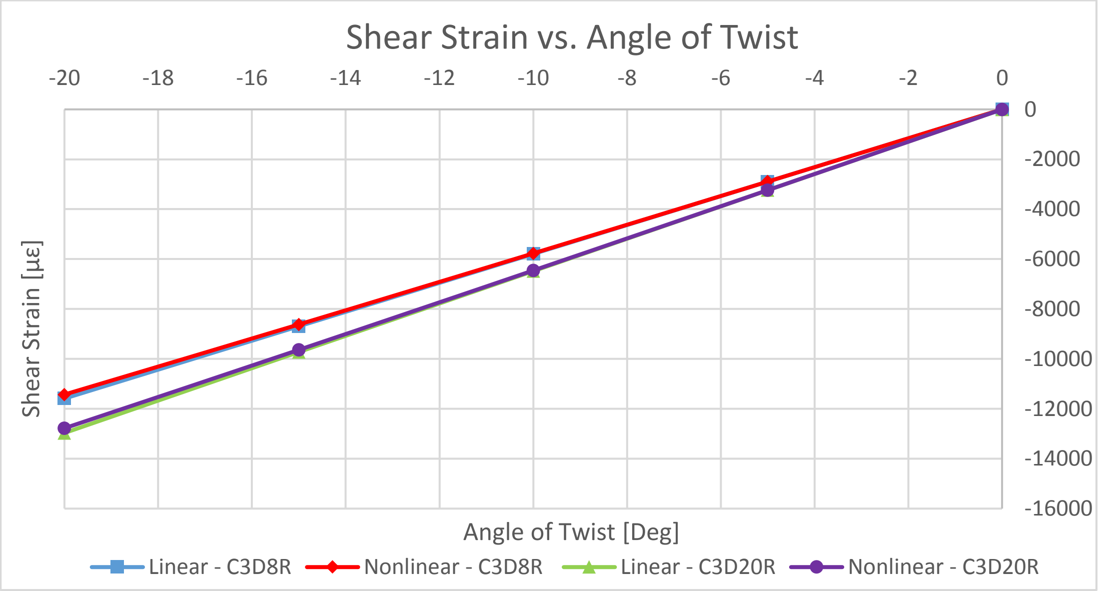

Figure 3.21: Shear Strain - Angle of Twist Curves for the Beams without Tabs

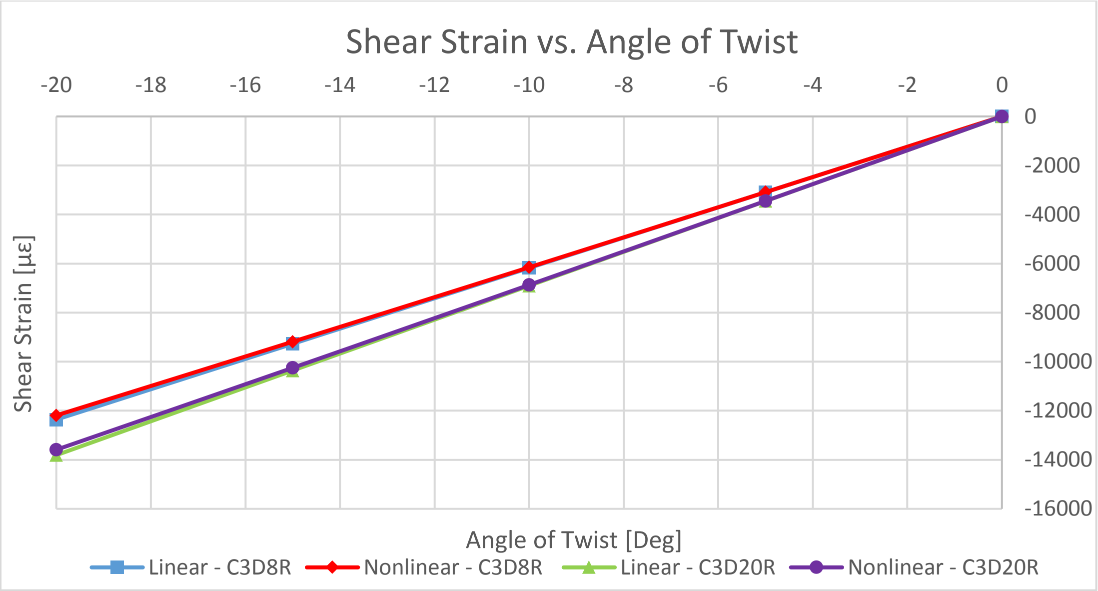

Figure 3.22: Shear Strain - Angle of Twist Curves for the Beams with Tabs

Torque vs. shear strain graphs for the beams are presented in Figure 3.23 and in Figure 3.24. Slope of the curves are greater for the FEA including nonlinear effects for the same type of finite element. In addition, slope of the curves are greater for the FEA conducted with C3D8R elements.

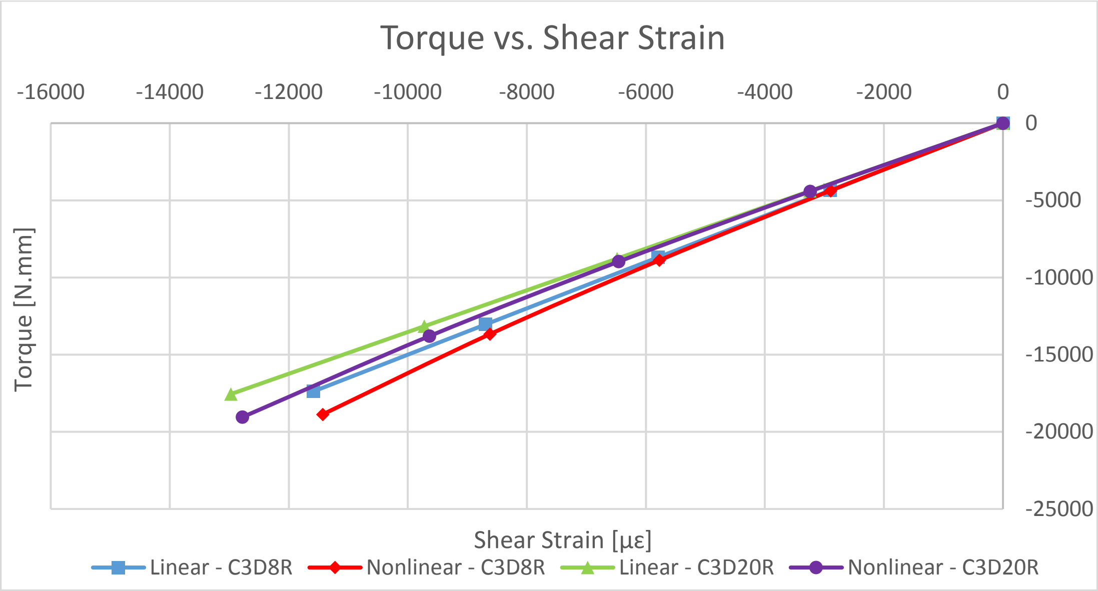

Figure 3.23: Torque vs. Shear Strain for the Beams without Tabs

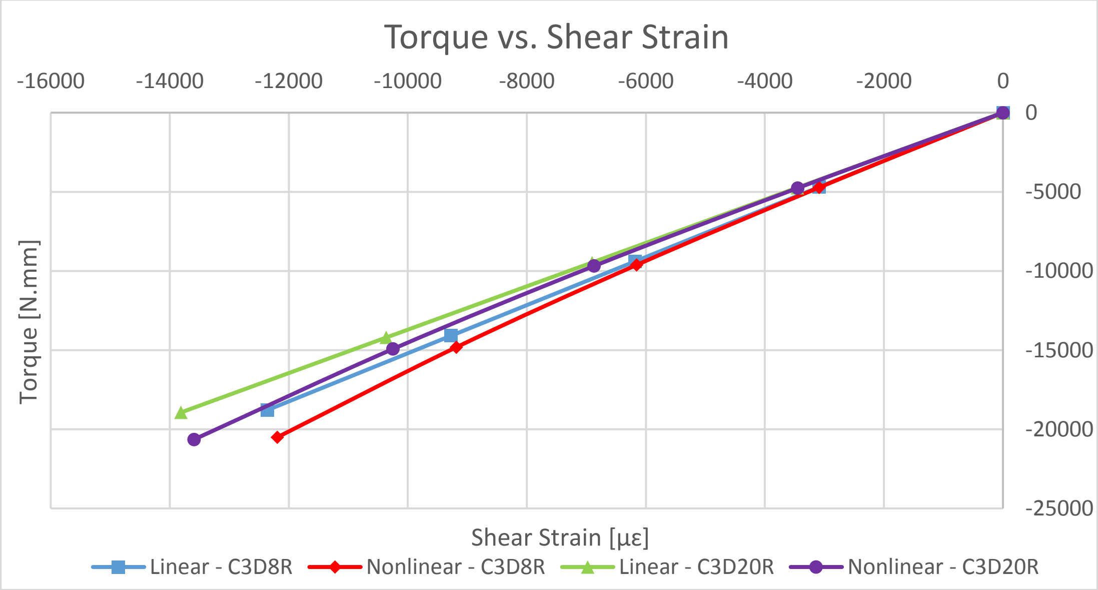

Figure 3.24: Torque vs. Shear Strain for the Beams with Tabs

3.4 Conclusion

In this chapter, FEM development of composite beams under torsional load were explained in detail. FEA were performed for 20° of angle of twist where both geometric and material nonlinearity were expected. However, only geometrical nonlinearity was able to input into the FEM due to the unavailability of material properties in plastic region.

Maximum in-plane shear strain results were obtained at the middle of the long edges, as expected.

FEA results of the models generated with C3D8R and C3D20R finite elements were compared. Although torque results were the same for both elements, it has been found that shear strain results were greater for C3D20R elements. This might be caused by the fact that second order finite elements are more sensitive to distortions than first order finite elements [63].

The suitable FEM for the composite beams under torsional load will be decided by comparing the results of FEA and tests in Chapter 5.

CHAPTER 4

TORSION TESTS OF COMPOSITE BEAMS EQUIPPED WITH FIBER BRAGG GRATING SENSORS

4.1 Introduction

In this chapter, torsion tests of the composite beams equipped with Fiber Bragg Grating (FBG) sensors are presented. First, geometrical and material properties of the beams and placement of the FBG sensors over the beams are described in detail. Then, the FBG sensor system including FBG sensors and interrogator system is introduced. In addition, method of manufacturing and the problems encountered during the procedure are explained. Later, the test procedure and the results of the torsion tests are presented. Finally, a case study to compare the results of the shear strains obtained from FBG sensor and strain gage is outlined.

4.2 Geometrical and Material Properties of the Composite Beams

Six composite beams, four of which without tabs and two of which with tabs, were prepared for the torsion tests. In this section, geometry and material properties of the composite beams are explained.

Top view and side view of the beams without tabs are presented in Figure 4.1 and Figure 4.2. Dimensions of the beams without tabs are 250 mm x 45 mm x 4.42 mm.

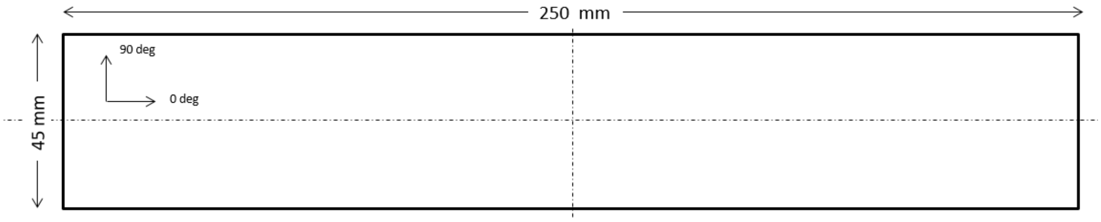

Figure 4.1: Top View of the Beams without Tabs

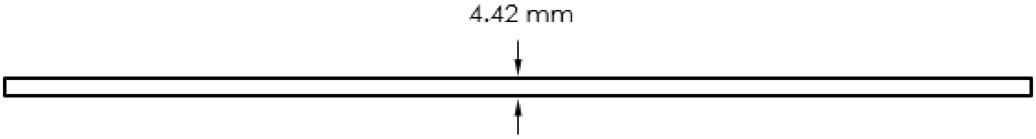

Figure 4.2: Side View of the Beams without Tabs

Top view and side view of the beams with tabs are given in Figure 4.3 and Figure 4.4. Length and width of the beams with tabs are 250 mm and 45 mm, respectively. The thickness at the middle of the beam is 4.42 mm, whereas the thickness at the end of the beams with the tabs is 7.46 mm.

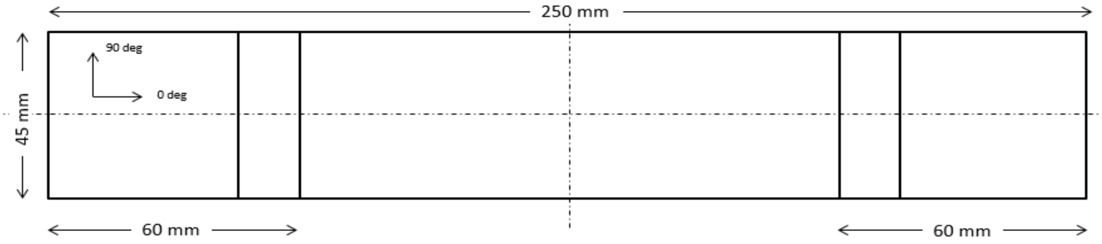

Figure 4.3: Top View of the Beams with Tabs

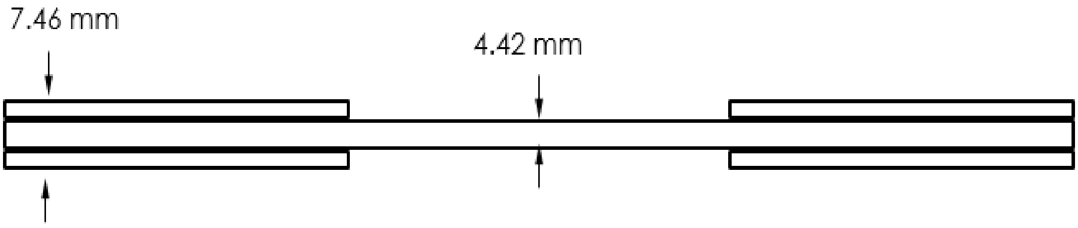

Figure 4.4: Side View of the Beams with Tabs

Layup of the beams is presented in Figure 4.5, which consists of unidirectional glass/epoxy composite layers, woven glass/epoxy composite layers and thermosetting epoxy film adhesive strips with the stacking sequence

$$[0_8/Film/(\mp 45)_{Woven}/(\mp 45)_{Woven}/Film/0_8].$$

The layup sequence is visualized in Figure 4.5, which presents the cross sectional view of the beams.

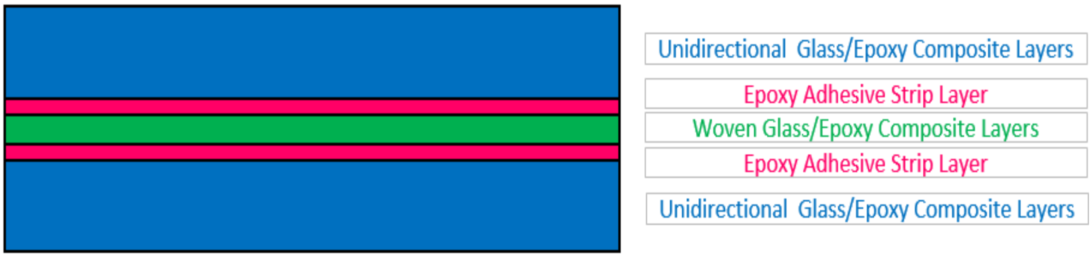

Figure 4.5: Cross Sectional View of the Beams

Tab material is woven glass/epoxy composite materials and the adhesive which bonds the beams and tabs together is thermosetting epoxy film adhesive strips.

4.3 Placement of FBG Sensors

In this section, placement of the FBG sensors on six composite beams will be explained.

Position of the FBG sensors on longitudinal, transverse and thickness directions are presented in Table 4.1. Notice that the beams with tabs contain double “T” in their name (S1TTUD and S1TTW). Positions of the FBG sensors in thickness direction are demonstrated in Figure 4.6 in detail using the cross sectional view of the beams.

Table 4.1: Positions of the FBG Sensors in Longitudinal, Transverse and Thickness Directions

	The Beam	**FBG**	**Position**		
			Longitudinal	**Transverse**	**Thickness**
The Beams without Tabs	**S1TUD**	FBG1	Middle	Middle	Surface
		FBG2	Middle	Middle	Embedded between UD
	S1TW	FBG1	Middle	Middle	Surface
		FBG2	Middle	Edge	Embedded between Woven
	S2T	FBG1	Middle	Middle	Surface
		FBG2	Middle	Middle	Embedded between UD
		FBG3	Middle	Edge	Embedded between Woven
	S3T	FBG1	Middle	Middle	Surface
		FBG2	Middle	Middle	Surface

The Beams with Tabs	The Beam	FBG	Position		
			Longitudinal	**Transverse**	**Thickness**
	S1TTUD	FBG1	Middle	Middle	Surface
		FBG2	Middle	Middle	Embedded between UD
	S1TTW	FBG1	Middle	Middle	Surface
		FBG2	Middle	Middle	Embedded between Woven

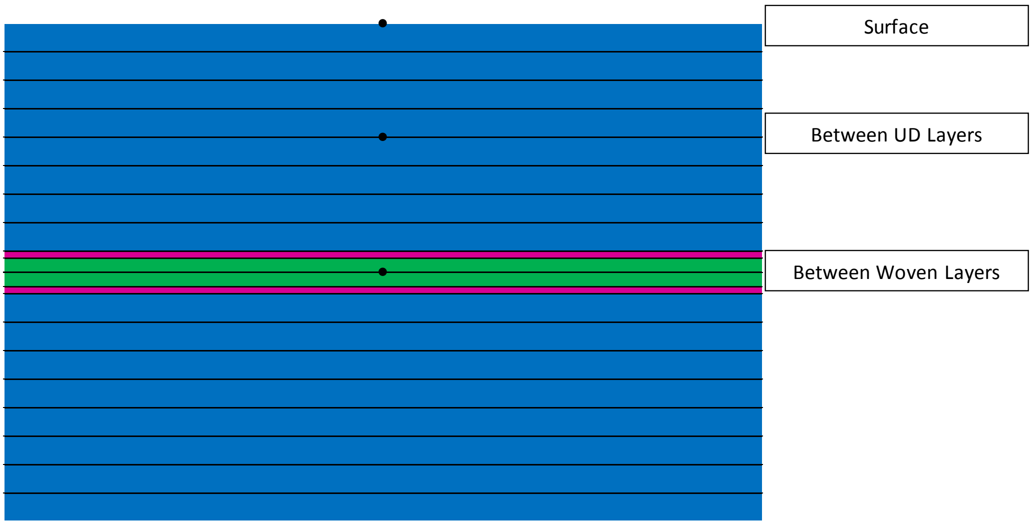

Figure 4.6: Positions of FBG Sensors in Thickness Direction (Cross Sectional View)

In the literature, there are studies for strain measurement with FBG sensors on cylindrical parts under torsional load. In general, two FBG sensors are placed in +45° and -45° configuration to compensate the temperature effect [50], [64]–[66]. However, Tian and Tao uses only one FBG sensor two measure the torque of a shaft claiming that if the measurement is at room temperature and the temperature variation is small, the temperature effect could be neglected [67]. Therefore, assuming test conditions do not change much through the tests, single FBG sensor could be used for measurements.

All the sensors are planned to be in alignment with the ±45° direction from longitudinal axis such that the in-plane shear strain is obtained using the strain transformation Equation 4.1.

$$\varepsilon_{fbg} = \varepsilon_{11} cos^2\theta + \varepsilon_{22} sin^2\theta + \gamma_{12} sin\theta cos\theta \qquad \boxed{4.1}$$

where

ε_{fbg}: Strain measured by the FBG sensors

ε_{11}: Strain in longitudinal direction

ε_{22}: Strain in transverse direction

γ_{12}: In-plane shear strain

θ: Angle between the longitudinal axis and the line on which FBG sensors are positioned

Assuming strains in longitudinal and transverse directions are small relative to the in-plane shear strain, we obtain Equation 4.2 to calculate the in-plane shear strain from the strain measured using FBG sensor.

$$\varepsilon_{fbg} = \gamma_{12} sin\theta cos\theta \qquad \boxed{4.2}$$

For θ =45°, Equation 4.3 is obtained.

$$\varepsilon_{fbg} = \gamma_{12} sin45° cos45° \tag{4.3}$$

The strains measured with FBG sensors are transformed to shear strains using the Equation 4.4.

$$\gamma_{12} = 2\varepsilon_{fbg} \tag{4.4}$$

4.4 The Fiber Bragg Grating Sensor System Utilized During the Torsion Tests

The system utilized during the torsion tests to measure the strains consists of embedded or surface mounted FBG sensors, an interrogator system that reads and processes data obtained from the sensors and a personal computer, which has the software to monitor the data and command the system for measurements. Following subsections include the specifications of the FBG sensors and the interrogator system used during the study.

4.4.1 Specifications of Fiber Bragg Grating Sensors

In this study, embedded and surface mounted FBG sensors are used to measure the strain caused by torsional load applied to composite beams.

Working principle of FBG sensors is based on tracking the wavelength of the reflected light. Gratings reflect the light with a unique wavelength, which is called Bragg wavelength acquired by a peak-picking algorithm using the interrogator and SmartSoft software. When there is elongation or retraction on the sensors, the Bragg wavelength changes. The changes of the wavelength are transformed into the strain measurements by algorithms.

Bragg wavelength of the FBG sensors used for this study is 1550 ± 0.5 nm. Fiber optic cables contain single FBG sensor with a length of 10 mm. The Bragg wavelength of one of the sensors is tracked online using Smartsoft software [68] as 1549.96 nm, which is presented in Figure 4.7.

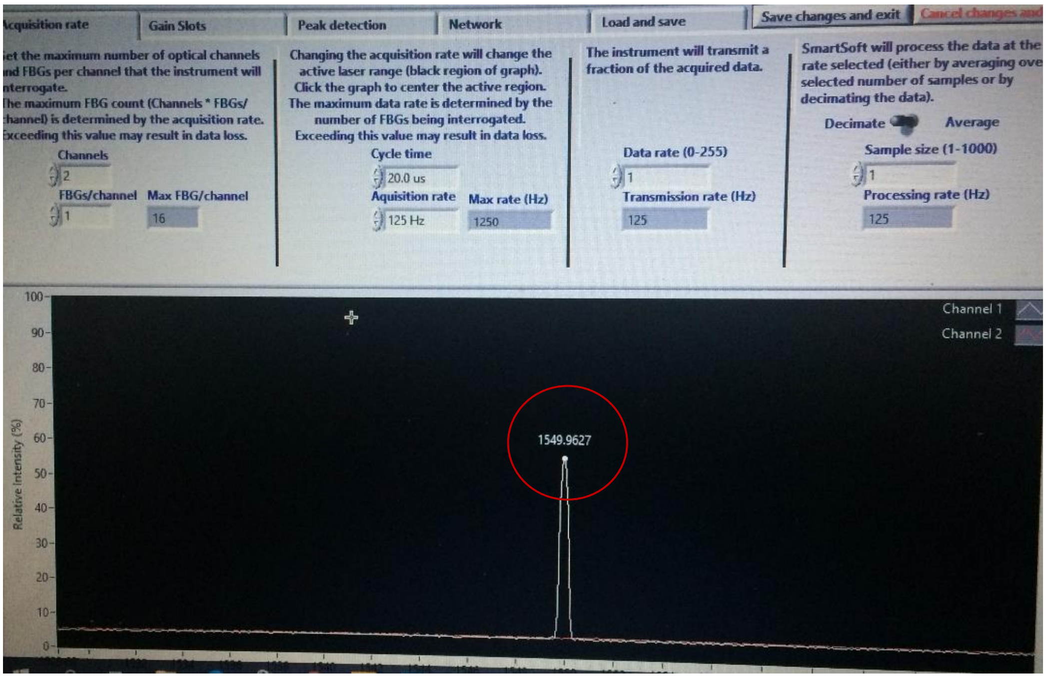

et the maximum number of optical channels nd FBGs per channel that the instrument will nterrogate.
he maximum FBG count (Channels * FBGs/ hannel) is determined by the acquisition rate. xceeding this value may result in data loss.

Channels: 2
FBGs/channel: 1
Max FBG/channel: 16

Changing the acquisition rate will change the active laser range (black region of graph). Click the graph to center the active region. The maximum data rate is determined by the number of FBGs being interrogated. Exceeding this value may result in data loss.

Cycle time: 20.0 us
Aquisition rate: 125 Hz
Max rate (Hz): 1250

The instrument will transmit a fraction of the acquired data.

Data rate (0-255): 1
Transmission rate (Hz): 125

SmartSoft will process the data at the rate selected (either by averaging ove selected number of samples or by decimating the data).

Decimate ● Average
Sample size (1-1000): 1
Processing rate (Hz): 125

Figure 4.7: Bragg Wavelength of Single FBG Sensor [68]

All the fiber optic cables containing the FBG sensors have polyimide coating which enables superior strain transfer with a durability until 300°C [44]. This polyimide coating could be removed from the surface only after softening the material with a flame and pulling it with a tissue by force.

4.4.2 Interrogator System

Interrogator is a laser source that beams the light into the fiber optic cable. In addition, interrogator is the system to process data obtained from the FBG sensors. Interrogator used in this study is called SmartScan Aero which is a compact and robust interrogator that could be used for dynamic measurements which is presented in Figure 4.8 [69]. It has four optical channels to connect four fiber optic cable with 16 FBG sensors per channel. The interrogator is connected to the personal computer via Ethernet port such that data is collected using SmartSoft software.

Figure 4.8: SmartScan Aero Interrogator [69]

High-resolution interrogation is possible with The SmartScan Aero interrogator at multi-kHz frequencies. Maximum scanning frequency is 25 kHz; however, 2.5 kHz is suggested for simultaneous measurement of the sensors [69].

Fiber optic cables are connected to the interrogator via pigtail connectors. Fiber optic cable, FBG sensor and pigtail connecter are presented in Figure 4.9.

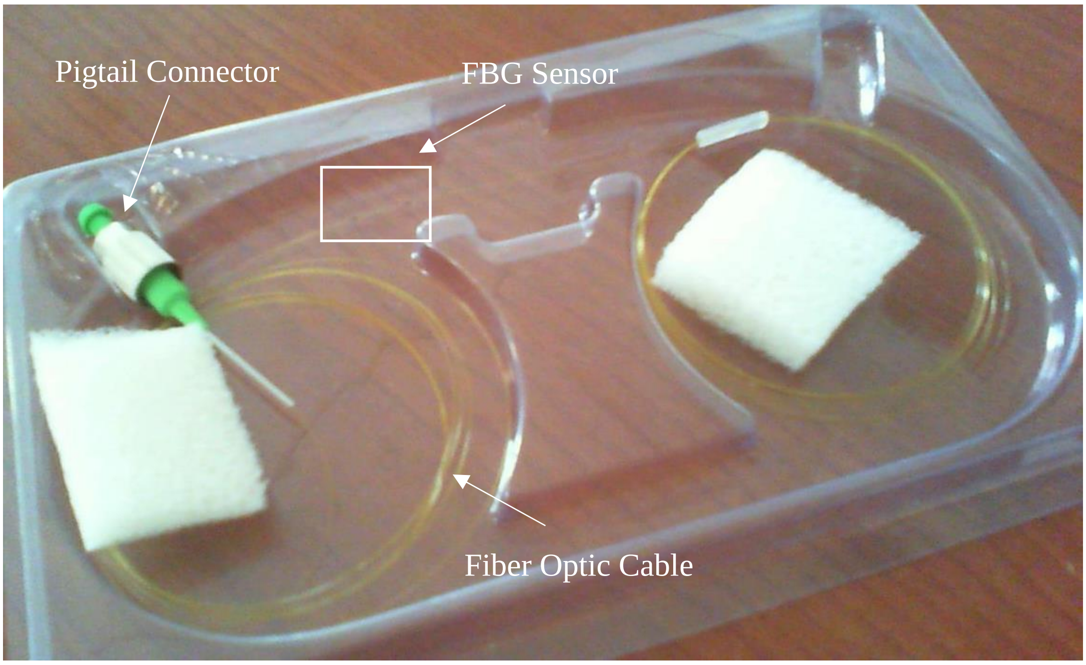

Figure 4.9: Fiber Optic Cable with Pigtail Connector

4.5 Manufacturing of the Composite Beams with Embedded and Surface Mounted FBG Sensors

In this section, manufacturing methods for the composite beams with embedded FBG sensors are presented. In addition, the problems encountered during the process along with the solutions are discussed.

All the composite layers used for manufacturing were prepreg composite layers, i.e. the fiber cloths were impregnated with resin beforehand. Prepreg layers were cut in their dimensions before the layup process using the cutting machine for composites and industrial fabrics, as seen in Figure 4.10. However, in width direction, prepreg layers were cut a little longer than designed for the purpose of scraping the excess material and obtaining smooth free edges.

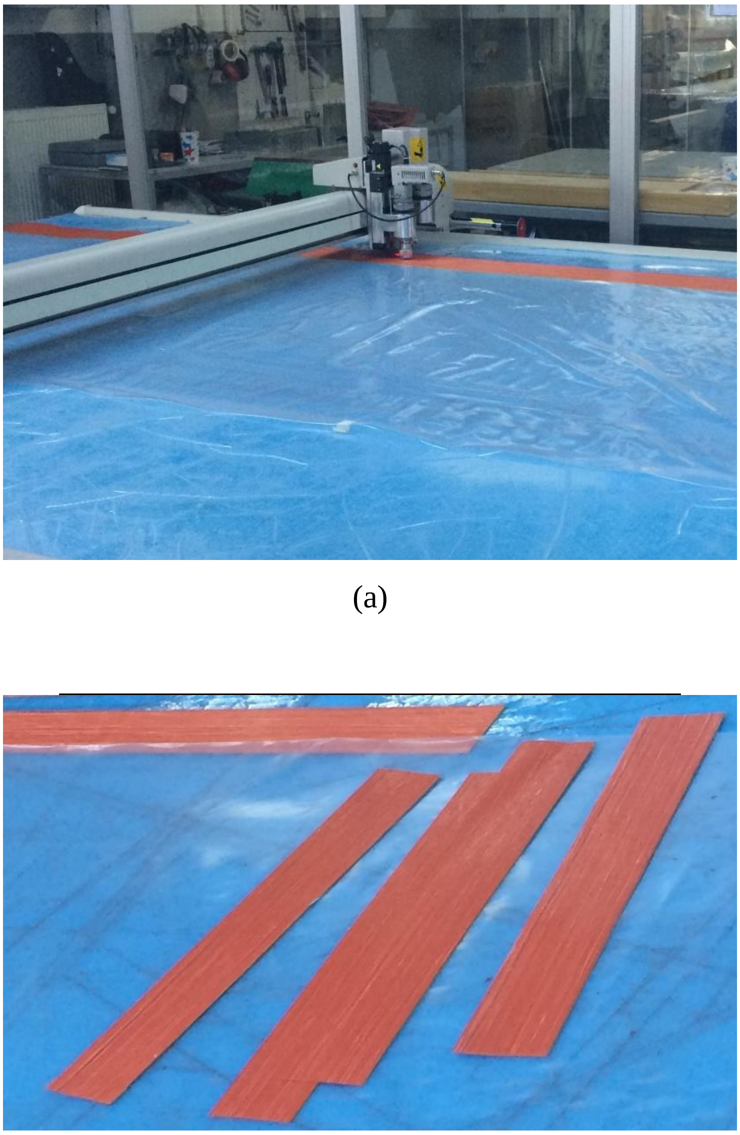

(a)

(b)

Figure 4.10: (a) Composite Cutting Machine (b) Prepreg Layers

The layup process of composite beams was performed on the same plate, which allowed the beams to be cured together in one cure cycle such that any differences in material properties due to the temperature and pressure during curing were eliminated.

Layup of the beam was continued until the layer on which the FBG sensor will be placed. Before placement of the FBG sensor, beam was put under vacuum to eliminate sliding of the layers as shown in Figure 4.11.

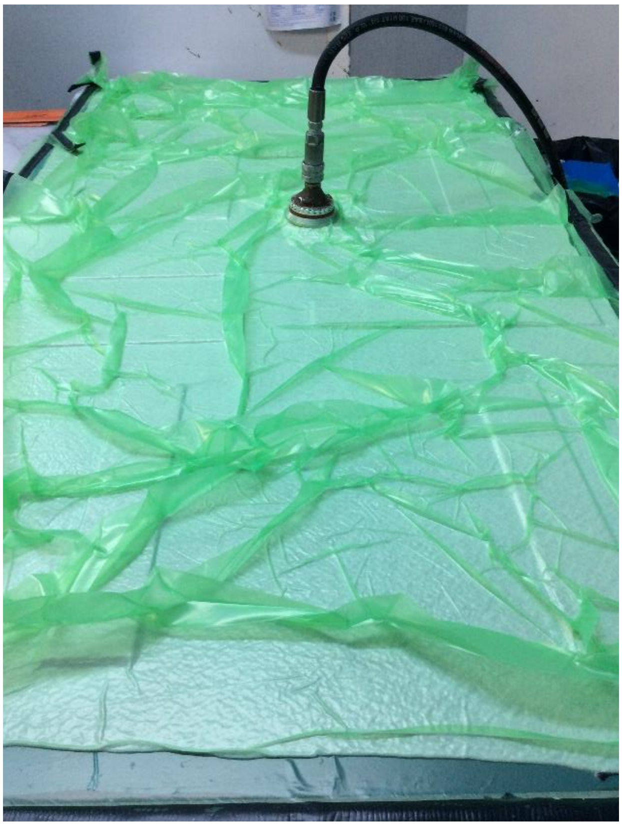

Figure 4.11: The Plate under Vacuum

The health of the FBG sensors was ensured before the layup process by connecting them to the interrogator system and observing their wavelength.

In literature, stress concentrations on fiber optic cables are expected at the ingress and egress sections. As a solution, Teflon tubes were used to avoid breakage of the fiber optic cables as seen in Figure 4.12.

FBG sensors were aligned with 45° from the longitudinal axis and fiber optic cables were evacuated from the region that will stay between the grips of the test machine to obtain an adequate working space as in Figure 4.13.

Throughout the process, the curvature of the fiber optic cables was arranged such that minimum optical loss was sustained.

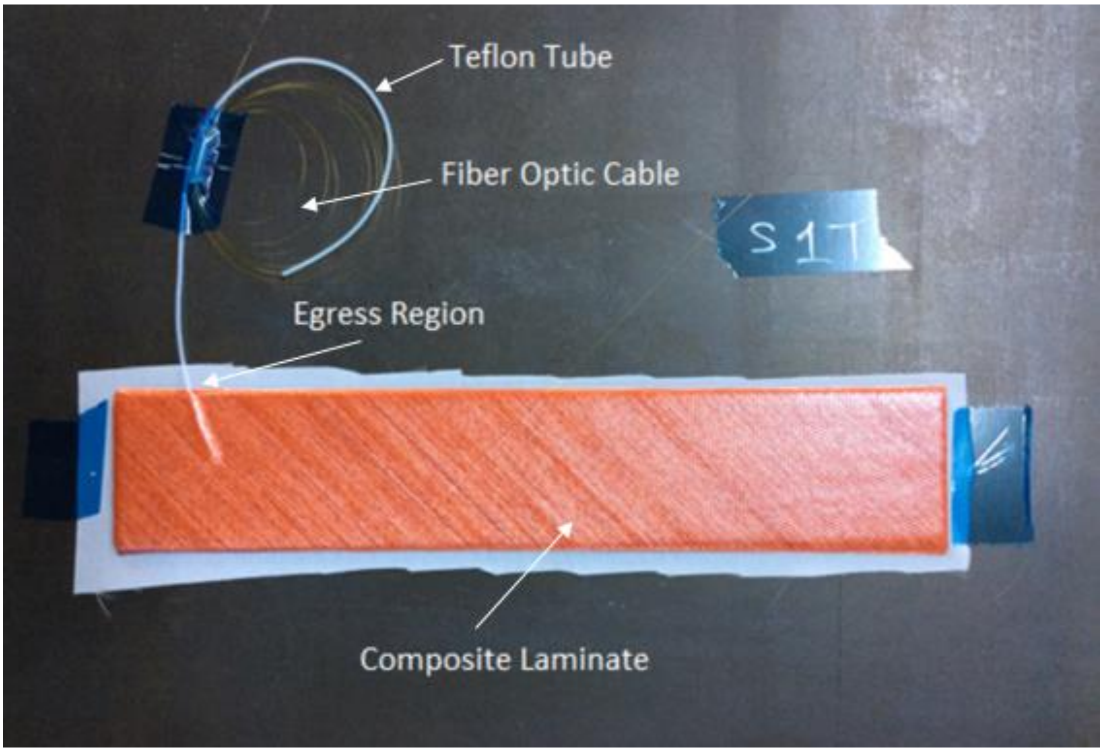

Figure 4.12: Fiber Optic Placement with Teflon Tube at Egress Region

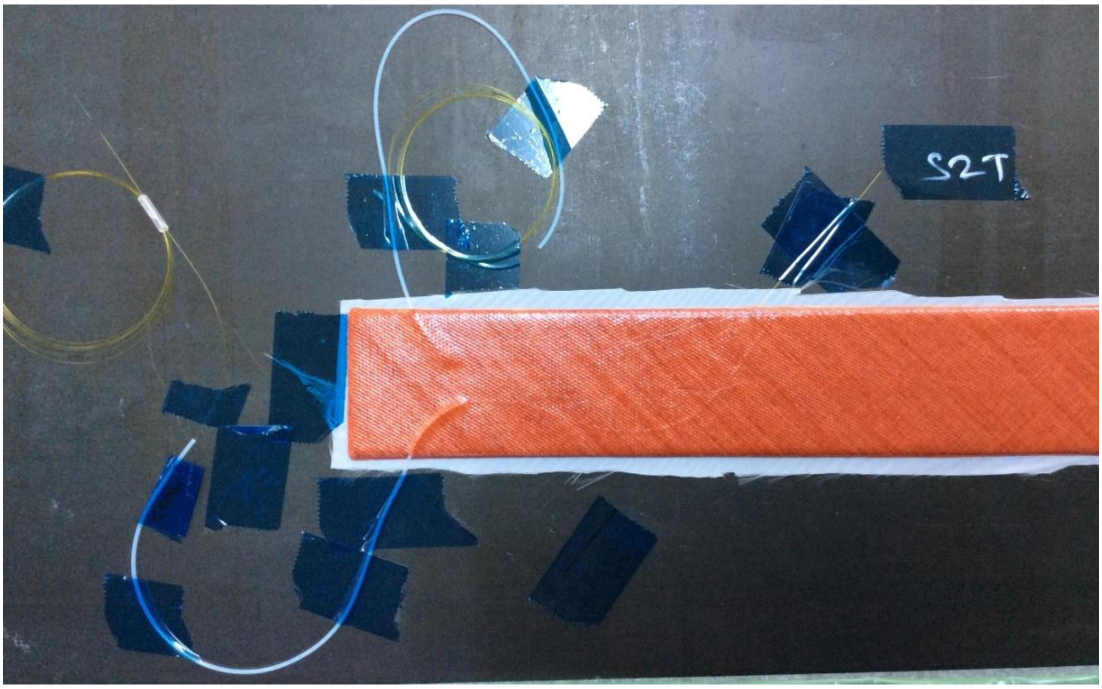

Figure 4.13: Evacuation of the Fiber Optic Cables

After FBG sensors were placed between the layers as planned, the plate was again put under vacuum. After vacuuming process, the health of the FBG sensors was controlled again to check whether the vacuuming led to any damage to the sensors. Then, layup was proceeded to complete the beam. Before curing, the pigtail connections, which were used to connect the fiber optic cables to the interrogator system, were cut to avoid the melting. Beams that were ready for the curing process could be seen in Figure 4.14.

Figure 4.14: Beams with Embedded FBG Sensors Ready for the Curing Process

After curing, it was seen that resin flowed in and over the Teflon tubes, although the fiber optic cables were isolated from the beam area using isolation bands as presented in Figure 4.15. During the tests, resin accumulated regions around the Teflon tubes were treated with care to avoid fiber optic sensor breakage.

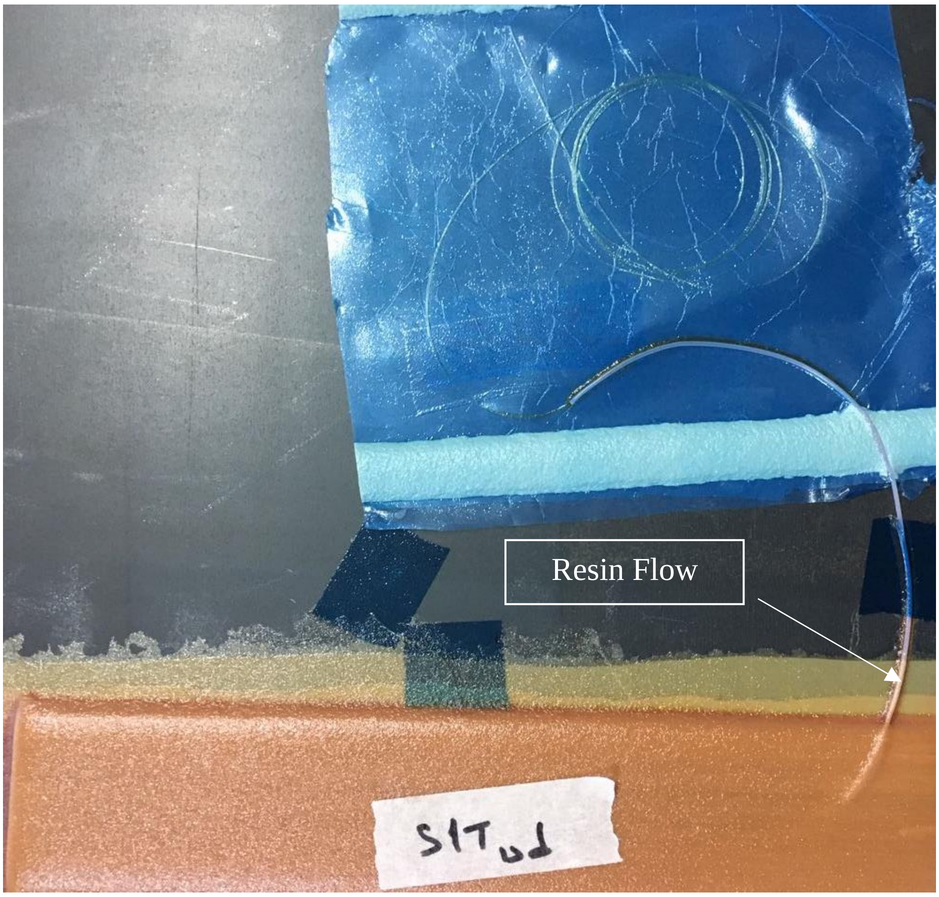

Figure 4.15: Resin Flow in and over the Teflon Tubes

After curing, the excess resin around the beams are cut using ribbon saw to obtain smooth edges as in Figure 4.16.

Figure 4.16: S2T with Smoothened Edges

Tabs were secondarily bonded to the composite beams to obtain the beams with reinforcements.

In addition, Pigtail connecters were reconnected to the fiber optic cables using splicer device, Fujikura 70S Fusion Splicer. Splicer is a device, which sends sparks to the junction and joins the two parts together [70].

Figure 4.17: Fujikura 70S Fusion Splicer [70]

Splicer is also used to reinforce the junction region by covering it with a plastic tube as seen in Figure 4.18.

Figure 4.18: Plastic Tube around the Junction Region

Process of manufacturing composite beams with embedded FBG sensors is summarized in Figure 4.19.

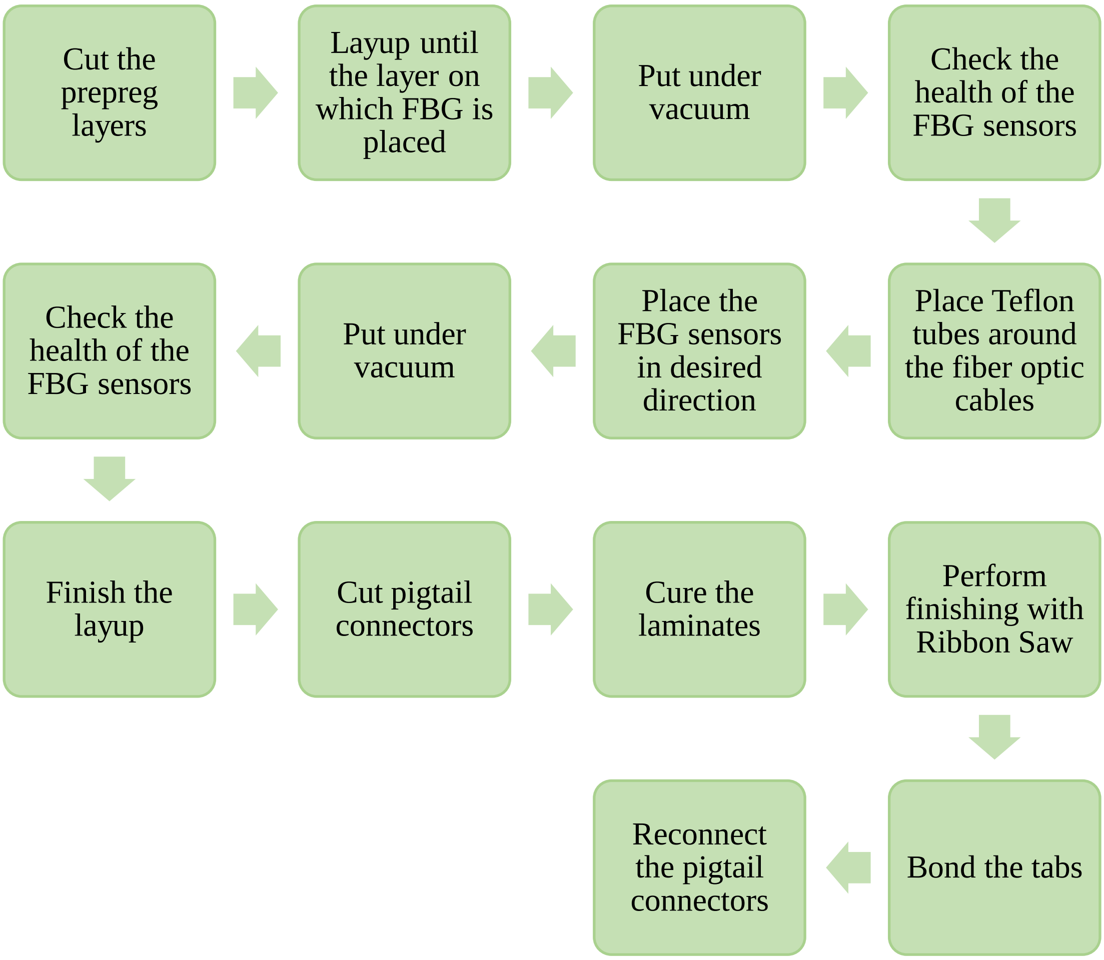

Figure 4.19: The Manufacturing Process of Composite Beams with Embedded FBG Sensors

Finally, the FBG sensors on the surfaces are mounted on the composite beams using an industrial liquid adhesive, M-Bond 200.

4.6 Properties of the Test Machine

Torsion tests of composite beams are conducted using MTS 809 Axial/Torsional Test System presented in Figure 4.20 which is a hydraulic testing machine capable of applying axial and torsional load at the same time having 100 kN dynamic load capacity [71]. The test machine, which is setup in RUZGEM laboratories, has been calibrated by the company personnel in 2015.

Figure 4.20: MTS 809 Axial/Torsional Test Machine

Grips of the testing machine are 647 all-temperature hydraulic wedge grips [72]. Flat and vee wedges with flat surfaces are used during the test, which are convenient for specimens having rectangular cross section with flat surfaces as presented in Figure 4.21.

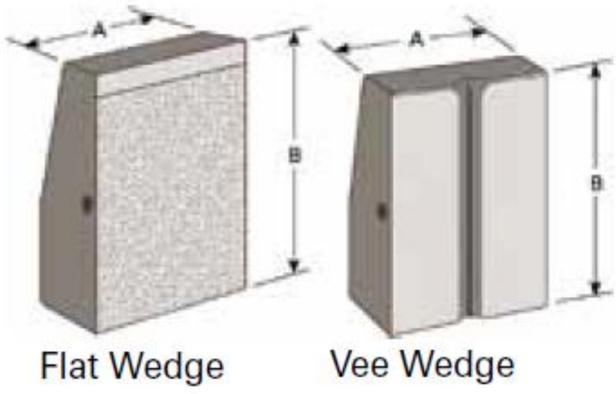

Figure 4.21: Wedges Utilized for the Torsion Tests [72]

4.7 Procedure for the Torsion Tests

Great care is required while placing the composite beams between the wedges with a correct alignment. Any misalignment might cause application of undesired loads on the beams, which may cause premature failures.

A composite beam without any sensor was mounted on the machine to decide whether the parameters that are input to the software are convenient for the desired torsion test.

As boundary conditions, one end of the beams was fixed and the other end was allowed to move around longitudinal axis in rotational displacement control and to move in axial direction in force control to ensure that any axial stress on the beams was eliminated.

Figure 4.22 presents a composite beam without sensors, which was twisted for a 45° of angle of twist.

Figure 4.22: Composite Beam Twisted for a 45 Degrees of Angle of Twist

Torque is measured by the load cell on testing machine with 20 Hz of sampling frequency. Torque - angle of twist curve is presented in Figure 4.23. The curve is obtained by linear regression analysis of the data to avoid the offset and data distortion problems. In addition, it can be observed that axial force was nearly zero from Figure 4.24, and the beam actually moved in axial direction as desired from Figure 4.25.

The results of the torsion test of the composite beam without any sensors to control whether the system works properly showed that it is convenient to proceed the tests of the composite beams with embedded and surface mounted FBG sensors.

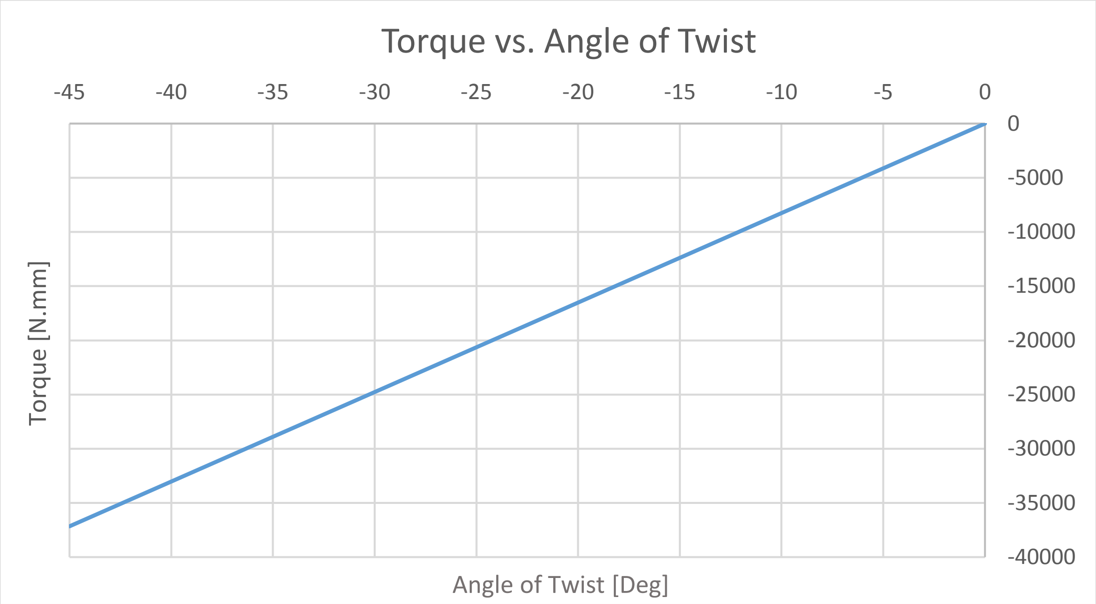

Figure 4.23: Change of Torque with Angle of Twist for the Beam without Any Sensor

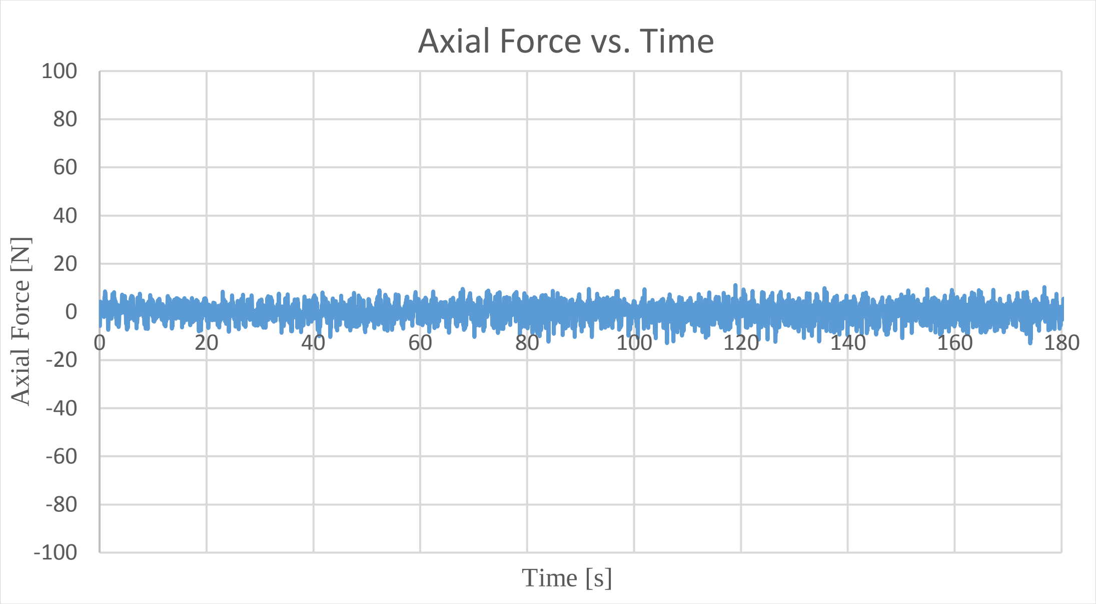

Figure 4.24: Change of Axial Force with Time for the Beam without Any Sensor

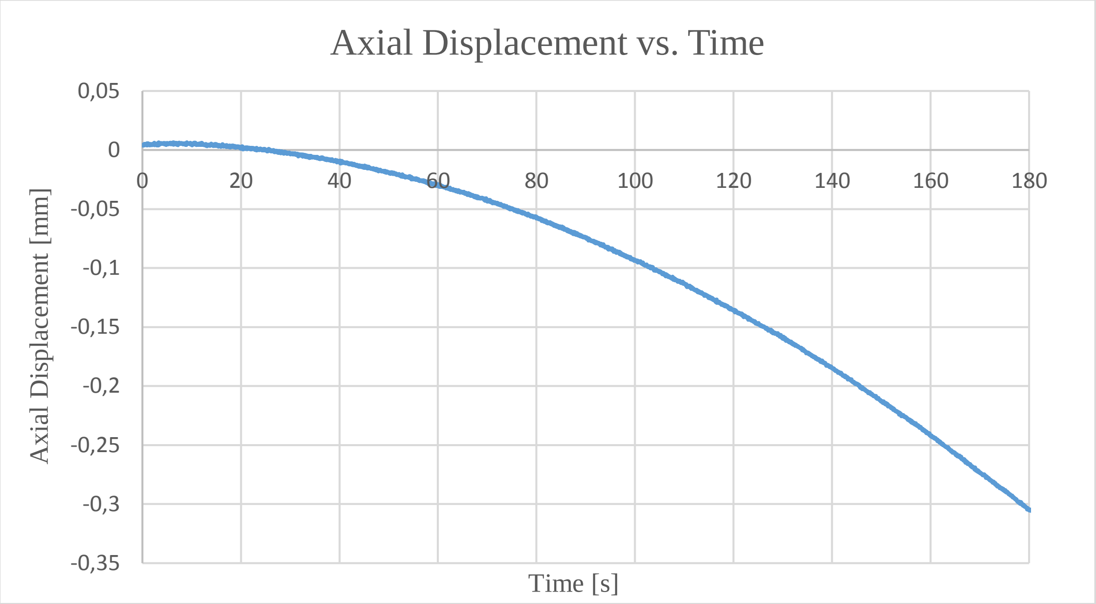

Figure 4.25: Change of Axial Displacement with Time for the Beam without Any Sensor

Each specimen was tested under torsional load three times to demonstrate reproducibility.

The test parameters for the three tests of each laminate are presented in Table 4.2.

Observe that the grip pressure was reduced to 500 psi after identifying embedded fiber optic cable damage between the grips for the laminates S1TW and S1TUD. Position of the fiber optic cable breakage was confirmed using a laser light source as presented in Figure 4.26. The laser light escapes from the damaged parts of the fiber optic cable and becomes visible, which helps to identify the problematic portions. Tabs were another solution to protect the fiber optic cables from the breakage due to grip pressure.

A different problem was the differences in thickness values of the laminates due to manufacturing errors. Figure 4.27 presents unexpected cambering due to Teflon tubes at the tab region of S1TTUD. As a solution, vee-serrated wedges were used, which have larger gap than flat wedges.

Finally, improper bonding of the FBG sensors on the surface of the S1TTUD led to the buckling of the sensors at high angle of twists. Distorted data is not presented in the results.

Table 4.2: Test Parameters for Each Specimen

The Beam	Test Number	Grip Pressure [psi]	Angle of Twist [Deg]	Wedge Type
S3T	Test 1	2000	20	Flat
	Test 2	2000	20	Flat
	Test 3	2000	20	Flat
S1TW	Test 1	2000	20	Flat
	Test 2	2000	20	Flat
	Test 3	2000	20	Flat
S2T	Test 1	500	20	Flat
	Test 2	500	20	Flat
	Test 3	500	20	Flat
S1TTW	Test 1	500	20	Flat
	Test 2	500	20	Flat
	Test 3	500	20	Flat
S1TTUD	Test 1	500	20	Vee-serrated
	Test 2	500	20	Vee-serrated
	Test 3	500	20	Vee-serrated

Figure 4.26: Fiber Optic Cable Breakage between the Grips (S1TTUD)

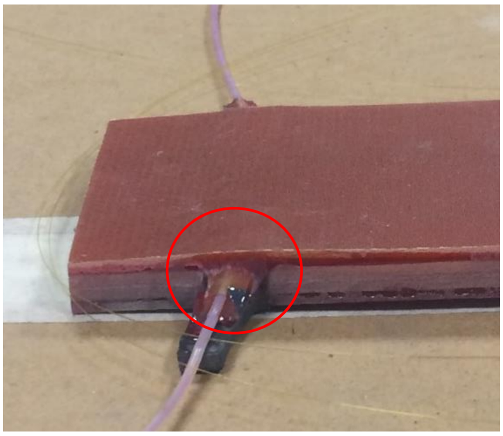

Figure 4.27: Cambered Region on S1TTUD due to Teflon Tubes

4.8 Results and Discussion of the Torsion Tests

In this section, torque and shear strain results are presented for all the beams. The tests were performed such that loading is followed by unloading for a set of test. Considering the fact that maximum permanent rotation between the loading and unloading was 1°, it is assumed that the tests are conducted in linear range. In addition, for both loading and unloading, it is observed that the torque and the shear strains change linearly with the angle of twist. Still, the curves are obtained by applying linear regression on the data to eliminate offset and data distortion problems.

Torque – angle of twist and shear strain – angle of twist curves obtained from the three tests are presented for each specimen to observe reproducibility in Figures 4.28 – 4.40. Shear strain values obtained from the FBG sensors placed between the woven layers are not presented in this section as graphs, since the values are nearly zero, as expected.

The axes bounds of all the graphs are kept the same for ease in comparison. Shear strain values obtained from FBG sensors on the surface are larger than the ones obtained from the FBG sensors between the UD layers, as expected.

Observe that in Figure 4.41, the shear strain data on the surface of S1TTUD is only available for one test, since the data obtained from the other tests were distorted due to buckling of the fiber optic cable. Distorted data is not presented in the graph.

All the torque and shear strain data at intervals of 5° of angle of twist for each beam could be found in tabular from in Appendix A.

Results of torque, shear strain on the surfaces and shear strain between UD layers demonstrate that the deviations from the average results of three tests for each beam are in the range of ±2%, as presented in Appendix B. Considering this result, it could be said that the repeatability of the tests are achieved.

In addition, statistical analysis is performed for results of torque, shear strain on the surface and shear strain between the UD layers obtained from the three tests. The equations used for the calculation of mean, standard deviation and the difference are presented in Appendix C. In addition, the calculated values for all the beams are demonstrated in Table C.1 in Appendix C. It is observed that maximum deviation of measurement from the mean value is 1.15σ, where σ is the standard deviation. There are three types of error, which are random errors (statistical errors), systematic errors (errors due to experimental apparatus) and personal errors (human errors). It is said that if the difference between one of the measurements and the mean is 2σ or greater than 2σ, then this behavior might be very likely due to systematic errors or personal errors [73]. Considering the maximum difference between the mean and a measurement is 1.15σ, one could conclude that the errors are due to random errors. However, performing the tests more than 30 times is suggested to reveal random errors [74].

Results of S3T

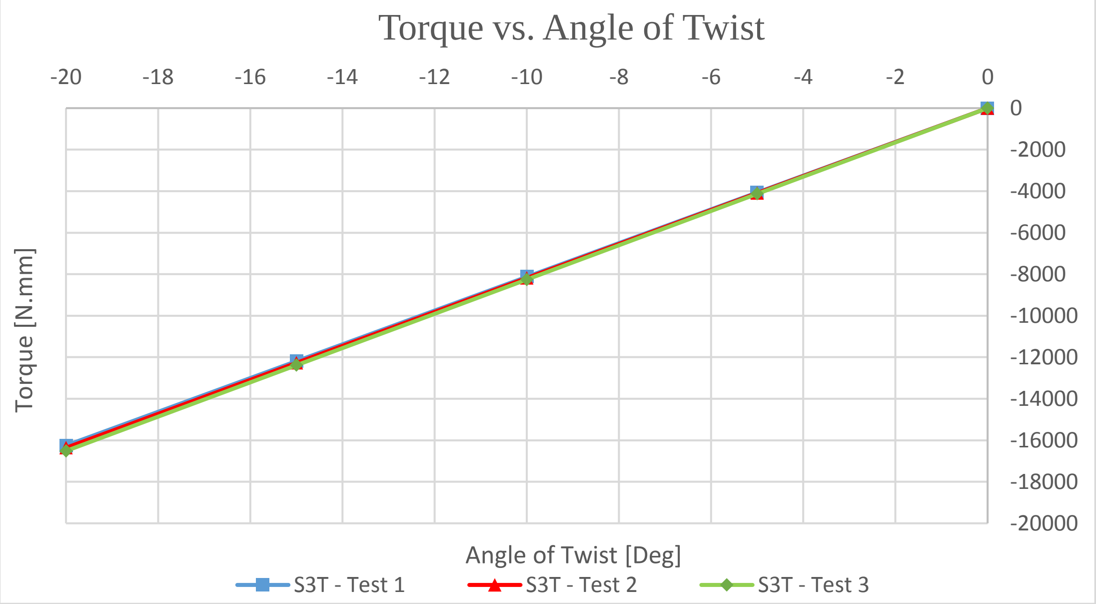

Figure 4.28: Torque - Angle of Twist Curves of S3T

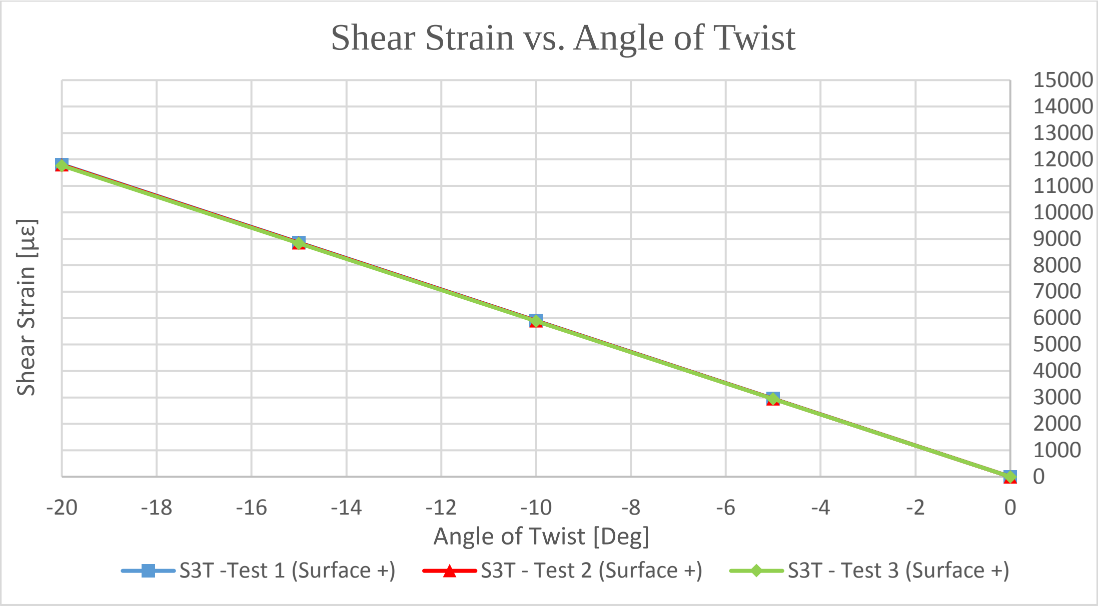

Figure 4.29: Shear Strain - Angle of Twist Curves from the FBG Sensor on the Surface of S3T

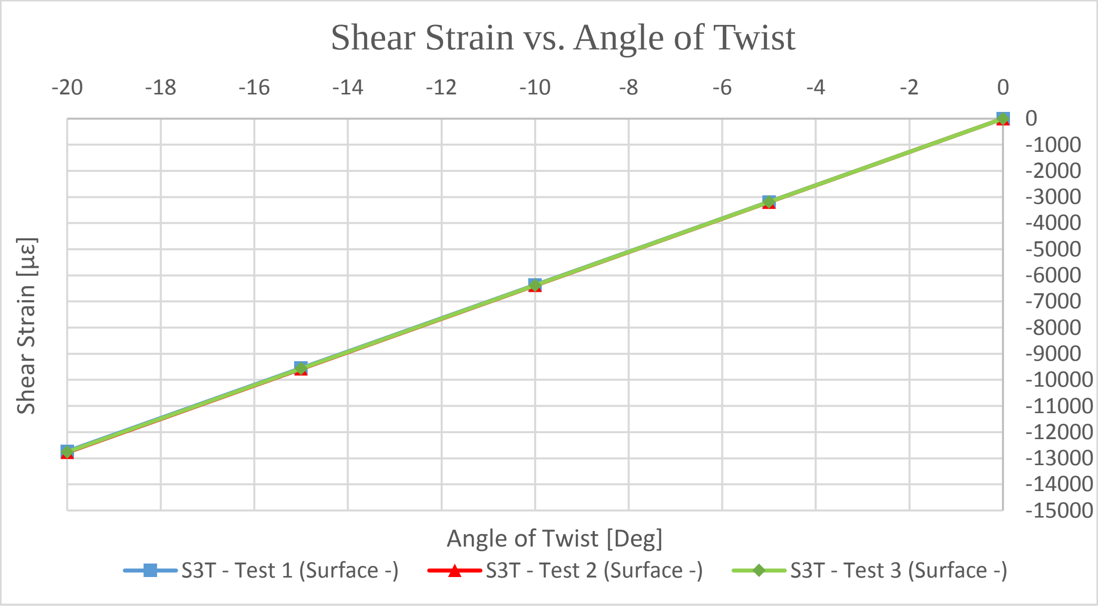

Figure 4.30: Shear Strain - Angle of Twist Curves from the FBG Sensor on the Other Surface of S3T

Results of S1TW

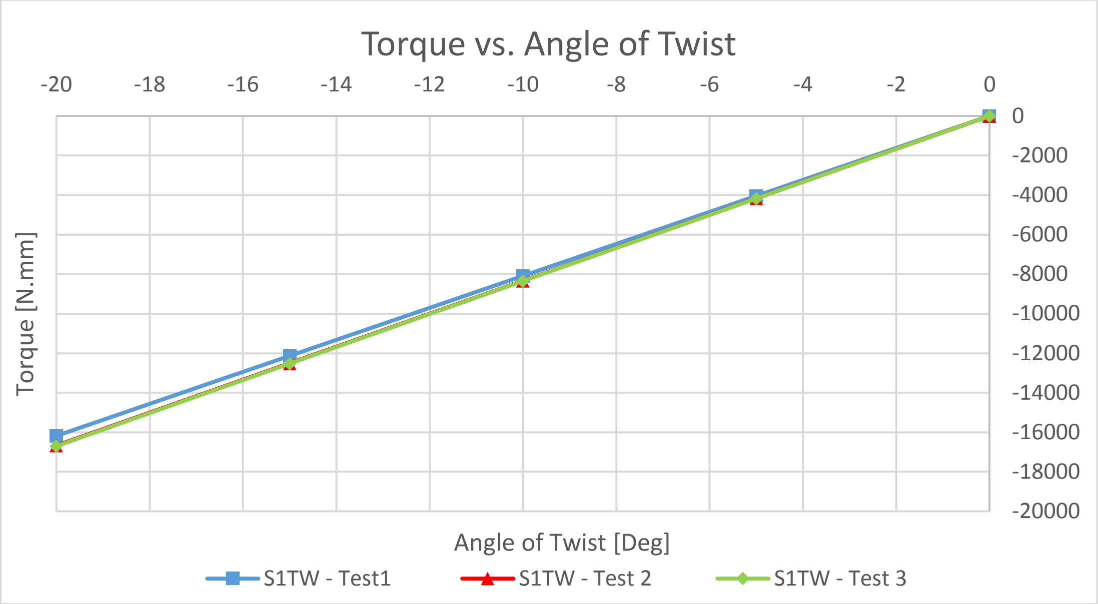

Figure 4.31: Torque - Angle of Twist Curves of S1TW

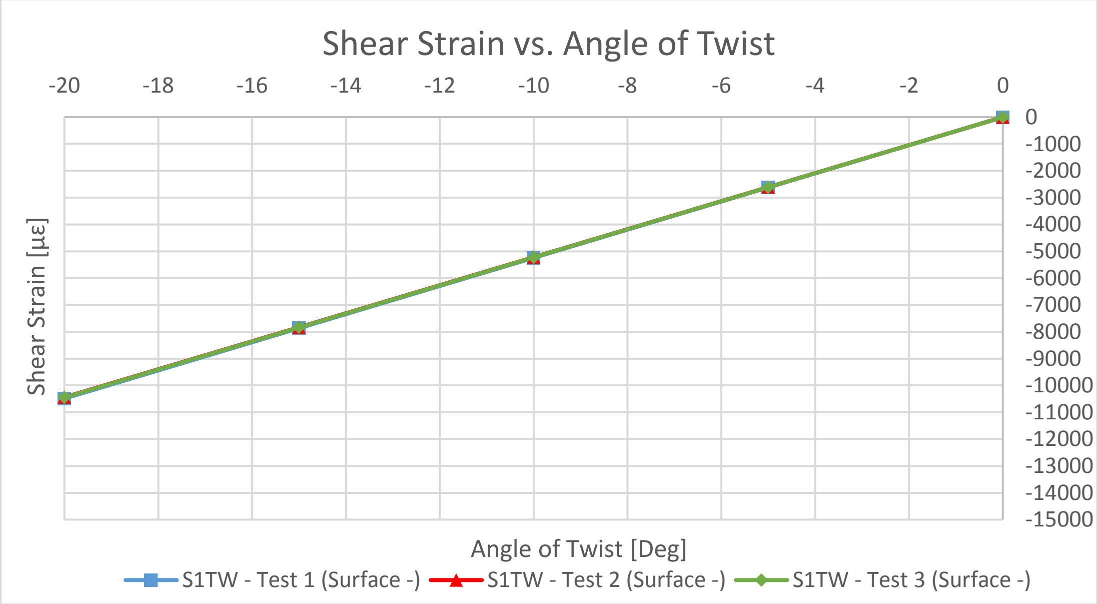

Figure 4.32: Shear Strain - Angle of Twist Curves from the FBG Sensor on the Surface of S1TW

Results of S2T

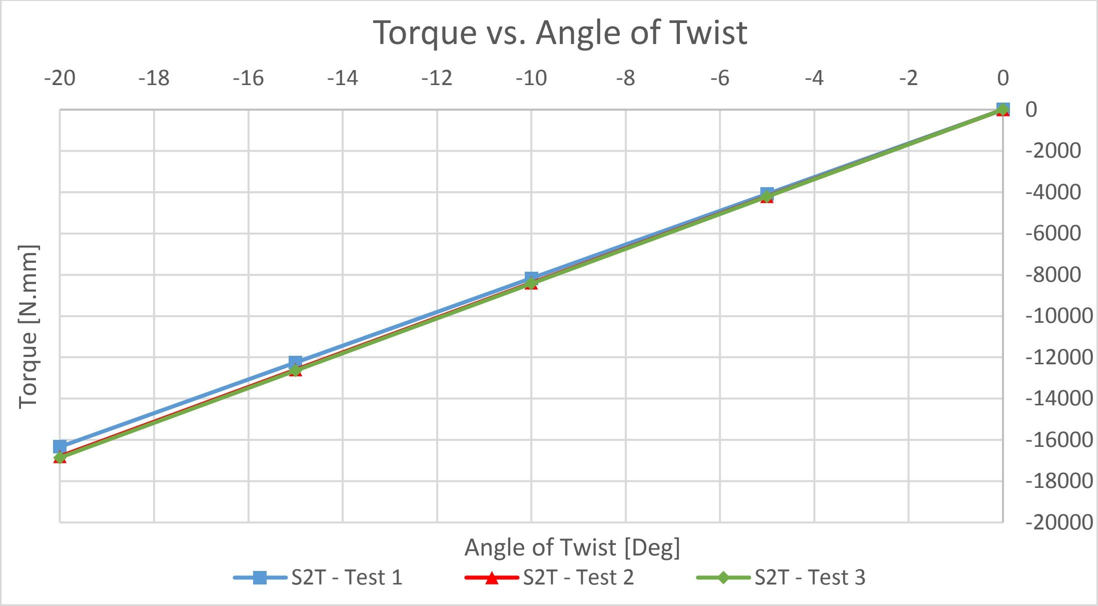

Figure 4.33: Torque - Angle of Twist Curves of S2T

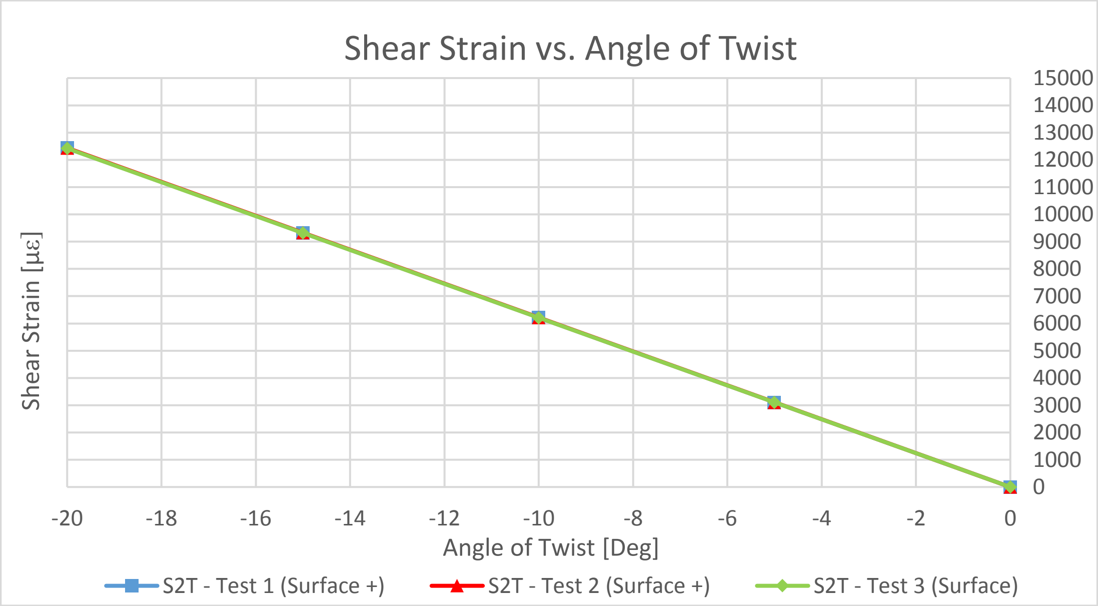

Figure 4.34: Shear Strain - Angle of Twist Curves from the FBG Sensor on the Surface of S2T

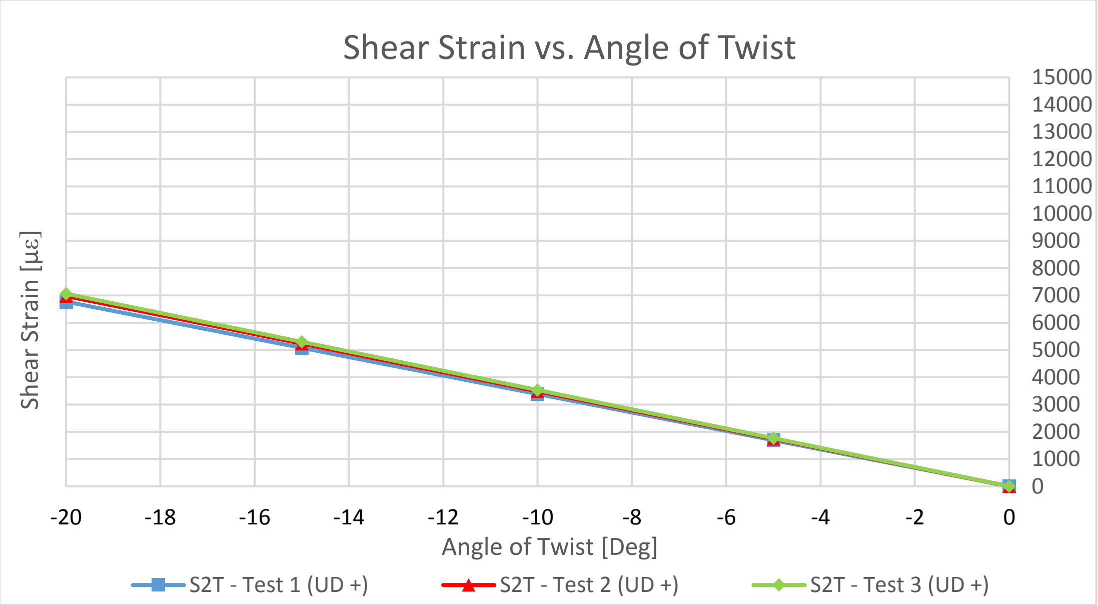

Figure 4.35: Shear Strain - Angle of Twist Curves from the FBG Sensor between the UD Layers of S2T

Results of S1TTW

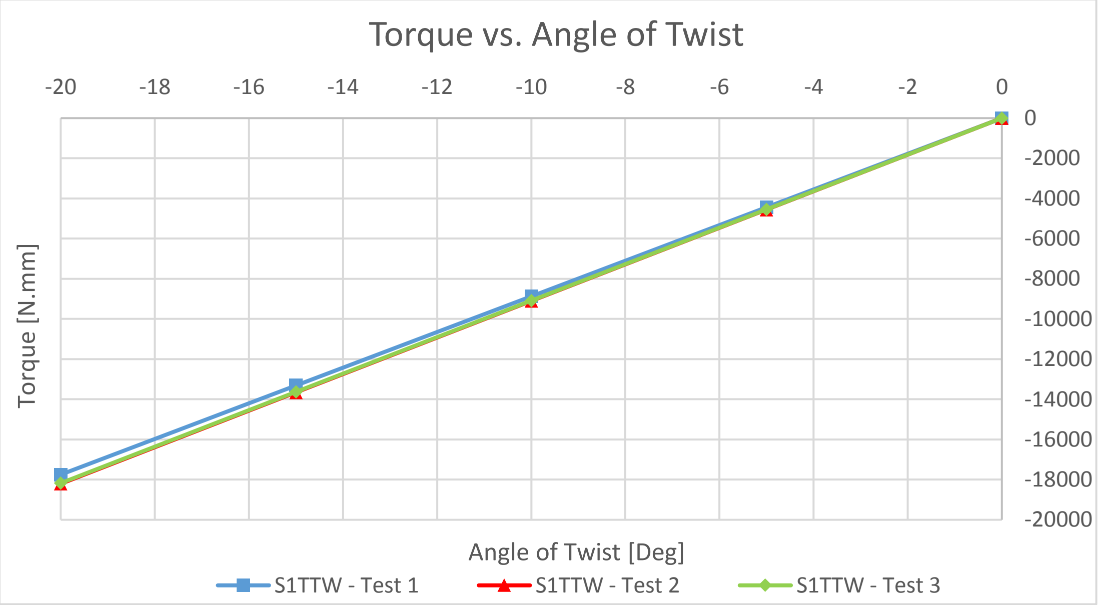

Figure 4.36: Torque - Angle of Twist Curves of S1TTW

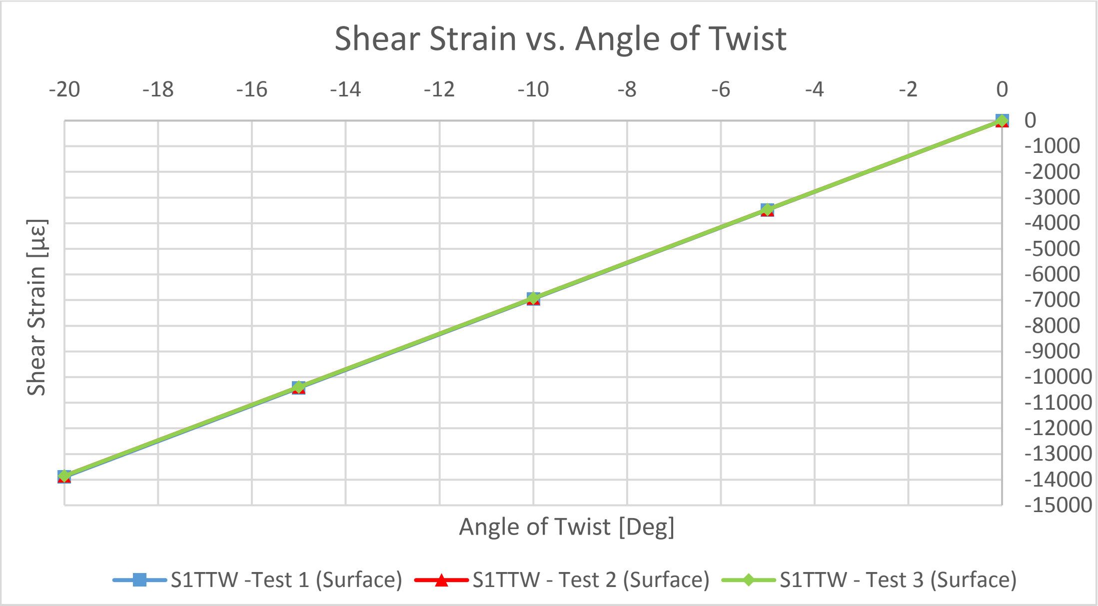

Figure 4.37: Shear Strain - Angle of Twist Curves from the FBG Sensor on the Surface of S1TTW

Results of S1TTUD

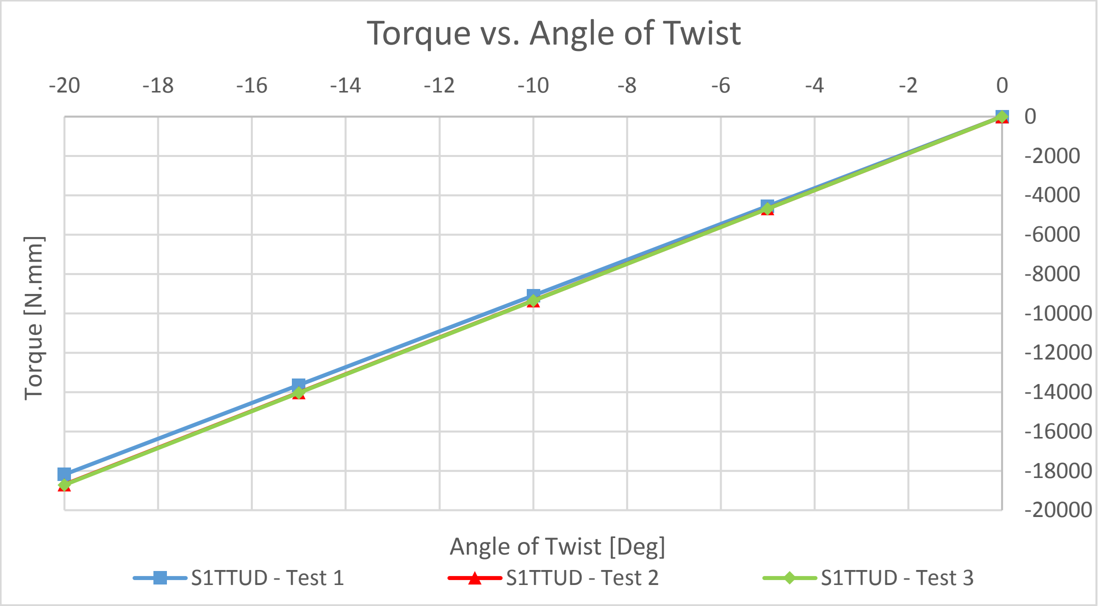

Figure 4.38: Torque - Angle of Twist Curves of S1TTUD

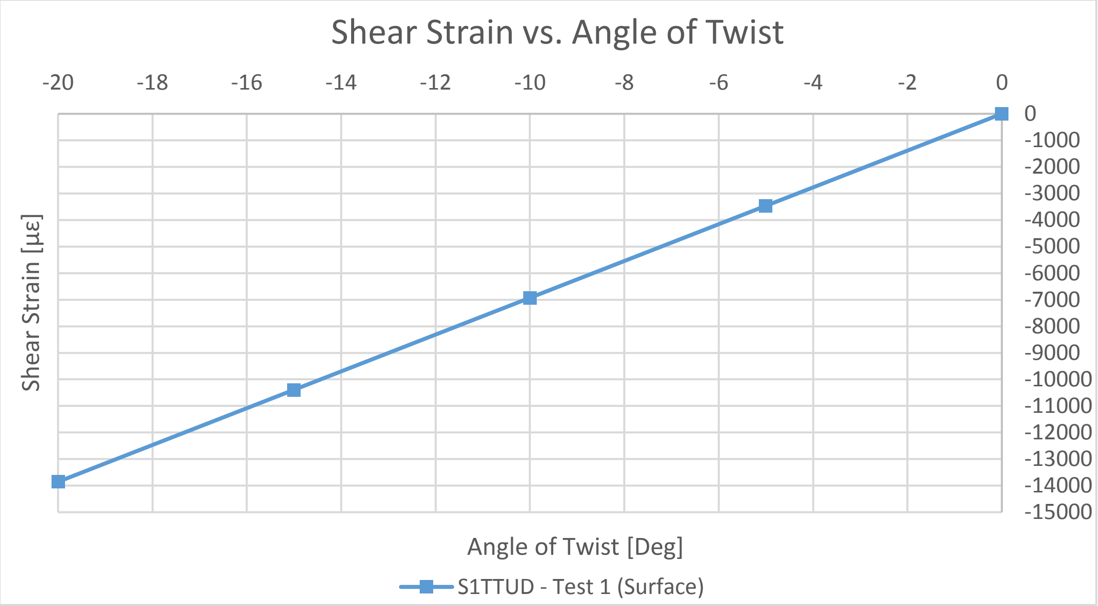

Figure 4.39: Shear Strain - Angle of Twist Curve from the FBG Sensor on the Surface of S1TTUD

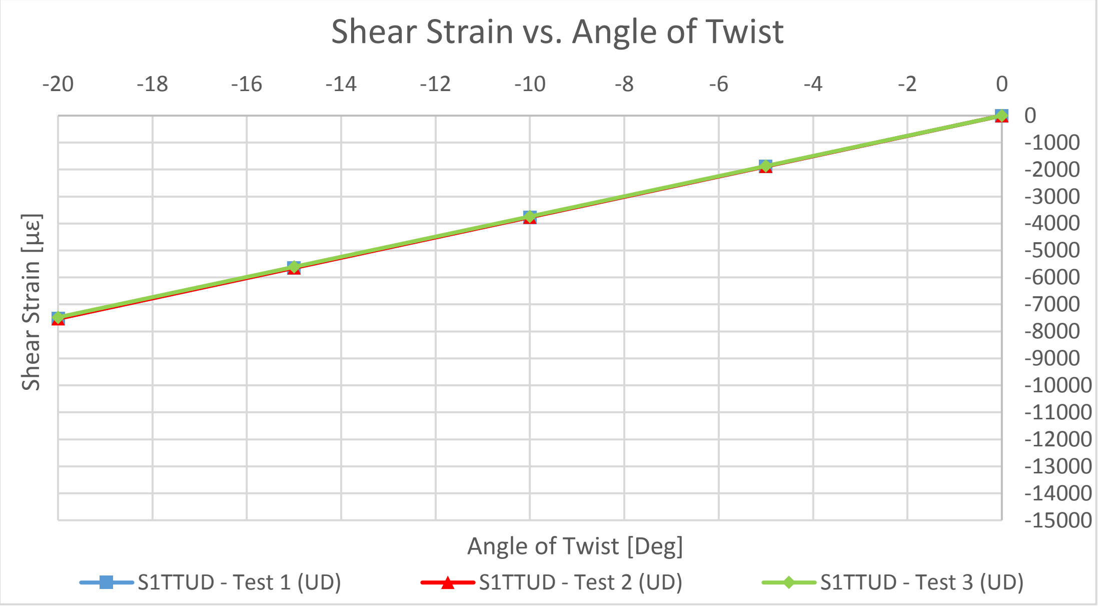

Figure 4.40: Shear Strain - Angle of Twist Curves from the FBG Sensor between the UD Layers of S1TTUD

Average Results Obtained from Three Tests for Each Beam

Average torque - angle of twist curves obtained from three tests for each beam are presented in Figure 4.41. As expected, the results of the beams without tabs (S1TW, S2T and S3T) are very close to each other. In addition, the results of the beams with tabs (S1TTUD and S1TTW) are nearly the same. Another observation is that the beams with tabs are stiffer than the beams without tabs, since the beams with tabs require larger torque for the same angle of twist.

Figure 4.42 and Figure 4.43 present average shear strains on the surface - angle of twist curves obtained from three tests of each beam. There are positive and negative shear strain data since position of some of the FBG sensors are in negative and some of them are in positive alignment with respect to the longitudinal axis. From Figure 4.42, it is observed that the shear strain results are nearly the same for the beams S2T and S3T, which have no tabs. However, from Figure 4.43, it is observed that there is an apparent difference between the shear strain measured at the surface of S1TW and the one measured from S3T, which means that the position or the angle of the FBG sensor on the surface of S1TW might be inaccurate. Also, adhesive thickness under the FBG sensor might affect the result. Another observation is that the shear strain measurements are larger for the beams with the tabs compared to the ones for the beams without the tabs.

Average torque - shear strain curves obtained from three tests of each beam are presented in Figure 4.44 and Figure 4.45, slope of which give torsional rigidity. From the figures, it is observed that the torsional rigidities of all the beams are nearly the same, except S1TW. As explained before, the difference might have been caused by the error in the measurement of the shear strain.

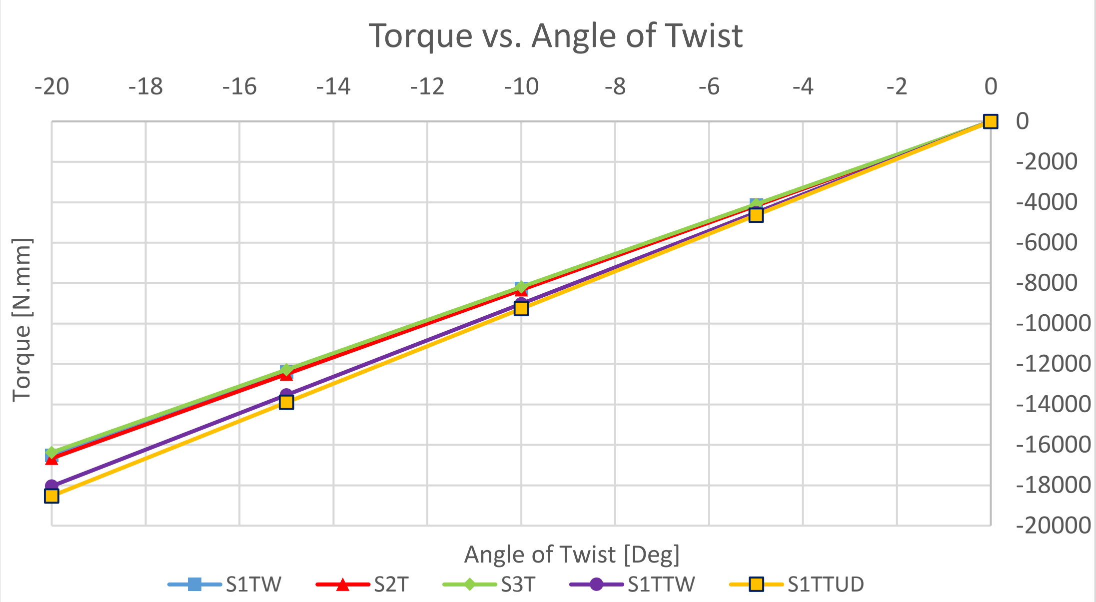

Figure 4.41: Average Torque - Angle of Twist Curves for Each Beam

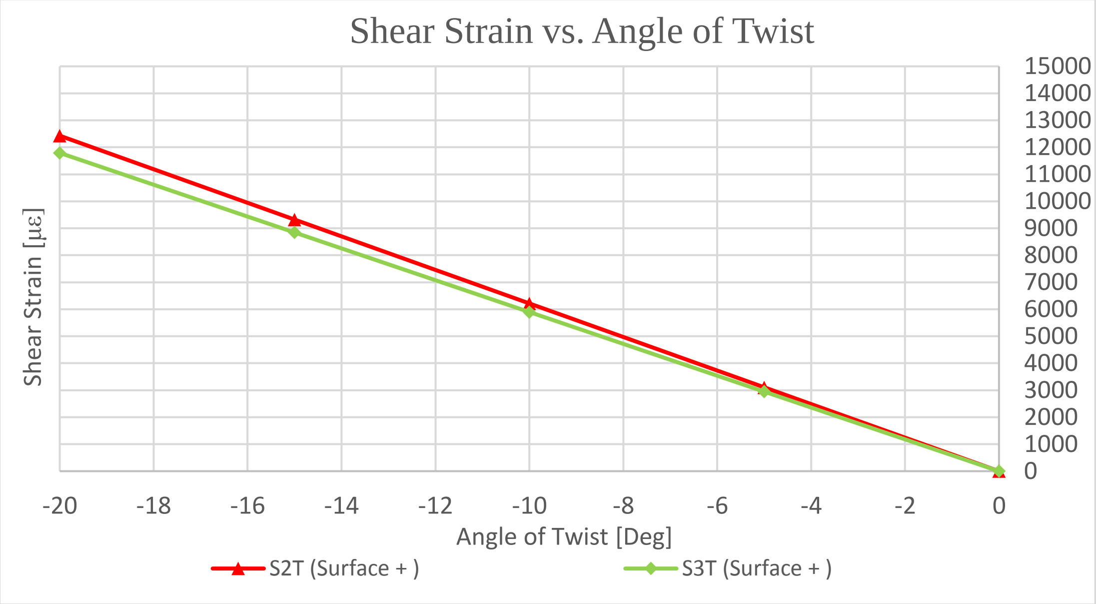

Figure 4.42: Average Positive Shear Strain - Angle of Twist Curves for Each Beam Obtained from the FBG Sensors at the Surface

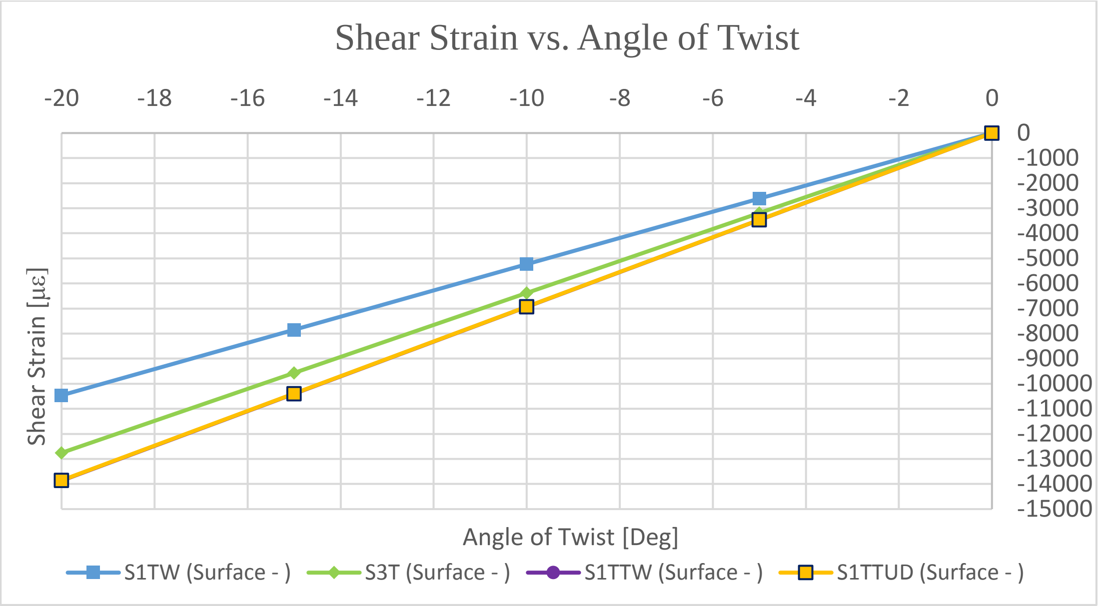

Figure 4.43: Average Negative Shear Strain - Angle of Twist Curves for Each Beam Obtained from the FBG Sensors at the Surface

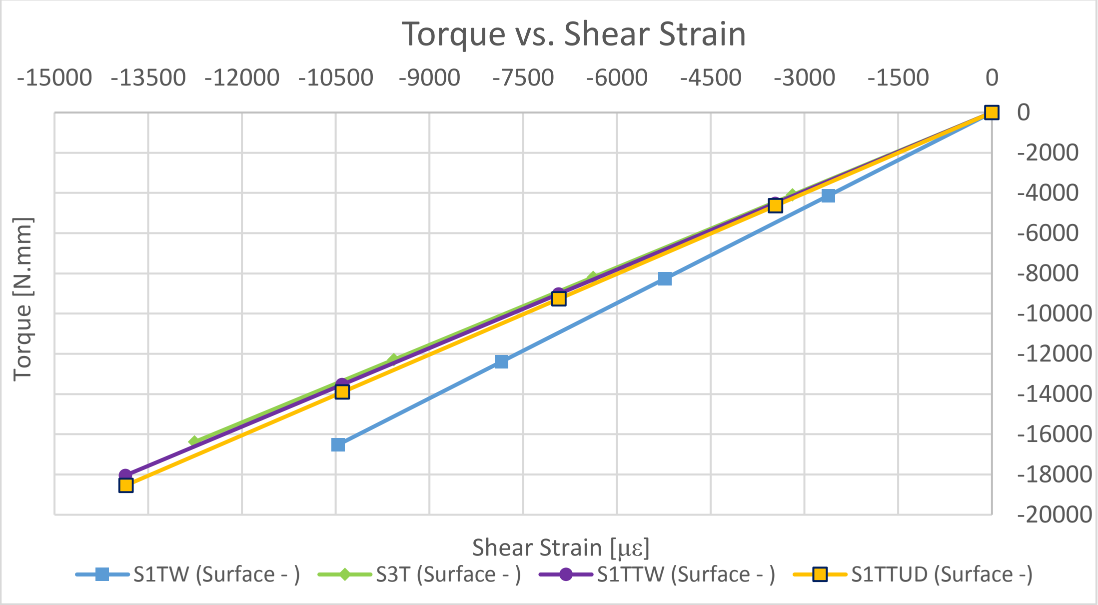

Figure 4.44: Average Torque – Negative Shear Strain Curves for Each Beam Obtained from the FBG Sensors at the Surface

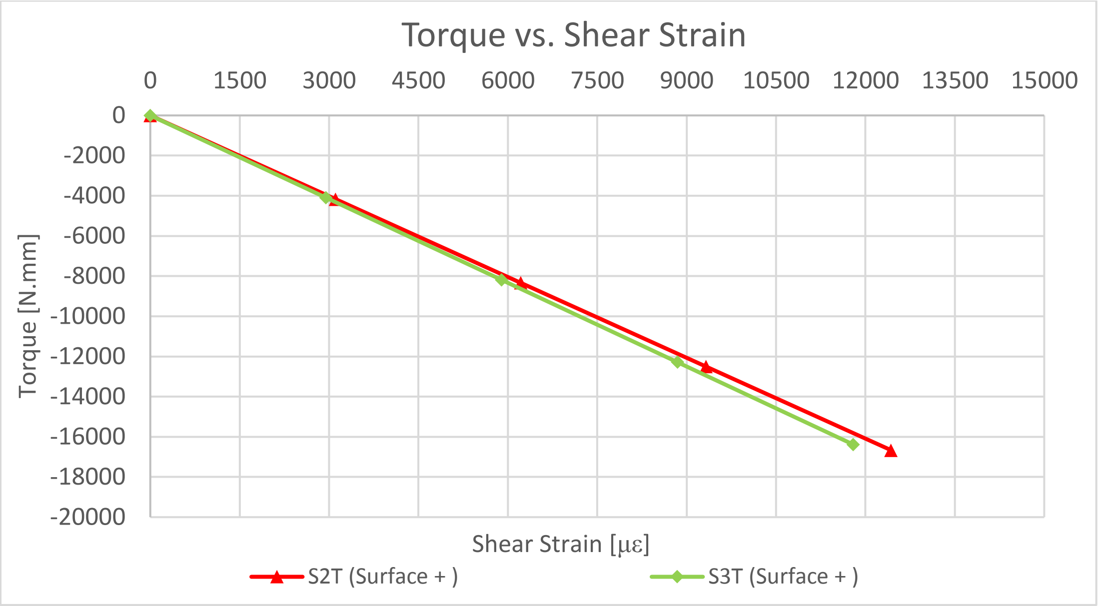

Figure 4.45: Average Torque – Positive Shear Strain Curves for Each Beam Obtained from the FBG Sensors at the Surface

Table 4.3 presents the overall average torque and shear strain results. First, the average of three tests for each specimen was obtained. Then, the beams were divided into two categories, namely the beams without tabs and the beams with tabs to calculate the average of them separately. Distorted data and unexpected results were not taken into account for the calculations. It is observed that the shear strain values increase with increasing distance from the middle plane of the beams. In addition, the shear strain values obtained from the FBG sensors between the woven layers are nearly zero, as expected. Very small strain readings could have been caused by the misalignments of the FBG sensors during embedding process and deterioration in symmetry during manufacturing. It is also noticed that the beams with tabs are stiffer than the beams without tabs, since the beams with tabs require larger torque.

Table 4.3: Average Torque and Shear Strain Results for Torsion Test

<table>
<tr><th colspan="6">Composite Beams without Tab</th></tr>
<tr><th>Angle [Deg]</th><th>Torque [N.mm]</th><th>Surface + [με]</th><th>Surface - [με]</th><th>UD [με]</th><th>Woven [με]</th></tr>
<tr><td>0</td><td>0.</td><td>0</td><td>0</td><td>0</td><td>0</td></tr>
<tr><td>-5</td><td>-4130.03</td><td>3027.66</td><td>-2902.29</td><td>1734.82</td><td>-50.03</td></tr>
<tr><td>-10</td><td>-8260.07</td><td>6055.31</td><td>-5804.58</td><td>3469.64</td><td>-134.86</td></tr>
<tr><td>-15</td><td>-12390.10</td><td>9082.97</td><td>-8706.87</td><td>5204.45</td><td>-254.49</td></tr>
<tr><td>-20</td><td>-16520.13</td><td>12110.63</td><td>-11609.16</td><td>6939.27</td><td>-408.92</td></tr>
<tr><th colspan="6">Composite Beams with Tab</th></tr>
<tr><th>Angle [Deg]</th><th>Torque [N.mm]</th><th>Surface + [με]</th><th>Surface - [με]</th><th>UD [με]</th><th>Woven [με]</th></tr>
<tr><td>0</td><td>0</td><td>-</td><td>0</td><td>0</td><td>0</td></tr>
<tr><td>-5</td><td>-4602.53</td><td>-</td><td>-3465.12</td><td>-1905.37</td><td>-23.56</td></tr>
<tr><td>-10</td><td>-9205.05</td><td>-</td><td>-6930.24</td><td>-3810.75</td><td>-50.48</td></tr>
<tr><td>-15</td><td>-13807.58</td><td>-</td><td>-10395.36</td><td>-5716.12</td><td>-80.76</td></tr>
<tr><td>-20</td><td>-18410.10</td><td>-</td><td>-13860.48</td><td>-7621.50</td><td>-114.41</td></tr>
</table>

4.9 A Case Study for the Comparison of Strain Gage and FBG Sensor

A separate test was conducted to compare the shear strain results from a FBG sensor and a strain gage bonded to the surfaces of a composite beam. FBG sensor was bonded on the surface in 45° configuration from the longitudinal direction. Two strain gages were bonded on other surface in ±45° configuration as shown in Figure 4.49. Shear strain – angle of twist curves and torque – shear strain curves obtained from the sensors are presented in Figure 4.50 and Figure 4.51, respectively. Considering the results presented in figures, shear strain value difference is around ±0.5%.

A previous study conducted by the members of the project, including the author, also proved the agreement of the results obtained from the strain gages and FBG sensors during bending tests [75].

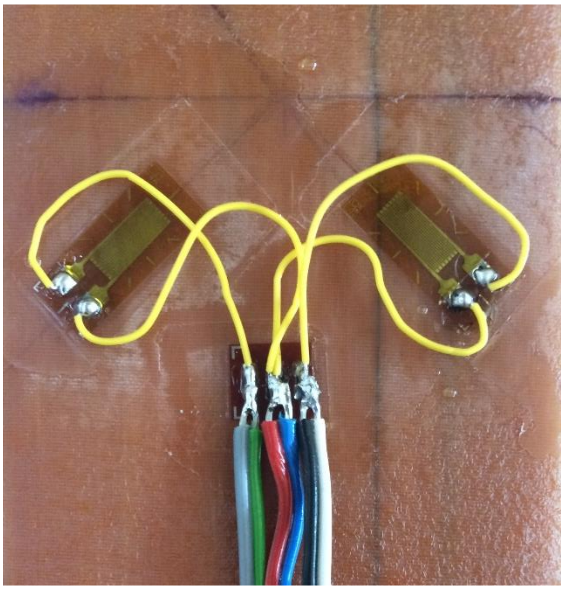

Figure 4.46: Strain Gages Bonded in ±45° Configuration

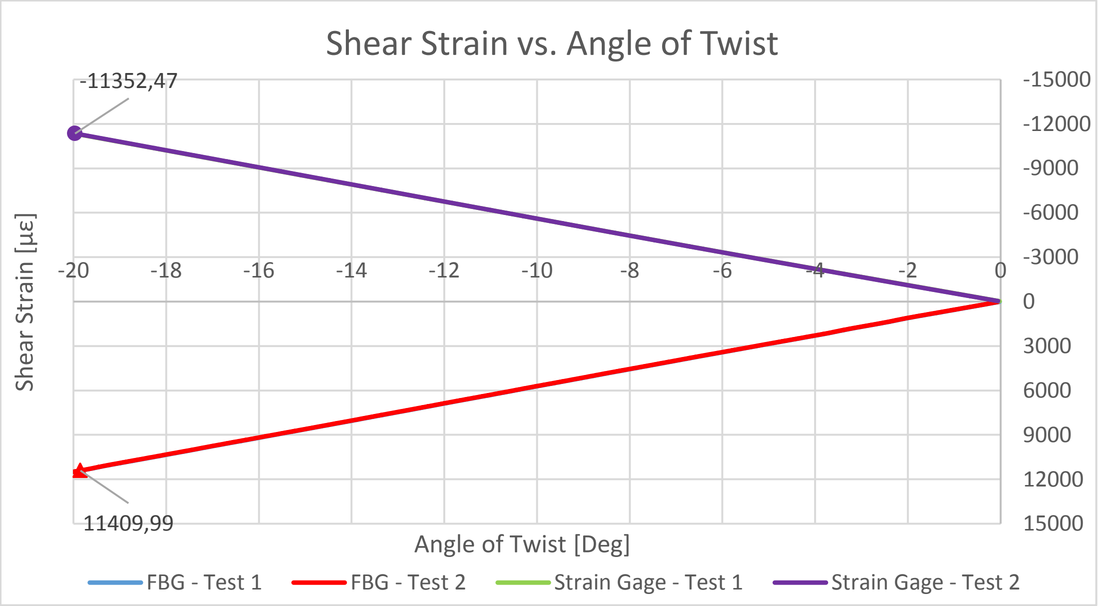

Figure 4.47: Shear Strain - Angle of Twist Curves Obtained from FBG and Strain Gage Sensors

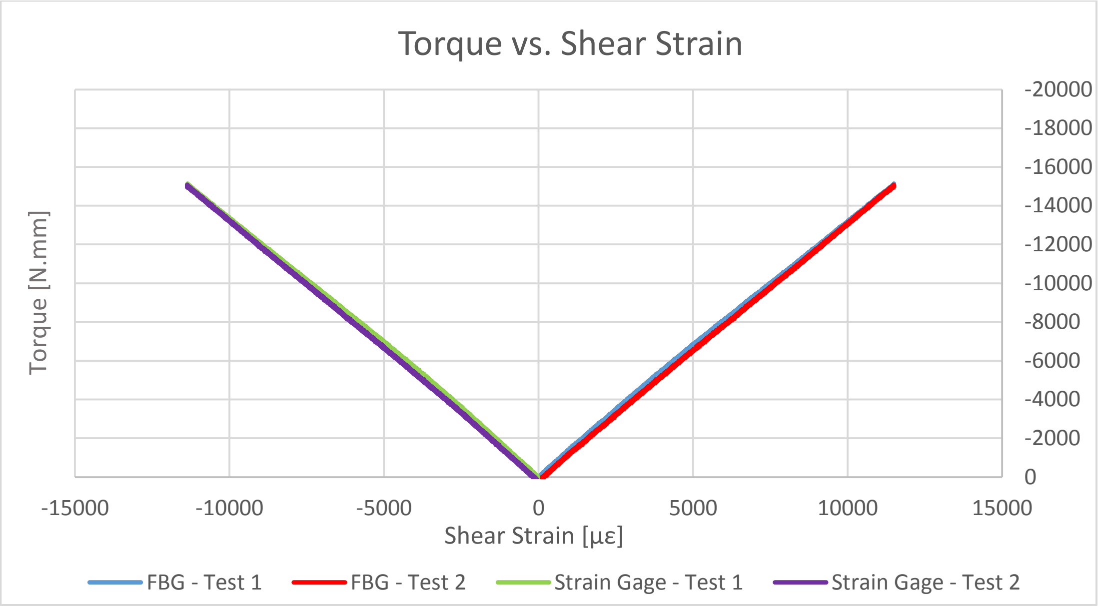

Figure 4.48: Torque - Shear Strain Curves Obtained from FBG and Strain Gage Sensors

4.10 Conclusion

Static tests of six composite beams instrumented with surface bonded and embedded FBG sensors were performed under torsional load. Some of the beams have tabs bonded at the ends of them. The signs in loading curves and cracking sounds which indicate damages were not observed.

All the tests were conducted three times for each specimen to prove the reproducibility. In addition, the similar trends in torque - angle of twist and shear strain - angle of twist curves for different beams also confirmed the reproducibility.

Test results demonstrated that both the torque and the shear strain change linearly with the angle of twist.

Shear strain values increased with increasing distance from the middle plane of the composite beams, which is expected. In addition, shear strain results of the FBG sensors embedded at the middle of the beam between the woven layers were nearly zero. Small variations from the zero might have been caused by misalignments of the FBG sensors and asymmetry caused by manufacturing errors.

Torsional rigidities of the composite beams are nearly the same except for one beam, namely S1TW. Misalignments of the FBG sensor and adhesive thickness might have been the reason behind that result.

Finally, a separate torsion test of a composite beam which had a FBG surface bonded on its surface and a strain gage bonded on its other surface is performed. Shear strain result difference was around ±0.5 %, which indicates good agreement of the results.

Overall average results of the torsion tests presented in Table 4.7 will be compared with the results of the FEA in Chapter 5.

CHAPTER 5

COMPARISON OF THE FINITE ELEMENT ANALYSES AND TEST RESULTS AND DISCUSSION

5.1 Introduction

In this chapter, torque and shear strain results obtained from the FEA and tests are compared. The reasons which might lead to the difference between the results are discussed. In addition, uncertainties caused by the manufacturing process and the tests are identified.

5.2 Comparison of the Results of Finite Element Analyses and Tests and Discussion

The results obtained from the tests and from the FEA are presented together in Figure 5.1 – Figure 5.12. Figure 5.1 – Figure 5.6 include the results for the beams without tabs and Figure 5.7 – Figure 5.12 include the results for the beams with tabs.

Test results are obtained by averaging the results of three tests of different beams (Figure 4.7). FEA results include the results of four different FEM. Finite Element Models differ from each other in terms of finite element types and geometric nonlinearity.

Test results are presented as solid lines whereas FEA results are presented as shapes for an easy comparison.

Results obtained from the tests and the FEA reveal great similarity especially until 10° of angle of twist. However, the difference between FEA and test results increases with increasing angle of twist for all of the four FEM.

Comparison of the test results and FEA results obtained from the four different FEM do not lead to a direct conclusion about which FEM is the most suitable one for the problem. Table 5.1 presents the percent differences between the test results and four different finite element models. It is observed that the difference between the tests and finite element models with C3D20R elements is greater than the one between the tests and finite element models with C3D8R elements, which shows that use of C3D8R elements is more convenient. Also, considering amount of the time needed to complete the FEA, one could prefer the finite element model with the C3D8R elements over the one with the C3D20R elements. In addition, the differences obtained from linear and nonlinear analyses do not lead to a direct conclusion about which analysis is convenient. However, geometric nonlinearity option should be included when great amount of angular distortion is expected. In addition, inclusion of material nonlinearity would lead to a more accurate solution of the torsion problem with great values of angle of twist.

It is observed that the torque results obtained from all the FEA are below the ones obtained from the tests. The main reason for the difference in torque measurements might have been an error in finite element modeling such as not including material nonlinearity in the FEA. Another observation is that some of the shear strain results obtained from the FEA are below the ones obtained from the tests. However, some of the shear strain results obtained from the FEA are above the ones obtained from the tests. In addition to not including the material nonlinearity, this outcome might have also been affected by the uncertainties surrounding manufacturing process and tests. An uncertainty analysis might be performed to reveal the effect on measurements. The list below includes the causes which might lead to the uncertainties.

- The alignment of the FBG sensors in ±45° from the longitudinal axis was conducted by hand with the help of a ruler and a miter.
- The position of the embedded FBG sensors might have been altered during the curing process of the beams.
- The position of the surface bonded FBG sensors depends on the adhesive thickness and bonding quality, which was performed by hand.
- The FBG sensors might not have been at the desired positions in thickness direction due to the effects distorting the symmetry during hand-layup.
- The beams were mounted on to the grips of the test machine by the sense of proportion which might have led to the symmetry and alignments errors.

Table 5.1: Percent Difference in Results of the Tests and Different Finite Element Models

	Angle [Deg]	**Torque [%]**	**Surface Strain + [%]**	**Surface Strain - [%]**	**UD + [%]**
Nonlinear C3D8R	0	-	-	-	-
	-5	5.88	-5.60	0.82	6.66
	-10	7.55	-7.29	1.37	4.15
	-15	10.33	-9.30	1.46	1.28
	-20	14.22	-11.60	1.13	-1.90
Linear C3D8Ra	0	-	-	-	-
	-5	5.25	-4.29	-0.16	8.72
	-10	5.25	-4.29	-0.16	8.72
	-15	5.25	-4.29	-0.16	8.72
	-20	5.27	-4.29	-0.16	8.72
Nonlinear C3D8R	0	-	-	-	-
	-5	6.90	5.70	12.75	6.86
	-10	8.61	3.93	13.18	4.35
	-15	11.38	1.77	13.15	1.46
	-20	15.31	-0.71	12.68	-1.73
Linear C3D8R	0	-	-	-	-
	-5	6.25	7.06	11.69	8.93
	-10	6.26	7.06	11.69	8.93
	-15	6.21	7.06	11.69	8.93
	-20	6.23	7.06	11.69	8.93

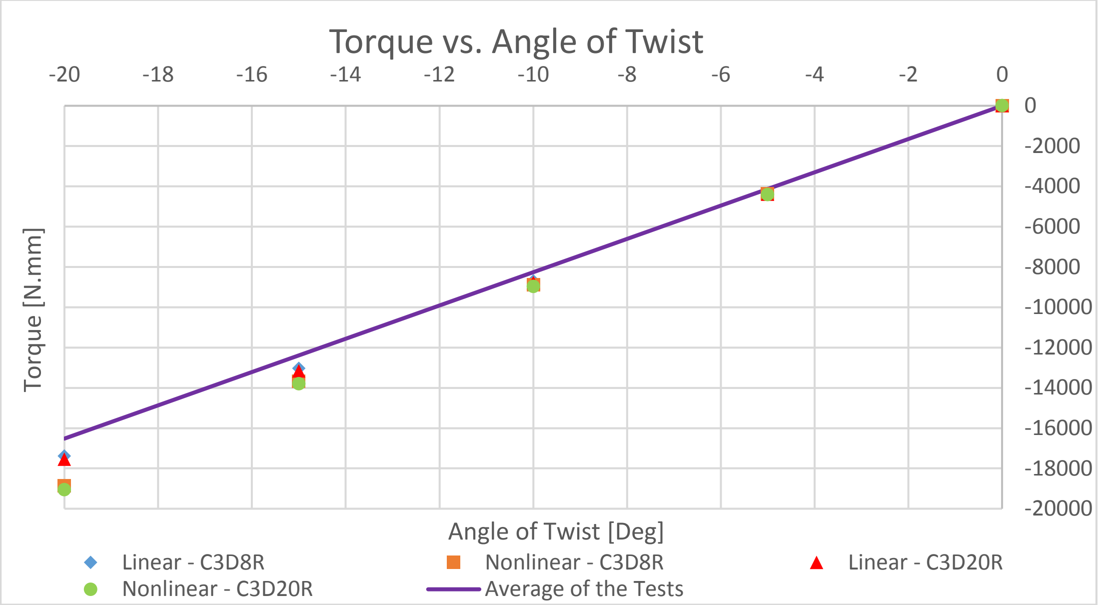

Figure 5.1: Torque - Angle of Twist Curves Obtained from the Tests and FEA for the Beams without Tabs

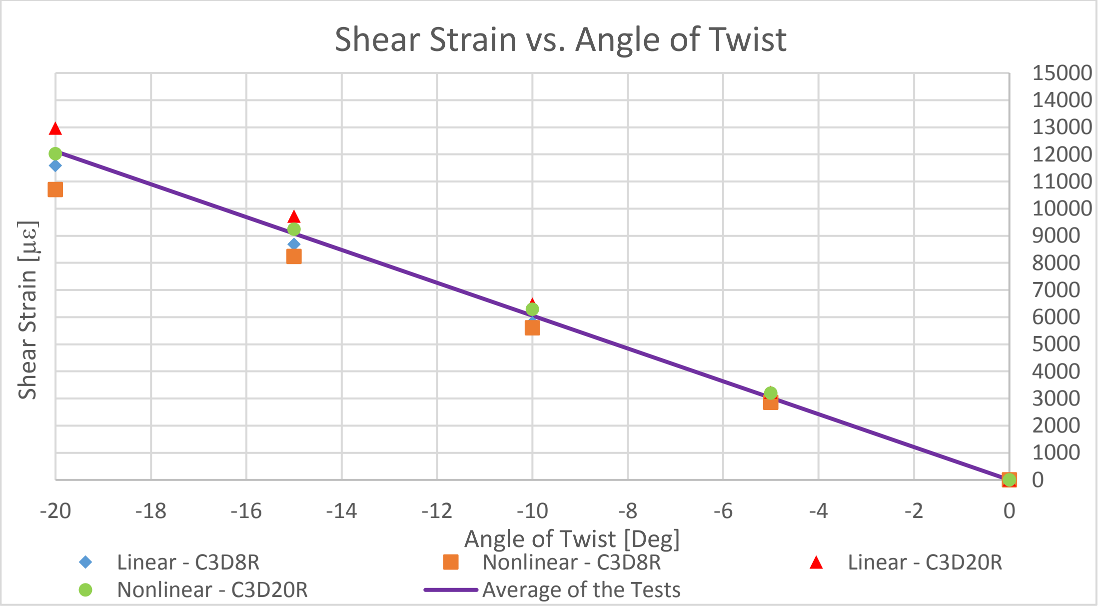

Figure 5.2: Positive Shear Strain on the Surface - Angle of Twist Curves Obtained from the Tests and FEA for the Beams without Tabs

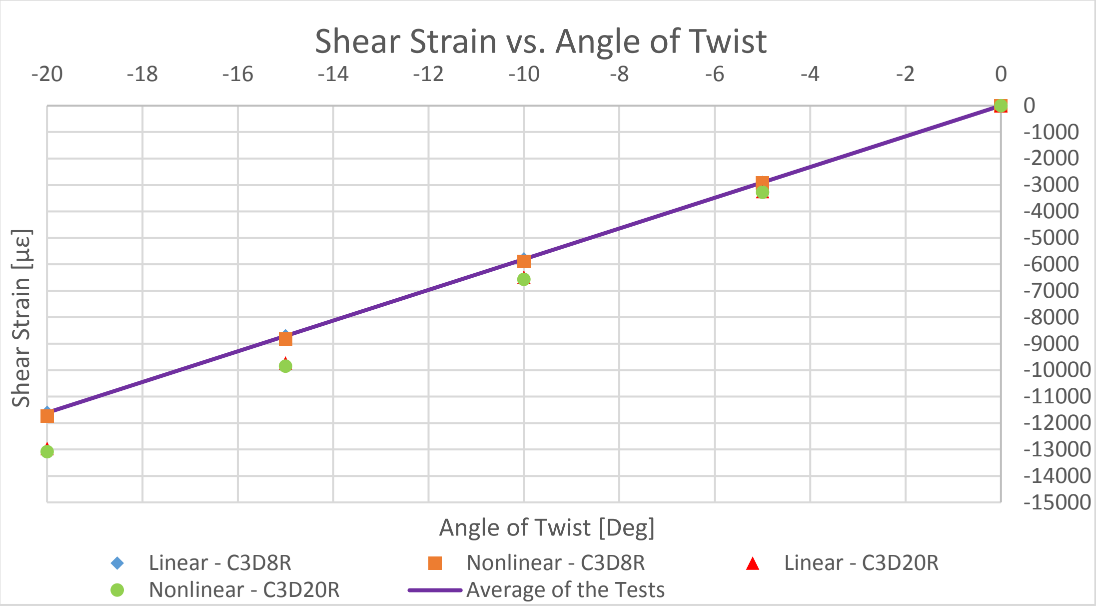

Figure 5.3: Negative Shear Strain on the Surface - Angle of Twist Curves Obtained from the Tests and FEA for the Beams without Tabs

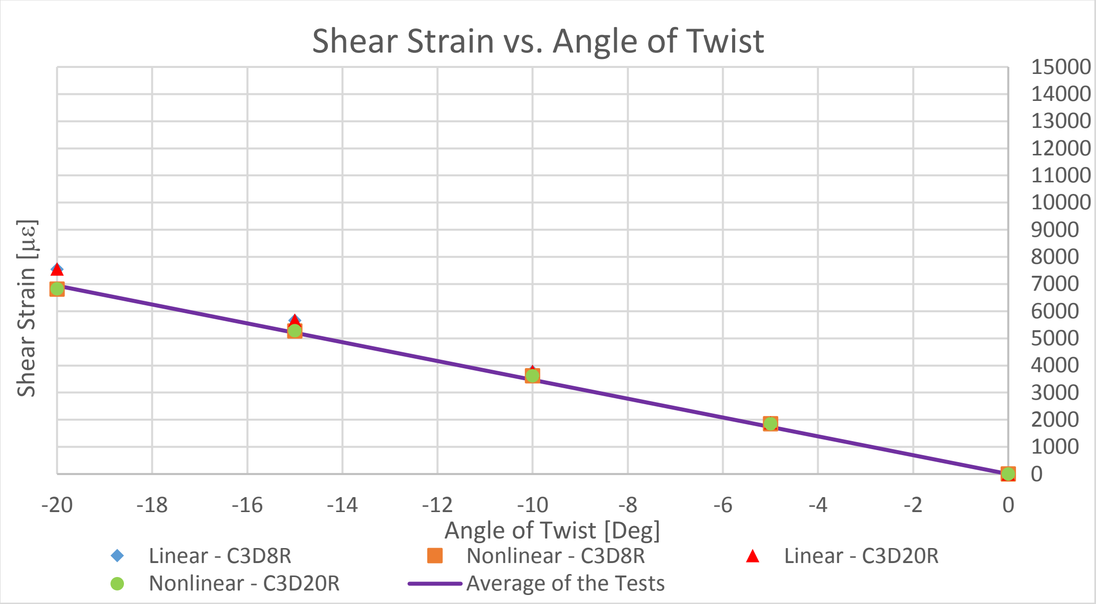

Figure 5.4: Positive Shear Strain between UD Layers - Angle of Twist Curves Obtained from the Tests and FEA for the Beams without Tabs

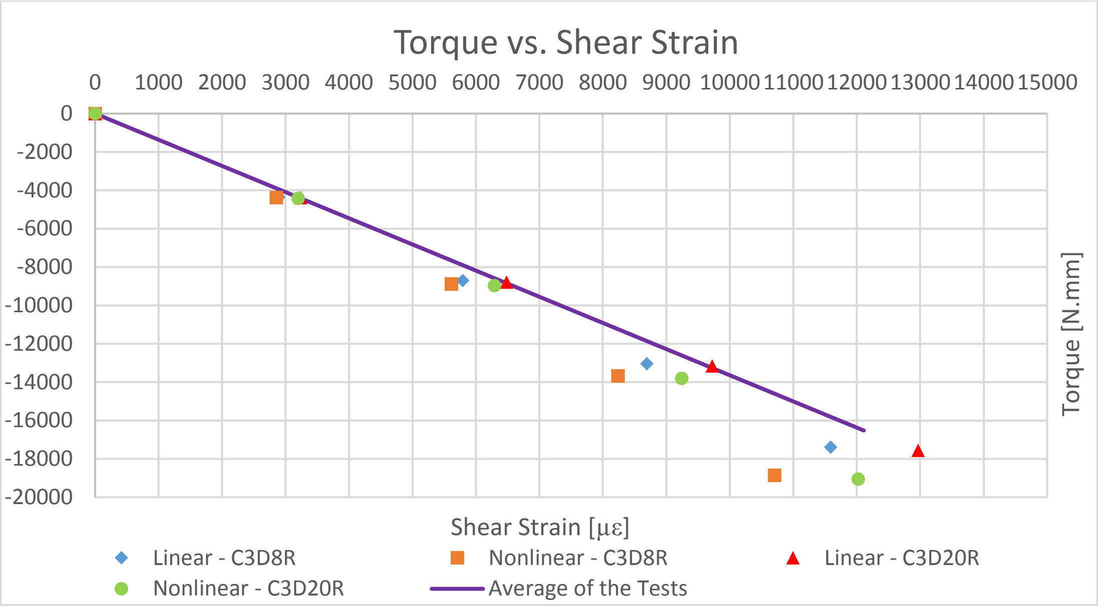

Figure 5.5: Torque - Positive Shear Strain on the Surface Curves Obtained from the Tests and FEA for the Beams without Tabs

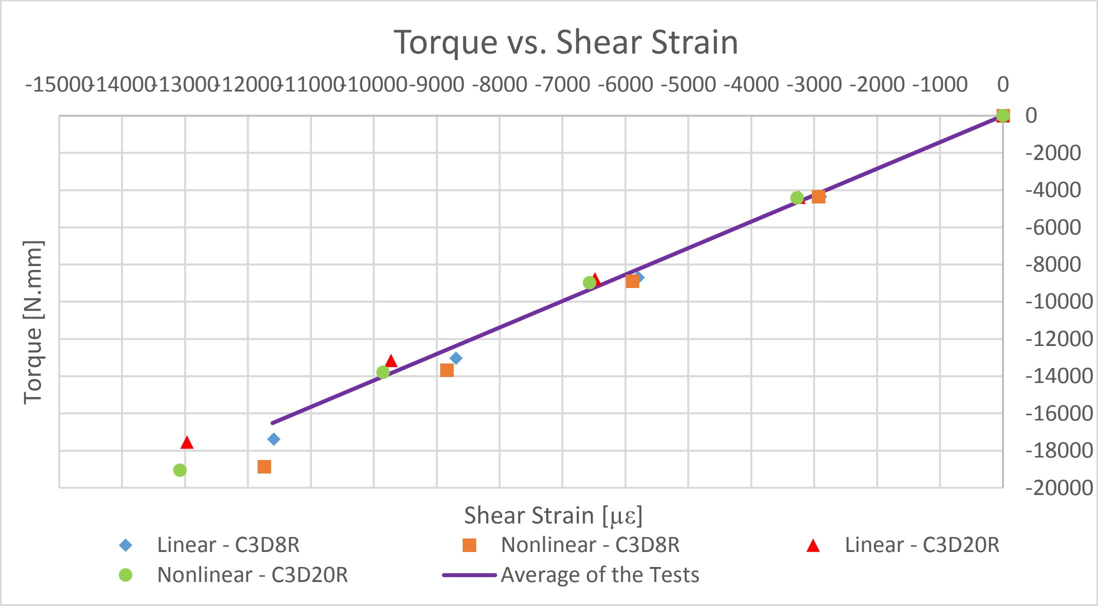

Figure 5.6: Torque - Negative Shear Strain on the Surface Curves Obtained from the Tests and FEA for the Beams without Tabs

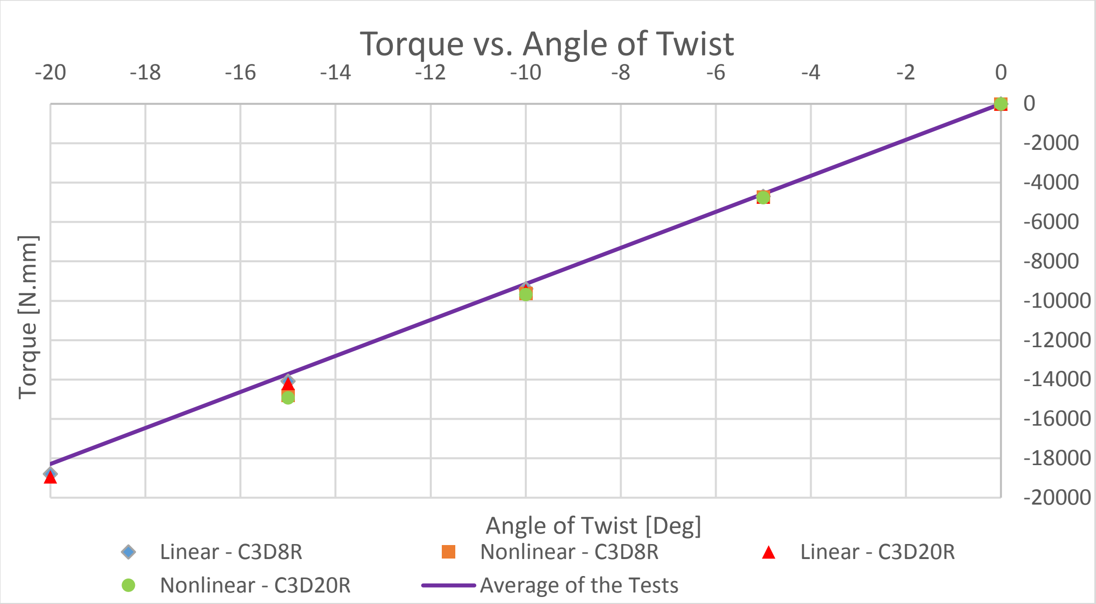

Figure 5.7: Torque - Angle of Twist Curves Obtained from the Tests and FEA for the Beams with Tabs

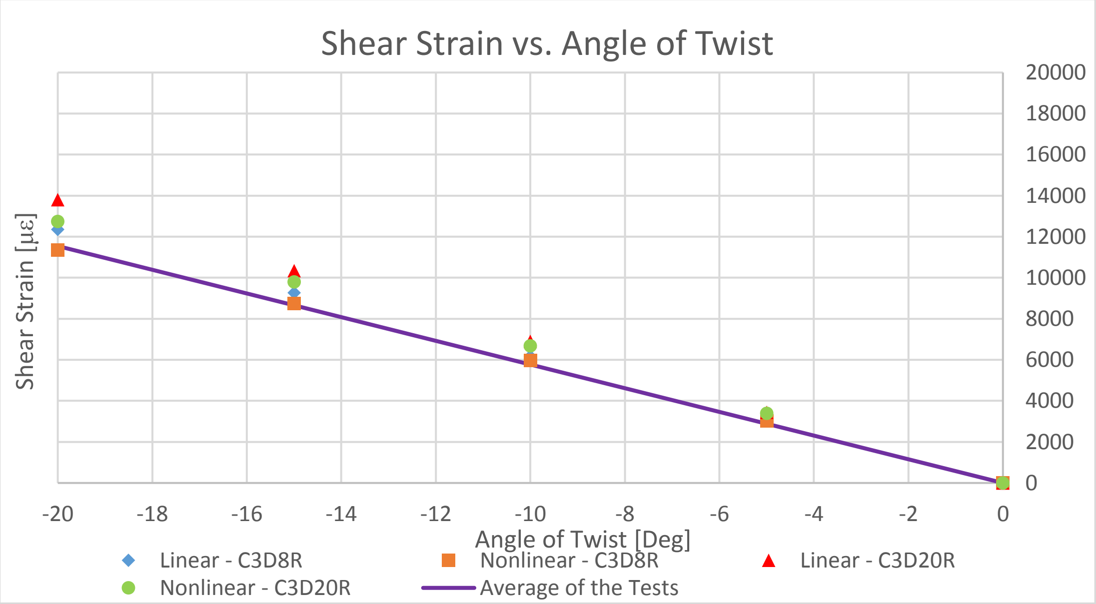

Figure 5.8: Positive Shear Strain on the Surface - Angle of Twist Curves Obtained from the Tests and FEA for the Beams with Tabs

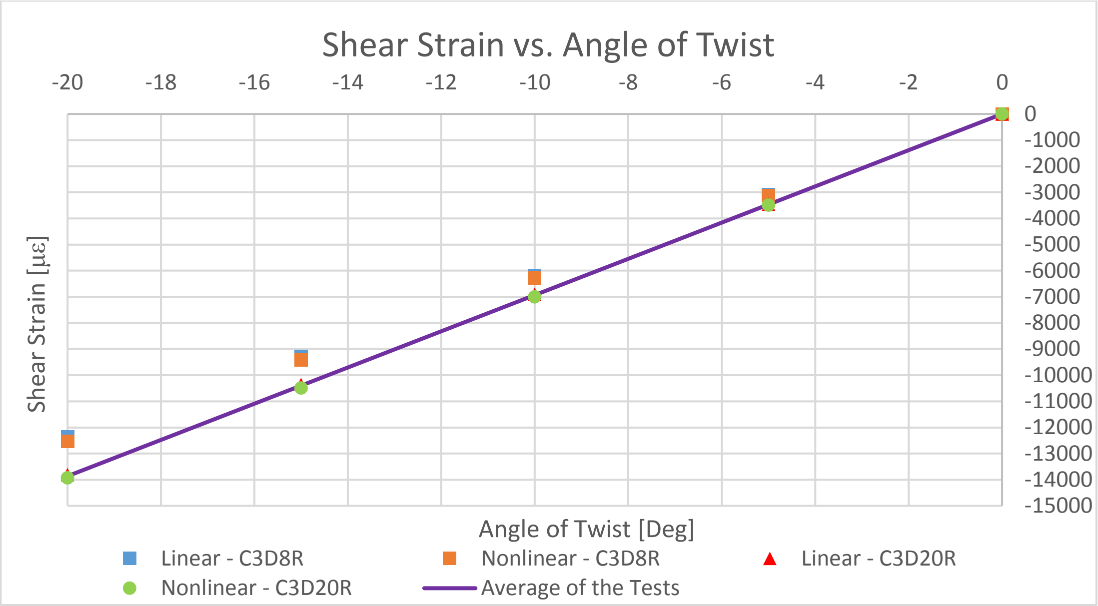

Figure 5.9: Negative Shear Strain on the Surface - Angle of Twist Curves Obtained from the Tests and FEA for the Beams with Tabs

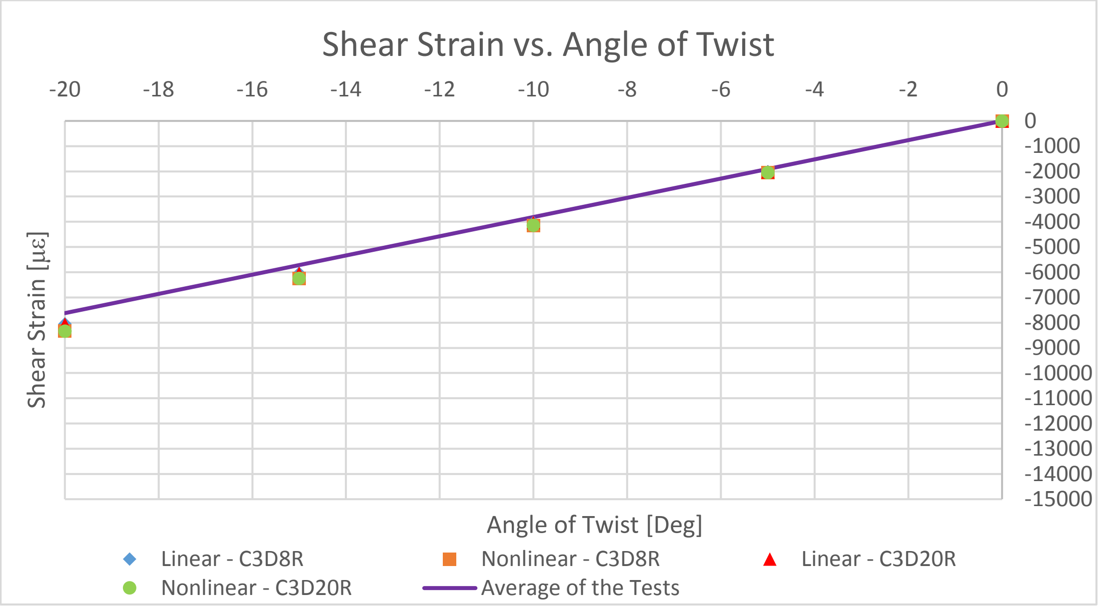

Figure 5.10: Negative Shear Strain between UD Layers - Angle of Twist Curves Obtained from the Tests and FEA for the Beams with Tabs

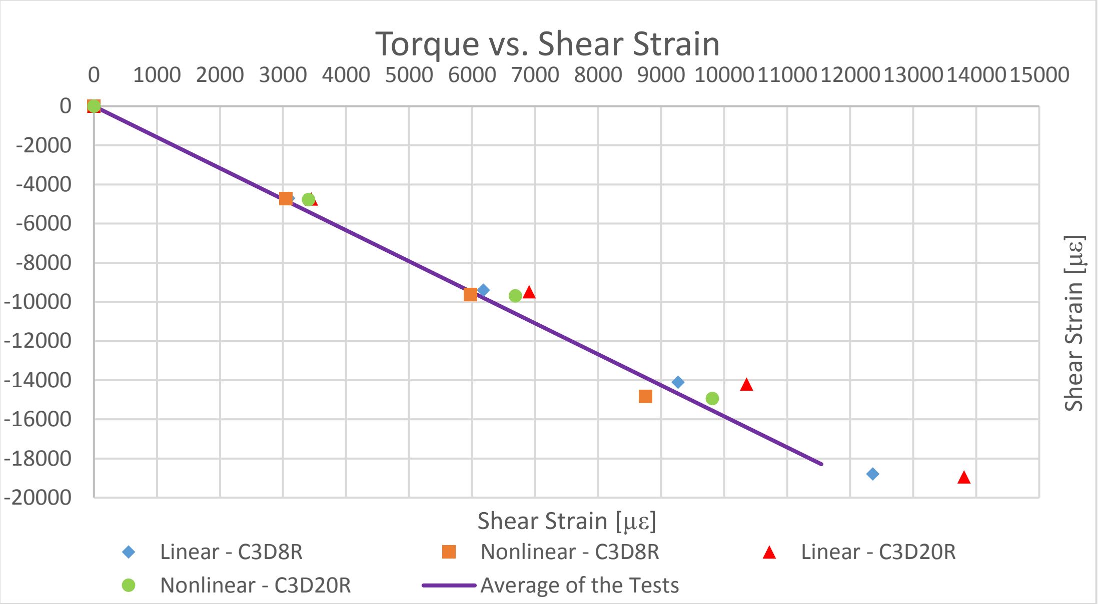

Figure 5.11: Torque - Positive Shear Strain on the Surface Curves Obtained from the Tests and FEA for the Beams with Tabs

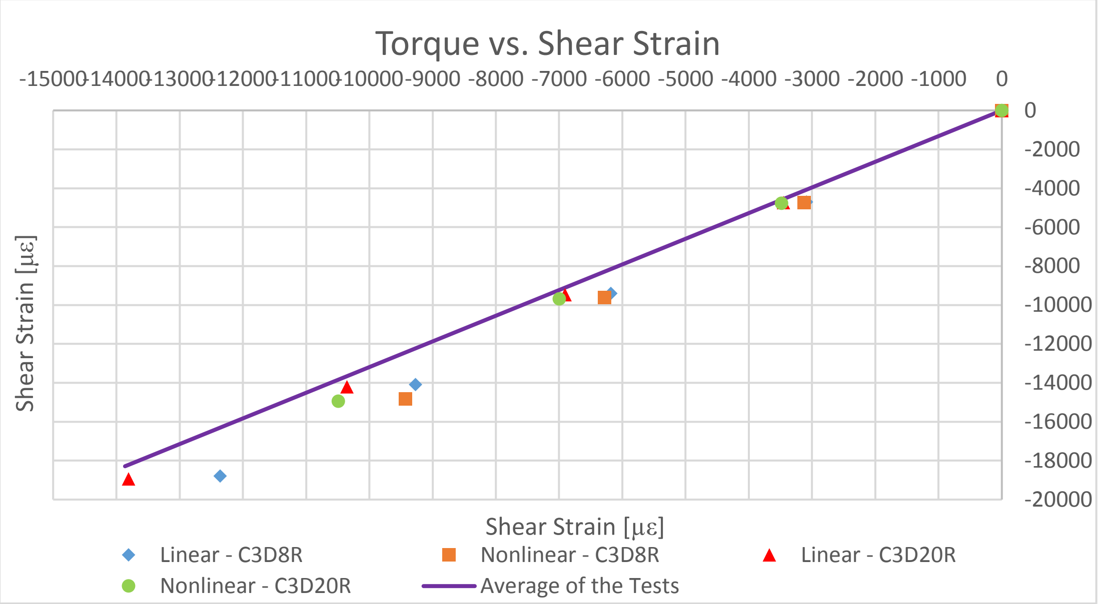

Figure 5.12: Torque - Negative Shear Strain on the Surface Curves Obtained from the Tests and FEA for the Beams with Tabs

Negative shear strain results on the surface are obtained at the locations 40° and 50° from the longitudinal axis to study the effect of misalignment in the angle of the FBG sensors. In addition, negative shear strain results on the surface are obtained at the locations -3 mm and +3 mm from the middle in longitudinal direction to study the effect of misalignment in the longitudinal position of the FBG sensors. The results are obtained from the FEA of the beams without tabs with C3D8R finite elements including geometric nonlinearity. Table 5.2 presents the error percentages in shear strains on the surface of the beams due to misalignments in angular position and in longitudinal position. It is observed that the maximum error percentage in shear strain results obtained from the misalignment in angle is -3.00% at 20° of angle of twist and the one obtained from the misalignment in longitudinal position is -0.20% at 20° of angle of twist. Considering the results, it could be said that the misalignment in angular position effects the shear strain results more than the misalignment in longitudinal position.

Table 5.2: Error Percentage of Negative Shear Strains on the Surface and between the UD Layers due to Misalignment Configurations

		Misalignment in Angular Position		**Misalignment in Longitudinal Position**	
On the Surface	Angle of Twist [Deg]	-5 Deg [%]	+5 Deg [%]	-3 mm [%]	+3 mm [%]
	0	0	0	0	0
	-5	-1.23	-1.78	-0.07	-0.07
	-10	-0.95	-2.01	-0.07	-0.07
	-15	-0.68	-2.24	-0.07	-0.07
	-20	-0.41	-2.5	-0.20	-0.09
		Misalignment in Angular Position		**Misalignment in Longitudinal Position**	
Between the UD Layers	Angle of Twist [Deg]	-5 Deg [%]	+5 Deg [%]	-3 mm [%]	+3 mm [%]
	0	0	0	0	0
	-5	-1.15	-1.88	-0.10	-0.10
	-10	-0.67	-2.27	-0.10	-0.10
	-15	-0.27	-2.64	-0.14	-0.10
	-20	-0.15	3.00	-0.20	-0.15

5.3 Conclusion

In this section, the results acquired from the FEA and tests are compared. FEA results include the analysis results from four FEM with different types of finite element and with different geometric nonlinearity configuration.

The difference between the FEA results and tests is below ±10% for 10° of angle of twist. However, the difference increases with increasing angle of twist. The reason behind the difference might be not including the material nonlinearity and misalignment errors during manufacturing and tests.

It is not possible to reach a direct conclusion about the most suitable FEM for the torsion problem. However, the percent differences between the tests and FEA results are lower for the finite element model with C3D8R elements. In addition, computational time is much less if finite element model with C3D8R elements are used.

As a conclusion, it could be said that the results of all the FEM are in good comparison with the results of the tests for 10° of angle of twist. However, material nonlinearity should be included to obtain more accurate results for torsion problems with angle of twist values greater than 10°.

CHAPTER 6

CONCLUSION

6.1 General Conclusions

In this thesis, feasibility of FBG sensors for the SHM of composite structures is investigated by testing composite beams with embedded and surface bonded FBG sensors under static torsional load.

Valuable experiences for the manufacturing of composite structures with embedded FBG sensors are gained. Composite laminates are put under vacuum after placement of FBG sensors to the desired positions for avoiding any misalignment. Also, Teflon tubes are used to protect the FBG sensors from the stress concentrations at the ingress/egress regions.

FEA of the composite laminates under torsional load is conducted using the commercial FEA code ABAQUS®. FEM is constructed as close as possible to the test conditions. Geometric nonlinearity is included since large amounts of angular distortions is expected for a 20° of angle of twist.

Most importantly, static torsion tests of the composite laminates with embedded and surface bonded FBG sensors are performed. Useful experience is gathered for handling and ensuring the health of the sensors during tests. In addition, it is observed that torque and shear strain values change linearly with angle of twist for glass/epoxy composite laminates.

Consistent results obtained from the FEA and the tests reveal that FBG sensors could be considered as feasible and capable sensors for the SHM of composite structures. The differences between the torque and shear strain results acquired from the FEA and tests are in the range of 10% for a 10° of angle of twist. The difference increases with increasing angle of twist, possibly due to not including the material nonlinearity for larger angle of twist values. Also, it is found that type of finite element does not greatly affect the results.

Finally, a case study including comparison of the results obtained from the FBG sensor and conventional strain gage reveals the feasibility of the FBG sensors for strain measuring. The difference between the measurements is in the range of ±0.5%.

6.2 Recommendations for Future Work

There are many recommendations that would improve this study. First of all, it would be superior to be able to track the positions of the FBG sensors. Metallic paint could be applied on the fiber optic cable before embedding process such that it becomes possible to track the positions of the FBG sensors using ultrasonic scans. Hence, the alignment of the FBG sensors is achieved. Also, the effect of the errors on the shear strain results due to misalignments could be quantified by performing tests using deliberately misaligned sensors. In addition, it is recommended that FEM is constructed as close as possible to the test conditions. Including both material and geometric nonlinearity during construction of FEM would produce more accurate results at great amounts of angle of twists. Finally, performing the tests in a more controlled environment and keeping the settings of the test system the same for the test of each specimen would improve the accuracy of the test results.

Future studies might include utilizing embedded FBG sensors to detect damage. Comparison of the strain measurements of healthy and damaged composite structures with surface bonded and embedded FBG sensors would further confirm the feasibility and ability of the FBG sensors for damage detection, and in turn for SHM applications. In addition, finite element model generated for the study might be used for optimizing damage and FBG sensor locations before the tests. Another future study might include comparison of the ability of damage detection of FBG sensors with the one of different embeddable sensors such as piezoelectric sensors. Finally, fatigue tests of composite laminates with embedded of surface bonded FBG sensors could be performed to reveal the durability of the FBG sensors.

REFERENCES

[1] G. Kister *et al.*, “Monitoring of an all-composite bridge using Bragg grating sensors,” *Constr. Build. Mater.*, vol. 21, no. 7, pp. 1599–1604, 2007.

[2] R. C. Tennyson, A. A. Mufti, S. Rizkalla, G. Tadros, and B. Benmokrane, “Structural health monitoring of innovative bridges in Canada with fiber optic sensors,” *Smart Mater. Struct,* vol. 10, no. 1, pp. 560–573, 2001.

[3] D. S. Li, L. Ren, H. N. Li, and G. B. Song, “Structural health monitoring of a tall building during construction with fiber bragg grating sensors,” *Int. J. Distrib. Sens. Networks*, vol. 2012, 2012.

[4] J. Joshi *et al.*, “Structural health monitoring of Earth Air Tunnel (EAT) using wireless sensor network,” *EESMS 2016 - 2016 IEEE Work. Environ. Energy, Struct. Monit. Syst. Proc.*, 2016.

[5] X. Y. Xie and L. Feng, “Real-Time Health Monitoring System for Power Tunnel,” *GeoCongress 2012 © ASCE 2012,* 3099, pp. 3099–3108, 2012.

[6] A. Sanchez Ramirez, R. Loendersloot, and T. Tinga, “Helicopter rotor blade monitoring using autonomous wireless sensor network,” *10th Int. Conf. Cond. Monit. Mach. Fail. Prev. Technol.,* 2013.

[7] B. R. Zwink, E. M. Prewett, D. E. Adams, and D. J. Koester, “Load Estimation and Damage Detection in Helicopter Rotor Blades Section I : Introduction Section II : Experimental Setup,” *IMAC-XXVI: Conference & Exposition on Structural Dynamics,* 2008.

[8] P. M. Pawar, “Structural Health Monitoring of Composite Helicopter Rotor Blades,” Indian Institute of Science, 2006.

[9] A. V. Srinivasan, D. G. Cuttsi H. . Shu, D. L. Sharpe, and O. A. Bauchau, “Structural Dynamics of a Helicopter Rotor Blade System,” *Journal of the American Helicopter Society*, vol. 35, pp. 75–85, 1990.

[10] J. R. Pedrazzani, S. M. Klute, D. K. Gifford, A. K. Sang, and M. E. Froggatt, “Embedded and surface mounted fiber optic sensors detect manufacturing defects and accumulated damage as a wind turbine blade is cycled to failure,” *Luna Innov. Inc,* 2012.

[11] S. W. Kim, W. R. Kang, M. S. Jeong, I. Lee, and I. B. Kwon, “Deflection

estimation of a wind turbine blade using FBG sensors embedded in the blade bonding line," *Smart Mater. Struct*, vol. 22, no. September 2016, 2013.

[12] S. Takeda, Y. Aoki, T. Ishikawa, N. Takeda, and H. Kikukawa, "Structural health monitoring of composite wing structure during durability test," *Composite Structures*, vol. 79, pp. 133–139, 2007.

[13] J. Costa *et al.*, "Fiber-optically sensorized composite wing," *Proc. of SPIE,* vol. 9062, pp. 1–6, 2017.

[14] C. Ryu, J. Lee, C. Kim, and C. Hong, "Buckling behavior monitoring of a composite wing box using multiplexed and multi-channeled built-in fiber Bragg grating strain sensors," *NDT&E Internationa*, vol. 41, pp. 534–543, 2008.

[15] J. Lee, C. Ryu, B. Koo, S. Kang, C. Hong, and C. Kim, "In-flight health monitoring of a subscale wing using a fiber Bragg grating sensor system," *Smart Mater. Struct.*, vol. 12, no. June 2017, pp. 147–155, 2003.

[16] P. Pawar and R. Ganguli, "Helicopter rotor health monitoring- a review," *Proc. Inst. Mech. Eng. Part G J. Aerosp. Eng.*, vol. 221, pp. 631–647, 2007.

[17] M. Saxena, O. O. Bannett, and V. Sharma, "Bearing Fault Evaluation for Structural Health Monitoring, Fault Detection, Failure Prevention and Prognosis," *Procedia Eng.*, vol. 144, pp. 208–214, 2016.

[18] A. Güemes and A. Fernandez-lopez, "Damage Detection in Bolted Joints by Fibre Optics Distributed Sensing," 2nd International Symposium on NDT in Aerospace 2010 - Mo.2.A.2, 2010.

[19] K. Worden and J. M. Dulieu-Barton, "An Overview of Intelligent Fault Detection in Systems and Structures," *Structural Health Monitoring*, vol. 3, no. 1, pp. 85–98, 2004.

[20] C. Boller, F. Chang, and Y. Fujino, *Encyclopedia of Structural Health Monitoring*. 2009.

[21] R. Rolfes, S. Zerbst, G. Haake, J. Reetz, and J. P. Lynch, "Integral SHM-System for Offshore Wind Turbines Using Smart Wireless Sensors," *6th Int. Work. Struct. Heal. Monit.*, no. 734, pp. 1–8, 2007.

[22] M. Luczak, B. Peeters, and K. Dziedziech, "Static and dynamic testing of the full scale helicopter rotor blades," *Proceedings of ISMA2010, 2010.*

[23] N. Saito, T. Yari, K. Nagai, and K. Enomoto, "Damage Detection Method for CFRP Bolted Joints Joints Using Using Embedded Embedded BOCDA BOCDA Optical Optical Fiber Fiber Sensor Sensor," *Process Technol.*, vol.

558, pp. 218–226, 2013.

[24] S. S. Kessler, “Piezoelectric-Based In-Situ Damage Detection of Composite Materials for Structural Health Monitoring Systems,” Massachusetts Institute of Technology, 2002.

[25] M. Lehmann, A. Büter, B. Frankestein, F. Schubert, and B. Brunner, “Monitoring system for delamination detection-Qualification of structural health monitoring (SHM) systems,” *Conf. damage Compos. Mater. CDCM, Stuttgart*, no. September 2006, pp. 1–10, 2006.

[26] Z. Kral, W. Horn, and J. Steck, “Damage Detection in Metal Structures Using Acoustic Emission,” Proceedings of the 5th Annual GRASP Symposium, Wichita State Unibersity, pp. 2–3, 2009.

[27] P. Pollock, “Composite Structural Health Monitoring with Piezoelectric Wafer Active Sensors,” University of South Carolina, 2009.

[28] H. Guo, G. Xiao, N. Mrad, and J. Yao, “Fiber optic sensors for structural health monitoring of air platforms,” *Sensors*, vol. 11, no. 4, pp. 3687–3705, 2011.

[29] B. Glišić and D. Inaudi, *Fibre Optic Methods for Structural Health Monitoring*. John Wiley & Sons, 2007.

[30] T. Schembri, S. Tejedor, and C. Davis, “Strain Measurements Using Fibre Bragg Gratings during Full-Scale Structural Testing of an F/A-18 Centre Barrel,” *Key Eng. Mater.*, vol. 558, pp. 510–521, 2013.

[31] P. Charlaftis, T. H. Loutas, C. Koimtzoglou, and V. Kostopoulos, “Structural Health Monitoring of Aerospace Components with Optical Fibre Ribbon-Tapes,” *Aero NDT*, 2014.

[32] D. Adams, *Health Monitoring of Structural Materials and Components: Methods with Applications*. 2007.

[33] A. Rytter, “Vibration Based Inspection of Civil Engineering Structures,” Aalborg University, Denmark, 1993.

[34] T. H. Ooijevaar, *Vibration based structural health monitoring of composite skin-stiffener structures*. 2014.

[35] E. Smith *et al.*, “Recent Research on Damage Detection Methods for Helicopter Rotor Systems,” *2007 Ben Franklin Structural Health Monitoring Workshop*, 2007.

[36] N. Goldfine, V. Zilberstein, D. Schlicker, and D. Grundy, “Eddy-current in situ

Sensors for SHM," *Encycl. Struct. Heal. Monit.*, no. i, pp. 1–14, 2009.

[37] M. S. Fairbanks-Smith, "Use of Fibre-Optic (FBG) Sensors in the Structural Health Monitoring of a Battlefield Helicopter Rotor," University of Southern Queensland, 2014.

[38] R. S. Muñoz, "Structural Health Monitoring using embedded fiber optic strain sensors," University of Maine, 2008.

[39] E. Udd and W. B. Spillman, *Fiber optic sensors : an introduction for engineers and scientists*. 2011.

[40] National Instruments, "Fundamentals of Fiber Bragg Grating (FBG) Optical Sensing," 2016.

[41] A. Güemes and J. M. Menendez, "Fiber-Optic Sensors," *Structural Health Monitoring*. 2006.

[42] National Instruments, "Fiber-Optic Sensing Technologies," 2012.

[43] R. D. Sante, "Fibre Optic Sensors for Structural Health Monitoring of Aircraft Composite Structures: Recent Advances and Applications," *Sensors*, vol. 15, no. 8, pp. 18666–18713, 2015.

[44] Smart Fibres Ltd, UK, "SmartFBG, Fibre Bragg Grating Sensor", 2017.

[45] P. E. Heider, R. G. Blosser, J. Florio, R. P. Donti, and J. Garcia, "Demonstration of distributed strain sensing in production scale instrumented structures" *Proc. SPIE*, vol. 2721, 1996.

[46] Micron Optics, Inc., "What are the Specific Advantages of FBG Sensors," *http://www.micronoptics.com/what-are-the-specific-advantages-of-fbg-sensors-2/*, 2015.

[47] National Instruments, "FBG Optical Sensing: a New Alternative for Temperature Measurements," *http://www.ni.com/white-paper/51913/en/*, 2014.

[48] D. H. Kang, C. U. Kim, and C. G. Kim, "The embedment of fiber Bragg grating sensors into filament wound pressure tanks considering multiplexing," *NDT & E Int.*, vol. 39, pp. 109–116, 2006.

[49] R. Ramly, W. Kuntjoro, and M. K. A. Rahman, "Using embedded fiber bragg grating (FBG) sensors in smart aircraft structure materials," *Procedia Eng.*, vol. 41, no. Iris, pp. 600–606, 2012.

[50] G. C. Kahandawa, J. Epaarachchi, H. Wang, and K. T. Lau, "Use of FBG

sensors for SHM in aerospace structures," *Photonic Sensors*, vol. 2, no. 3, pp. 203–214, 2012.

[51] T. A. Dawood, R. A. Shenoi, and M. Sahin, "A procedure to embed fibre Bragg grating strain sensors into GFRP sandwich structures," *Compos. Part A Appl. Sci. Manuf.*, vol. 38, no. 1, pp. 217–226, 2007.

[52] Y. Hayama, F. Ohshima, and J. Ibukuro, "Measurement of torsional strain distributions on cylindrical surfaces using fiber Bragg grating optical fiber sensing," *Bulletin of the JSME, Mechanical Engineering Letters*, vol. 2, no. 16, pp. 1–8, 2016.

[53] D. Bullock, J. Dunphy, and G. Hufstetler, "Embedded Bragg grating fiber optic sensor for composite flexbeams," *SPIE 1798, Fiber Opt. Smart Struct. Ski. V, 253 (March 26, 1993)*, vol. 1798, 1992.

[54] S. Takeda, Y. Okabe, and N. Takeda, "Delamination detection in CFRP laminates with embedded small-diameter fiber Bragg grating sensors," *Compos. - Part A Appl. Sci. Manuf.*, vol. 33, no. 7, pp. 971–980, 2002.

[55] C. Shin and C. Chiang, "Fatigue damage monitoring in polymeric composites using multiple fiber bragg gratings," *Int. J. Fatigue*, vol. 28, no. 10, pp. 1315–1321, 2006.

[56] S. Yashiro, N. Takeda, T. Okabe, and H. Sekine, "A new approach to predicting multiple damage states in composite laminates with embedded FBG sensors," *Composites Science and Technology,* vol. 65, pp. 659–667, 2005.

[57] M. Ramakrishnan, G. Rajan, Y. Semenova and G. Farrell, "Overview of Fiber Optic Sensor Technologies for Strain/Temperature Sensing Applications in Composite Materials," *Sensors*, vol. 16, no.1, pp. 99, 2016.

[58] Agy, "High Strength Glass Fibers," 2017.

[59] Dassault Systèmes Simulia, "Abaqus CAE User's Manual," v. 6.12, 2012.

[60] C. Karataş, "Güçlendirilmiş Bir Kompozit Kiriş Tasarımı," *Ulusal Havacılık ve Uzay Konferansı*, 2016.

[61] Dassault Systèmes Simulia, "Abaqus Analysis User's Guide," v. 6.14, 2015.

[62] "Eight-node brick element with reduced integration (C3D8R and F3D8R)," *http://web.mit.edu/calculix_v2.7/CalculiX/ccx_2.7/doc/ccx/node27.html*, 2014.

[63] MSc Software, "Finite Element Analysis - Basic Theory Introduction," *https://simcompanion.mscsoftware.com/infocenter/index?page=home*, 2017.

[64] Y. Wang, L. Liang, Y. Yuan, G. Xu, and F. Liu, “A Two Fiber Bragg Gratings Sensing System to vibration,” *Sensors*, 2016.

[65] L. Kruger, P. L. Swart, A. A. Chtcherbakov, and A. J. van Wyk, “Non-contact torsion sensor using fibre Bragg gratings.” *Institute of Pyhsics Publishing,* vol. 15, 2004.

[66] P. L. Swart, A. A. Chtcherbakov, and A. J. van Wyk, “Bragg grating sensor for torsion and temperature measurements in rotating machinery,” *Proceedings of SPIE,* vol. 5634, pp. 353–360, 2017.

[67] X. G. Tian and X. M. Tao, “Torsion Measurement Using Fiber Bragg Grating Sensors,” *Experimental Mechanics,* vol. 41, no. 3, pp. 248-253, 2001.

[68] Smart Fibres Ltd, UK, “SmartSoft v3.1. User Manual,” 2017.

[69] Smart Fibres Ltd, UK, “SmartScan Aero Interrogator,” 2017.

[70] AFL , “Fujikura 70S Fusion Splicer Fujikura 70S Fusion Splicer,” 2017.

[71] MTS Systems Corporation, “High-Force Axial / Torsional Test Systems,” *https://www.mts.com/en/products/producttype/test-systems/load-frames-multiaxial/axial-torsional/high-force/index.htm,* 2017.

[72] MTS Systems Corporation, “647 All-Temperature Hydraulic Wedge Grips,” *https://www.mts.com/cs/groups/public/documents/library/dev_003696.pdf,* 2006.

[73] Advanced Instructional Systems Inc. and Arizona State University Department of Physics, “Basic Concepts of Error Analysis,” *http://www.webassign.net/labsgraceperiod/asucolphysmechl1/error_analysis/manual.html,* 2012.

[73] A. Mysore, “Uncertainty Analysis,” *http://www.sjsu.edu/people/ananda.mysore/courses/c1/s0/ME120-11_Uncertainty_Analysis.pdf,* 2009.

[75] B. Değerliyurt, C. Karataş, M. Şahin, and Y. Yaman, “Structural Health Monitoring System of Composite Beams with Surface Bonded and Embedded Fibre Bragg Grating Sensors,” *Key Engineering Materials,* vol. 744, pp. 332-336, 2017.

APPENDIX A

ALL THE DATA MEASUREMENTS OBTAINED FROM THE TESTS OF COMPOSITE BEAMS UNDER TORSIONAL LOAD

In Table A.1, all the torque and shear strain results obtained from three tests of each beam are presented. In addition, average values of three tests are also demonstrated.

Table A.1: The Data Obtained from the Tests of Composite Beams under Torsional Load

		Torque [N.mm]				Surface + [µε]				Surface - [µε]							
	Angle [deg]	Test 1	Test 2	Test 3	Average	Test 1	Test 2	Test 3	Average	Test 1	Test 2	Test 3	Average				
S3T	0	0.00	0.00	0.00	0.00	0.00	0.00	0.00	0.00	0.00	0.00	0.00	0.00				
	-5	-4063.38	-4090.88	-4128.69	-4094.32	2952.93	2948.58	2942.32	2947.94	-3183.21	-3194.17	-3190.10	-3189.16				
	-10	-8126.75	-8181.77	-8257.37	-8188.63	5905.86	5897.15	5884.65	5895.89	-6366.41	-6388.34	-6380.21	-6378.32				
	-15	-12190.13	-12272.65	-12386.06	-12282.95	8858.78	8845.73	8826.97	8843.83	-9549.62	-9582.51	-9570.31	-9567.48				
	-20	-16253.51	-16363.54	-16514.74	-16377.26	11811.71	11794.31	11769.30	11791.77	-12732.83	-12776.68	-12760.42	-12756.64				
		Torque [N.mm]				Surface - [µε]											
	Angle [deg]	Test 1	Test 2	Test 3	Average	Test 1	Test 2	Test 3	Average								
S1TW	0	0.00	0.00	0.00	0.00	0.00	0.00	0.00	0.00								
	-5	-4045.11	-4168.37	-4174.92	-4129.47	-2622.83	-2610.31	-2613.11	-2615.42								
	-10	-8090.22	-8336.74	-8349.85	-8258.94	-5245.67	-5220.61	-5226.22	-5230.83								
	-15	-12135.33	-12505.11	-12524.77	-12388.40	-7868.50	-7830.92	-7839.34	-7846.25								
	-20	-16180.44	-16673.48	-16699.70	-16517.87	-10491.33	-10441.22	-10452.45	-10461.67								
		Torque [N.mm]				Surface + [µε]				Woven [µε]				UD [µε]			
	Angle [deg]	Test 1	Test 2	Test 3	Average	Test 1	Test 2	Test 3	Average	Test 1	Test 2	Test 3	Average	Test 1	Test 2	Test 3	Average
S2T	0	0.00	0.00	0.00	0.00	0.00	0.00	0.00	0.00	0.00	0.00	0.00	0.00	0.00	0.00	0.00	0.00
	-5	-4084.36	-4199.78	-4214.81	-4166.31	3107.18	3109.52	3105.41	3107.37	-100.24	-20.02	-29.84	-50.03	1693.23	1744.84	1766.38	1734.82
	-10	-8168.71	-8399.56	-8429.62	-8332.63	6214.36	6219.04	6210.82	6214.74	-217.90	-88.35	-98.34	-134.86	3386.47	3489.68	3532.76	3469.64
	-15	-12253.07	-12599.33	-12644.43	-12498.94	9321.53	9328.56	9316.23	9322.11	-352.98	-204.98	-205.51	-254.49	5079.70	5234.52	5299.14	5204.45
	-20	-16337.42	-16799.11	-16859.23	-16665.26	12428.71	12438.08	12421.64	12429.48	-505.49	-369.93	-351.34	-408.92	6772.94	6979.36	7065.52	6939.27
		Torque [N.mm]				Surface - [µε]				Woven [µε]							
	Angle [deg]	Test 1	Test 2	Test 3	Average	Test 1	Test 2	Test 3	Average	Test 1	Test 2	Test 3	Average				
S1TTW	0	0.00	0.00	0.00	0.00	0.00	0.00	0.00	0.00	0.00	0.00	0.00	0.00				
	-5	-4437.71	-4551.91	-4543.97	-4511.20	-3473.31	-3462.95	-3463.26	-3466.51	-16.04	-24.37	-30.27	-23.56				
	-10	-8875.42	-9103.83	-9087.93	-9022.39	-6946.62	-6925.90	-6926.52	-6933.01	-39.45	-49.21	-62.78	-50.48				
	-15	-13313.12	-13655.74	-13631.90	-13533.59	-10419.92	-10388.84	-10389.78	-10399.52	-70.23	-74.52	-97.53	-80.76				
	-20	-17750.83	-18207.66	-18175.86	-18044.78	-13893.23	-13851.79	-13853.04	-13866.02	-108.38	-100.31	-134.53	-114.41				
		Torque [N.mm]				Surface - [µε]				UD [µε]							
	Angle [deg]	Test 1	Test 2	Test 3	Average	Test 1	Test 2	Test 3	Average	Test 1	Test 2	Test 3	Average				
S1TTUD	0	0.00	0.00	0.00	0.00	0.00	-	-	0.00	0.00	0.00	0.00	0.00				
	-5	-4546.21	-4674.34	-4678.35	-4632.97	-3463.73	-	-	-3463.73	-1964.90	-1881.89	-1869.33	-1905.37				
	-10	-9092.43	-9348.69	-9356.70	-9265.94	-6927.47	-	-	-6927.47	-3929.80	-3763.78	-3738.66	-3810.75				
	-15	-13638.64	-14023.03	-14035.05	-13898.91	-10391.20	-	-	-10391.20	-5894.71	-5645.67	-5607.99	-5716.12				
	-20	-18184.85	-18697.37	-18713.41	-18531.88	-13854.93	-	-	-13854.93	-7859.61	-7527.56	-7477.32	-7621.50				

APPENDIX B

PERCENT ERROR VALUES OBTAINED FROM THE RESULTS OF THE TESTS COMPARED TO THE AVERAGE VALUES FOR EACH COMPOSTE BEAM

Table B.1: Percent Error Values of the Results of the Tests Compared to the Calculated Average Values for Each Composite Beam

		Torque [%]			Surface + [%]			Surface - [%]		
S3T	Angle [Deg]	Test 1	Test 2	Test 3	Test 1	Test 2	Test 3	Test 1	Test 2	Test 3
	0	-	-	-	-	-	-	-	-	-
	-5	-0.76	-0.08	0.84	0.17	0.02	-0.19	-0.19	0.16	0.03
	-10	-0.76	-0.08	0.84	0.17	0.02	-0.19	-0.19	0.16	0.03
	-15	-0.76	-0.08	0.84	0.17	0.02	-0.19	-0.19	0.16	0.03
	-20	-0.76	-0.08	0.84	0.17	0.02	-0.19	-0.19	0.16	0.03
S1TW		Torque [%]			Surface - [%]					
	Angle [Deg]	Test 1	Test 2	Test 3	Test 1	Test 2	Test 3			
	0	-	-	-	-	-	-			
	-5	-2.04	0.94	1.10	0.28	-0.20	-0.09			
	-10	-2.04	0.94	1.10	0.28	-0.20	-0.09			
	-15	-2.04	0.94	1.10	0.28	-0.20	-0.09			
	-20	-2.04	0.94	1.10	0.28	-0.20	-0.09			
S2T		Torque [%]			Surface + [%]			UD [%]		
	Angle [Deg]	Test 1	Test 2	Test 3	Test 1	Test 2	Test 3	Test 1	Test 2	Test 3
	0	-	-	-	-	-	-	-	-	-
	-5	-1.97	0.80	1.16	-0.01	0.07	-0.06	-2.40	0.58	1.82
	-10	-1.97	0.80	1.16	-0.01	0.07	-0.06	-2.40	0.58	1.82
	-15	-1.97	0.80	1.16	-0.01	0.07	-0.06	-2.40	0.58	1.82
	-20	-1.97	0.80	1.16	-0.01	0.07	-0.06	-2.40	0.58	1.82
S1TTW		Torque [%]			Surface - [%]					
	Angle [Deg]	Test 1	Test 2	Test 3	Test 1	Test 2	Test 3			
	0	-	-	-	-	-	-			
	-5	-1.63	0.90	0.73	0.20	-0.10	-0.09			
	-10	-1.63	0.90	0.73	0.20	-0.10	-0.09			
	-15	-1.63	0.90	0.73	0.20	-0.10	-0.09			
	-20	-1.63	0.90	0.73	0.20	-0.10	-0.09			
S1TTUD		Torque [%]			UD [%]					
	Angle [Deg]	Test 1	Test 2	Test 3	Test 1	Test 2	Test 3			
	0	-	-	-	-	-	-			
	-5	-1.87	0.89	0.98	3.12	-1.23	-1.89			
	-10	-1.87	0.89	0.98	3.12	-1.23	-1.89			
	-15	-1.87	0.89	0.98	3.12	-1.23	-1.89			
	-20	-1.87	0.89	0.98	3.12	-1.23	-1.89			

APPENDIX C

MEAN AND STANDARD DEVIATION CALCULATIONS

The mean values of all the measurements are calculated at each angle of twist for each beam using the Equation C.1.

$$\bar{x} = \frac{\sum_{i=1}^{n} x_i}{n} \tag{C.1}$$

where

x: Measured quantity

$\bar{x}$: Mean of the measurements

n: Number of measurements

Then, standard deviations are calculated using the Equation B.2.

$$\sigma = \sqrt{\frac{\sum_{i=1}^{n}(x_i - \bar{x})^2}{n-1}} \tag{C.2}$$

where

σ: Standard deviation

N: Number of measurements

Finally, the difference of the measurements from the mean, k, is calculated in terms of standard deviation, σ, as in Equation B.3.

$$k = \frac{x - \bar{x}}{\sigma} \tag{C.3}$$

All the difference of the measurements from the mean are presented in Table C.1. under test number columns.

Table C.1: Mean and Standard Deviation Values Calculated for the Tests of Each Beam

		Torque [N.mm]					Surface + [με]					Surface - [με]				
S3T	Angle [Deg]	Mean	Standard Deviation	Test 1	Test 2	Test 3	Mean	Standard Deviation	Test 1	Test 2	Test 3	Mean	Standard Deviation	Test 1	Test 2	Test 3
	0	-	-	-	-	-	-	-	-	-	-	-	-	-	-	-
	-5	-4094.32	32.79	0.94	0.10	-1.05	2947.94	5.33	0.94	0.12	-1.05	-3189.16	5.54	1.07	-0.90	-0.17
	-10	-8188.63	65.58	0.94	0.10	-1.05	5895.89	10.66	0.94	0.12	-1.05	-6378.32	11.09	1.07	-0.90	-0.17
	-15	-12282.95	98.37	0.94	0.10	-1.05	8843.83	15.99	0.94	0.12	-1.05	-9567.48	16.63	1.07	-0.90	-0.17
	-20	-16377.26	131.16	0.94	0.10	-1.05	11791.77	21.32	0.94	0.12	-1.05	-12756.64	22.17	1.07	-0.90	-0.17
		Torque [N.mm]					Surface - [με]									
S1TW	Angle [Deg]	Mean	Standard Deviation	Test 1	Test 2	Test 3	Mean	Standard Deviation	Test 1	Test 2	Test 3					
	0	-	-	-	-	-	-	-	-	-	-					
	-5	-4129.47	73.13	1.15	-0.53	-0.62	-2615.42	6.57	-1.13	0.78	0.35					
	-10	-8258.94	146.26	1.15	-0.53	-0.62	-5230.83	13.15	-1.13	0.78	0.35					
	-15	-12388.40	219.39	1.15	-0.53	-0.62	-7846.25	19.72	-1.13	0.78	0.35					
	-20	-16517.87	292.52	1.15	-0.53	-0.62	-10461.67	26.30	-1.13	0.78	0.35					
		Torque [N.mm]					Surface + [με]					UD [με]				
S2T	Angle [Deg]	Mean	Standard Deviation	Test 1	Test 2	Test 3	Mean	Standard Deviation	Test 1	Test 2	Test 3	Mean	Standard Deviation	Test 1	Test 2	Test 3
	0	-	-	-	-	-	-	-	-	-	-	-	-	-	-	-
	-5	-4166.31	71.37	1.15	-0.47	-0.68	3107.37	2.06	-0.09	1.04	-0.95	1734.82	37.59	-1.11	0.27	0.84
	-10	-8332.63	142.75	1.15	-0.47	-0.68	6214.74	4.12	-0.09	1.04	-0.95	3469.64	75.18	-1.11	0.27	0.84
	-15	-12498.94	214.12	1.15	-0.47	-0.68	9322.11	6.19	-0.09	1.04	-0.95	5204.45	112.76	-1.11	0.27	0.84
	-20	-16665.26	285.50	1.15	-0.47	-0.68	12429.48	8.25	-0.09	1.04	-0.95	6939.27	150.35	-1.11	0.27	0.84
		Torque [N.mm]					Surface - [με]									
S1TTW	Angle [Deg]	Mean	Standard Deviation	Test 1	Test 2	Test 3	Mean	Standard Deviation	Test 1	Test 2	Test 3					
	0	-	-	-	-	-	-	-	-	-	-					
	-5	-4511.20	63.77	1.15	-0.64	-0.51	-3466.51	5.89	-1.15	0.60	0.55					
	-10	-9022.39	127.53	1.15	-0.64	-0.51	-6933.01	11.79	-1.15	0.60	0.55					
	-15	-13533.59	191.30	1.15	-0.64	-0.51	-10399.52	17.68	-1.15	0.60	0.55					
	-20	-18044.78	255.07	1.15	-0.64	-0.51	-13866.02	23.57	-1.15	0.60	0.55					
		Torque [N.mm]					UD [με]									
S1TTUD	Angle [Deg]	Mean	Standard Deviation	Test 1	Test 2	Test 3	Mean	Standard Deviation	Test 1	Test 2	Test 3					
	0	-	-	-	-	-	-	-	-	-	-					
	-5	-4632.97	75.16	1.15	-0.55	-0.60	-1905.37	51.93	-1.15	0.45	0.69					
	-10	-9265.94	150.32	1.15	-0.55	-0.60	-3810.75	103.87	-1.15	0.45	0.69					
	-15	-13898.91	225.48	1.15	-0.55	-0.60	-5716.12	155.80	-1.15	0.45	0.69					
	-20	-18531.88	300.64	1.15	-0.55	-0.60	-7621.50	207.74	-1.15	0.45	0.69					